IMPROVING THE ROBUSTNESS AND UTILITY

OF HYPERPOLARIZED-GAS MAGNETIC

RESONANCE IMAGING

_____

A Dissertation

Presented to

The Faculty of the School of Engineering and Applied Science

University of Virginia

_____

In Partial Fulfillment

Of the requirements for the Degree

Doctor of Philosophy in Biomedical Engineering

by
Kun Qing
December, 2012

APPROVAL SHEET

The dissertation is submitted in partial fulfillment of the

requirements for the degree of

Doctor of Philosophy in Biomedical Engineering

_____
Author

This dissertation has been read and approved by the examining Committee:

_____
Dissertation advisor

_____

_____

_____

Accepted for the School of Engineering and Applied Science:

_____
**Dean, School of Engineering and
Applied Science**

May , 2013

Abstract

Hyperpolarized-gas MRI using ^{3}He or ^{129}Xe is an evolving technology for providing images of the lung with high spatial and temporal resolution. The associated acquisition strategies, such as ventilation imaging and ^{129}Xe dissolved-phase imaging, have great potential to yield a comprehensive morphologic and functional assessment of the lung. The goal of this dissertation was to advance hyperpolarized-gas MRI by addressing three specific needs: (1) robust and rapid calibration of the MR-scanner transmitter; (2) accelerated acquisition of hyperpolarized-gas and proton image sets during a single breath hold; and (3) quantitative regional assessment of ^{129}Xe dissolved in lung tissue and blood.

Subject-specific calibration of the MR-scanner transmitter is an important initial step for every MR examination. However, due to the non-equilibrium nature of hyperpolarized-gas magnetization, techniques established for proton MRI are not applicable for hyperpolarized gases. In this work, we sought to design and implement an optimized phase-based transmitter calibration method that yields accurate results from only a small fraction of the hyperpolarized-gas magnetization, and to validate this method against a commonly-used amplitude-based method in human subjects. To permit integration at the beginning of any imaging pulse sequence, the proposed method requires less than 100-ms, and consumes no more than 5% of the hyperpolarized magnetization. The method yielded results comparable to the reference amplitude-based approach in the presence of B_0 and B_1 inhomogeneity representative of that encountered in human lung imaging.

Acquisition of ^{3}He and proton (^{1}H) image sets during the same breath hold offers complementary functional and anatomical information, and greatly facilitates quantitative analysis of ventilation defects in the ^{3}He images. Although isotropic 3D image sets are preferred, such a combined ^{3}He /^{1}H acquisition requires a breath-hold duration of 10-20 s (depending on lung dimensions), which may be difficult for subjects with impaired respiratory function. In this work, to accelerate the combined acquisition of ^{3}He and ^{1}H 3D image sets, we incorporated the ideas of compressed sensing to achieve a breath-hold duration which is less than one-half of that required for the conventional approach, without application of multi-coil parallel imaging. The undersampling pattern and reconstruction quality for both ^{3}He and ^{1}H imaging were evaluated using simulations based on fully-sampled data sets and using direct comparison of fully-sampled and undersampled data from the same subject. Finally, the performance of the accelerated and conventional acquisitions in depicting ventilation defects was compared in subjects with pulmonary disease.

Through recent advances in pulse-sequence techniques and ^{129}Xe-polarization technology, acquisition of ventilation and dissolved-phase ^{129}Xe images of the human lung in a single breath hold has been demonstrated. To maximize the information on pulmonary disease offered by dissolved-phase ^{129}Xe, it is important to extend this methodology to permit quantification of the individual dissolved-phase components in the human lung. This project is focused on developing an MRI pulse sequence that permits regional quantification of the tissue (lung parenchyma/plasma) and red blood cell (RBC) fractions of the dissolved ^{129}Xe signal, relative to the associated gas ^{129}Xe signal, from a breath-hold acquisition of less than 20 s. This technique was tested in healthy

subjects and validated against spectroscopic measurements of the dissolved-phase ^{129}Xe components in the lung. Finally, a pilot study was performed to compare tissue/RBC fractions in healthy subjects to those in subjects with pulmonary disease.

Acknowledgements

I would like to personally thank those who helped me a lot during my studies at the University of Virginia. First of all, I would like to thank my advisor, Dr. John P. Mugler, III. I learned a lot from him, not only in research, but also in the basic attitude towards life and work. He was always patient with every question I asked, leading me to the right way of scientific thinking, responsive to almost everything even though some aspects were very trivial, and being very careful with detailed aspects. I benefited a lot from his excellent expertise in MRI, great passion for work, easygoing personality and inspiring optimism. I also would like to thank Dr. Craig H. Meyer for educating me on MRI and offering lots of constructive advice towards my dissertation research. I would like to thank Dr. G. Wilson Miller for his many suggestions during discussions, lots of technical support he offered me, teaching me in Advanced MRI classes, and also spending lots of time helping me modifying the dissertation. I want to acknowledge Dr. James R. Brookeman for his sincere help to improve my dissertation, and also his long-time encouragement throughout my graduate studies. I want to thank Dr. John A. Hossack for giving me suggestions on my proposal and dissertation.

I greatly thank Talissa A. Altes, MD for her contributions in all my research projects and guiding my thinking from clinical perspectives during discussions. I would like to thank Dr. Frederick H. Epstein for his teaching and organization of Advanced MRI classes, which greatly broadened and deepened my understanding of MR techniques. I want to thank Dr. Kai Ruppert, who taught me a lot in both MR technical aspects and

lung physiology when I worked on the dissolved-phase ^{129}Xe project. I also acknowledge Dr. Jaime Mata, for his sincere help and very hard working in gas polarization. I appreciate Peter Komlosi, MD for helping me using his solid medical physiology background. Also, I would like to thank the staff of the hyperpolarized gas research team, John Christopher, Joanne Gersbach, Vanessa John, and Doris Harding, for their great support.

Finally, I would like to thank Xue Feng, Xiao Chen, Yang Yang, Bhairav Mehta, Meihan Wang, Li Zhao and Samuel W. Fielden for technical and programming discussions.

I also greatly appreciate my parents for their long time caring and support.

Table of Contents

List of Symbols

B_0 Main static magnetic field strength

B_1 Radio-frequency field strength

$B_{1,normalized}(t)$ Radio-frequency pulse normalized by peak B_1 value in Bloch-Siegert shift

$B_{1,peak}$ Peak B_1 value of RF pulse in Bloch-Siegert shift

F, Fs Fourier Transform

f_r RBC fraction

FA_{act} Flip angle measured by calibration

FA_{nor} Nominal (assumed) flip angle applied by calibration

f Time frequency, in Hz

G_{FE} Magnetic gradient field in the frequency-encoding direction

G_{PE} Magnetic gradient field in the phase-encoding direction

G_s Spoiler gradient

G_{SS} Magnetic gradient field in the slice-select direction

G_x Magnetic gradient field in the x direction

G_z Magnetic gradient field in the z direction

I The identity matrix

i Imaginary number, equal to $\sqrt{-1}$

k Sparsity dimension

k_x x component of k-space spatial frequency

k_y y component of k-space spatial frequency

k_z	z component of k-space spatial frequency
K_{BS}	Bloch-Siegert shift constant
m	Data in image domain
M	Magnetization magnitude or amount
M_{xy}	Transverse magnetization, usually expressed in complex form
M_z	Longitudinal magnetization, a scalar value
N	Image matrix dimension
p	Theoretical signal intensity at echo time zero
R	Acceleration factor
$R2^*_r$	R2* value of RBC component
$R2^*_t$	R2* value of tissue component
SNR_{mag}	Measured signal-to-noise ratio of signal magnitude
t	Time
T	Pulse duration in MATPULSE
T_1	Spin-lattice relaxation time constant
T_2	Spin-spin relaxation time constant
T_2^*	Time constant composed of spin-spin relaxation and local magnetic-field non-uniformities.
u	Vector in n-dimensional space R^n
V_{app}	Applied (reference) transmitter calibration voltage
V_{cal}	Calculated transmitter calibration voltage
w	Vector in n-dimensional space R^n
w_r	Chemical shift of RBC component in radians/s

w_t	Chemical shift of tissue component in radians/s
W	Frequency span in MATPULSE
y	Data in k-space domain
X_i	Random variable
x	Spatial coordinate measured along the x axis
y	Spatial coordinate measured along the y axis
z	Spatial coordinate measured along the z axis
α	Flip angle of a radiofrequency pulse, typically small compared to 90°, or phase difference between RBC and tissue components
Ψ	Sparsifying transform
φ_{BS}	Phase shift induced by Bloch-Siegert pulse in radians
θ	Phase angle
σ_{phase}	Measured standard deviation of phase
π	Ratio of any circle's circumference to its diameter, a constant value of 3.1415926535…
γ	Gyromagnetic ratio
$\omega_{RF}(t)$	Off-resonance angular frequency in Bloch-Siegert shift

List of Abbreviations

1D	One-dimensional
2D	Two-dimensional
3D	Three-dimensional
ADC	Apparent Diffusion Coefficient
ANTs	Advanced Normalization Tools
bSSFP	Balanced Steady-state Free Precession
BS	Bloch-Siegert Shift
CDF 9/7	Cohen-Daubechies-Feauveau 9/7 Wavelet
COPD	Chronic Obstructive Pulmonary Disease
CNS	Central Nervous System
CSSR	Chemical Shift Saturation Recovery
CT	computed tomography
DLCO	Diffusion Capacity of the Lung for Carbon monoxide
EPI	Echo Planar Imaging
FA	Flip Angle
FEV_1	Forced Expiratory Volume in 1 second
FID	Free Induction Decay
FT	Fourier Transform
FVC	Forced Vital Capacity
FWHM	Full Width at Half Maximum
GRE	Gradient Echo

HPG	Hyperpolarized Gas
ICE	Image Calculation Environment
IDEA	Integrated Development Environment for Applications
IDEAL	Iterative Decomposition of Water and Fat with Echo Asymmetry and Least Squares
IFT	Inverse Fourier Transform
IND	Investigational New Drug application
MAPE	Mean Absolute Percentage Error
MRI	Magnetic Resonance Imaging
NMR	Nuclear Magnetic Resonance
PB	Pass Band
PCG	Preconditioned Conjugate Gradient
PF	Partial Fourier
PO2	Oxygen Partial Pressure
PPM	Parts Per Million
PSF	Point Spread Function
PET	Positron Emission Tomography
QPWLS	Quadratic Penalized Weighted Least Squares Iterative Reconstruction
RB	Rejection Band
RF	Radiofrequency
ROI	Region of Interest
RV	Residual Volume

RBC   Red Blood Cell

SE   Spin Echo

SLR   Shinnar-Le Roux Algorithm

SNR   Signal-to-Noise Ratio

SPGRE   Spoiled Gradient Echo

SPECT   Single Photon Emission Computed Tomography

SSFP   Steady-State Free Precession, same meaning as TrueFISP

SSIM   Structural Similarity Index

TE   Echo Time

TLC   Total Lung Capacity

TPSF   Transform Point Spread Function

TR   Repetition Time

UI   User Interface

VOI   Voxel of Interest

Chapter 1

Introduction

1.1 Dissertation Scope

Obstructive lung diseases, such as chronic obstructive pulmonary disease (COPD) and asthma, affect millions of people's lives and are both reported to increase in incidence in recent years [1, 2, 3, 4]. There is growing need to evaluate newly developed therapies and to better understand the underlying mechanisms leading to development of these pulmonary diseases. Imaging techniques which can provide regional information on the structure and function of the lung are highly desirable to help address this need.

Hyperpolarized-gas (HPG) MRI has shown rapid development in the past two decades, and has proven to have great potential for yielding a comprehensive morphologic and functional assessment of the lung by providing images with high spatial and temporal resolution [5, 6, 7, 8]. Nonetheless, imaging time, limited by breath-hold duration and the non-equilibrium nature of hyperpolarized-gas magnetization, remains an obstacle for producing images with higher quality and for developing new technologies to explore many aspects of lung function. The work for this dissertation focused on developing new pulse sequences and incorporating new MRI technology into hyperpolarized-gas studies to improve robustness and utility in three ways: 1) development of a new transmitter calibration pulse sequence for hyperpolarized-gas studies, which consumes less magnetization and requires less time than existing methods, and thus can be integrated into any imaging pulse sequence; 2) acceleration and optimization of an imaging pulse

sequence useful for quantification of ventilation abnormalities, which currently requires a relatively long breath-hold duration; and 3) design of a new acquisition method to better explore basic lung function by providing regional maps of gas exchange using hyperpolarized ^{129}Xe.

1.2 Dissertation Overview

This dissertation is organized as follows.

Chapter 1 provides a brief introduction to the scope and structure of this dissertation.

Chapter 2 discusses background information and the corresponding three specific aims.

Chapter 3 presents a phase-based method for HPG transmitter calibration, and work on optimization and evaluation of this method using simulation, phantom tests and human studies.

Chapter 4 describes acceleration of a combined ^{3}He and ^{1}H acquisition method using the compressed-sensing technique, and presents assessment of the reconstruction fidelity for this method in healthy and diseased subjects.

Chapter 5 demonstrates the implementation of a multi-echo 3D radial pulse sequence to acquire ^{129}Xe dissolved-phase and gas-phase images and the separation of the ^{129}Xe components dissolved in tissue and red blood cells (RBCs) using these multi-echo images, and describes relevant methodologies to analyze the results. This chapter also presents 3D ^{129}Xe dissolved-phase and gas-phase studies in human subjects, and quantitatively compares the results from healthy with the ones from diseased subjects.

Chapter 6 summarizes the work of this dissertation project and discusses the possibilities for further development.

Chapter 2

Background

2.1 Lung Function and Major Diseases

The major function of the lung is gas exchange: providing oxygen needed for metabolism and eliminating carbon dioxide. This process is driven by free diffusion. According to Fick's law of diffusion, the amount of gas that moves across the blood-gas barrier is proportional to the area of the exchange surface but inversely proportional to the thickness of the barrier wall. So, a larger surface area and a thinner blood-gas barrier facilitate the exchange process. This is achieved by the formation of the branching structures for both pulmonary airways and pulmonary blood vessels, and wrapping of the small blood vessels (capillaries) around an enormous number of small air sacs called alveoli, as Figure 2.1 shows.

The airway consists of a series of branching tubes which become shorter, narrower and more numerous, moving from the entrance (trachea) to deeper within the lung [9-12]. The whole branching system, like an inverted tree (Figure 2.2), can be divided into 23 generations according to Weibel [10]. The first 16 generations: trachea, right and left main bronchi, lobar, segmental bronchi, continuing to terminal bronchioles, make up the conducting airways with a volume of about 150 ml [9]. They lead the air to gas exchange regions, and are often called "anatomical dead space." The terminal bronchioles divide into respiratory bronchioles, alveolar ducts and finally alveoli. This alveolated region of the lung where the gas exchange occurs is known as the respiratory zone, which makes up

most of the lung volume of about 2.5 to 3 liters [9]. If this space were occupied by a single sphere, the internal surface area would be only 1/100 of a square meter. But in reality, human lung has an exchange surface area of about 70 square meters, which is accumulated from myriads of alveoli (about 300 million) at the end of the branching system.
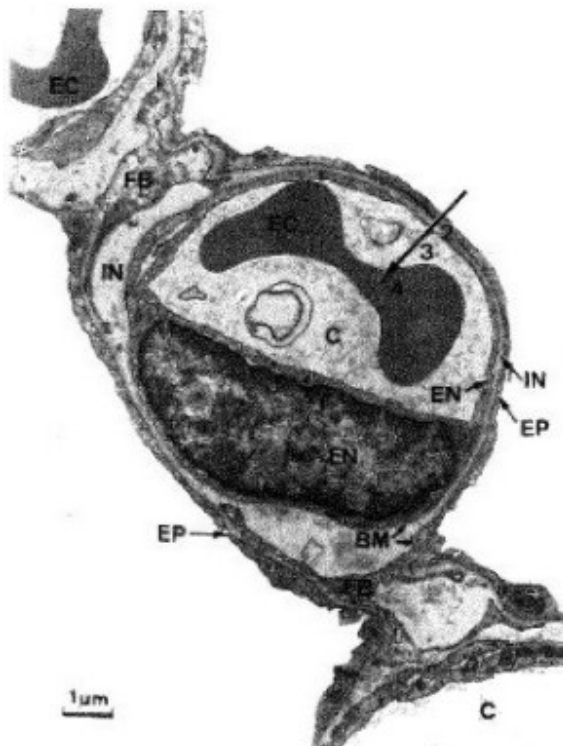
Figure 2.1. Electron micrograph showing a pulmonary capillary (C) in the alveolar wall. Large arrow indicates the diffusion path from alveolar gas to the interior of the erythrocyte (red blood cell, EC), alveolar epithelium (EP), interstitum (IN), capillary endothelium (EN), and plasma. The extremely thin blood-gas barrier can be noticed in this graph. (From West JB. Respiratory Physiology- The Essentials. Baltimore, USA: Williams & Wilkins; 1998 [9].

The pulmonary blood vessels also form a branching structure from the pulmonary artery to the capillaries and back to the pulmonary veins. Initially, the arteries, veins and bronchi travel close together, but when approaching the periphery of the lungs, the veins separate to pass between the lobules, whereas the arteries and bronchi continue to run together through the centers of lobules. The capillaries form a dense network in the walls of alveoli. The diameter of capillaries is about 10 μm, only large enough to allow one red blood cell to pass. The blood-gas barrier is also extremely thin, for example, in Figure 2.1

the blood-gas barrier is about 0.3 um in some places   All of these factors create a very efficient environment for gas exchange.

During inspiration, due to contraction of the diaphragm or rising of the ribs, the volume of the thoracic cavity increases and air is drawn into the lung. Inspired air flows down to about the terminal bronchioles by bulk flow. After this point, diffusion of gas within the airways becomes dominant. Expiration during resting breathing is mainly driven by passive return of the lung due to the elasticity of the lung tissue.

	generation		diameter (cm)	length (cm)	number	total cross sectional area (cm^2)
conducting zone	trachea	0	1.80	12.0	1	2.54
	bronchi	1	1.22	4.8	2	2.33
		2	0.83	1.9	4	2.13
		3	0.56	0.8	8	2.00
	bronchioles	4	0.45	1.3	16	2.48
		5 ↓	0.35 ↓	1.07 ↓	32 ↓	3.11 ↓
	terminal bronchioles	16	0.06	0.17	$6 \cdot 10^4$	180.0
transitional and respiratory zones	respiratory bronchioles	17	↓	↓	↓	↓
		18 ↓				
		19	0.05	0.10	$5 \cdot 10^5$	10^3
	alveolar ducts	20	↓	↓	↓	↓
		21				
		22 ↓				
	alveolar sacs	23	0.04	0.05	$8 \cdot 10^6$	10^4

Figure 2.2.   Schematic representation of airways branching in the human lung. (From Weibel ER. Morphometry of the Human Lung. Heidelberg: Springer Verlag; 1963 [10].)

Asthma [1] and COPD [2] are major lung diseases which affect millions of people worldwide. Improved methods of detection, intervention and treatment can reduce this burden and greatly promote health [3, 4, 13].

COPD is a preventable and treatable disease characterized by airflow limitation that is not fully reversible, as defined by the American Thoracic Society [14]. COPD is the fourth leading cause of death in the United States, and is the only major cause of death for which the age-adjusted death rate has increased in recent years. Currently, there is not sufficient knowledge on the genetic factors leading to COPD. Nonetheless, cigarette smoking is found to be the most important risk factor for COPD [14]. According to a statistical report [15] from 2006, nearly 8 out of 10 cases of COPD are caused by exposure to cigarette smoking. Emphysema, defined as abnormal enlargement of airspaces distal to the terminal bronchioles of the lung, occurs in a large portion of COPD subjects [2]. Because of the rapidly increasing rates of illness and death in COPD [16], and since only "rudimentary standards are available for describing the severity of COPD" [17], there is a growing need for improved tools for applications like monitoring the lung functional response to new treatments or aiding in the rapid development of novel respiratory drugs targeting COPD.

Asthma is a lung disease characterized by reversible obstruction of the small airways and chronic inflammation, resulting in reduced pulmonary ventilation [18, 19]. The prevalence of asthma has increased since the 1980s, but the death rate from asthma has been well controlled, even though there is no cure for asthma [18, 19, 20]. Also, asthma is the most common chronic disease of childhood, affecting about 4.8 million children in the US. During an asthma attack, airway smooth muscles tighten and constrict the airways, narrowing the airways and allowing less airflow to pass. In addition, cells in the airways

produce more mucus due to inflammation, which further narrows the effective airway diameter. Even in mild asthma, obstruction of small airways can lead to air trapping and regional hyperinflation; while in severe asthma, this can cause loss of elasticity of the lungs and low oxygen saturation [21, 22-26]. Prior reports in asthmatic patients were typically limited to only gross anatomic abnormalities such as bronchiectasis, atelectasis, or bronchial wall thickening [27-29]. Methods which help assessment of airway anatomy, regional lung mechanics and associated lung function (gas exchange) can promote understanding of the differences between the lungs of healthy subjects versus those with asthma, or of the differences between severe and non-severe asthma [30].

2.2 Methods of Assessing Major Lung Diseases

Clinical assessment of COPD is based on medical history, physical examination and pulmonary function tests (PFTs). Chest radiography can help to differentiate the diagnosis, and chest computed tomography (CT) is highly recommended if there is doubt of the diagnosis and in preparation for bullectomy or lung volume-reduction surgery [2]. But, these methods are not very sensitive to the early changes of the lung during initial stages of COPD, and are not sensitive enough to monitor gradual disease progression.

The diagnosis of asthma depends on two points: 1) evidence of episodic symptoms of airflow obstruction; and 2) obstructions are at least partially reversible [18, 20]. Similar to COPD, medical history, physical examination, PFTs, chest radiography and X-ray CT are common means to diagnose or evaluate asthma. Among them, medical history, physical examination and PFTs are global measurements, not sensitive to early detection and providing little information as to the regional distribution of disease.   X-ray CT has emerged as the choice for comprehensive assessment of the lung by providing a detailed

assessment of the airway and vascular trees, parenchyma, pulmonary blood volume [31], and regional ventilation [32]. However, X-ray CT is limited in assessing the lung function. For example, although it allows assessment of pulmonary function by obtaining images with inhalation of stable, non-radioactive xenon gas and determining the wash-in and wash-out rates, the image resolution and repeatability of these techniques under current technical conditions are limited. Concern about ionizing radiation further hinders its feasibility, as well as that of techniques such as Single Photon Emission Computed Tomography (SPECT), particularly when repeated imaging is needed longitudinally or the target subjects are children.

In summary, there is great need for better diagnostic imaging methods for lung diseases including COPD and asthma.

2.3 Hyperpolarized Gas Magnetic Resonance Imaging

Despite the recent advances with techniques such as ultrashort echo time imaging of the lung parenchyma [33], proton MRI still has shortcomings in evaluating pulmonary structure and function. For example, proton MRI cannot directly image the airspaces, and is limited in exploring the physiological function of the lungs.

Hyperpolarized noble gas MRI, using ^{3}He or ^{129}Xe, has demonstrated the capability to detect changes in ventilation [34, 35, 36, 37], lung microstructure [38, 39, 41, 41], and quantities related to perfusion and gas exchange in the lung [42, 43, 44, 45], all of which are related to normal lung development and function, as well as disease progression.

The most commonly used technique for hyperpolarized gas (HPG) MRI of the lung is ventilation imaging, which depicts the signal intensities (spin-density weighted) of the functioning (ventilated) regions of the lung, and detects ventilation defects: regions of

absent or relatively low signal intensity within the lung. Studies have shown HPG MRI is able to detect ventilation changes in the lung with much higher sensitivity than either spirometry or scintigraphy [34, 35]. For instance, ventilation imaging using HPG MRI showed the capability to detect regional airway closure in moderate to severe asthma [35], and changes before/after breathing albuterol [47], and also showed sensitivity and regional specificity for detecting obstructive lung diseases like COPD [37].

The application of diffusion-weighted MRI techniques to HPG MRI allows characterization of the lung microstructure by measuring the random Brownian motion of the gas atoms within the lung airspaces. By measuring the signal attenuation for at least two b values, an apparent diffusion coefficient (ADC) can be calculated, representing the restriction of gas inside the lung. Diffusion-weighted MRI of HPG has proven to be exquisitely sensitive to both diseased-induced alternations and normal physiological variations [48, 49], and even more sensitive than high-resolution CT [46].

The paramagnetic effects of oxygen have been exploited to measure the partial pressure of oxygen (pO_2) inside the lung using HPG MRI [42, 43]. This method shows potential for providing valuable information on both healthy and diseased subjects [44].

Further, various other techniques for probing the structure and function of the lung using HPG have been developed, such as dynamic imaging of gas flow [50]. In particular, hyperpolarized [129]Xe, because of its relatively high solubility in lung parenchyma and blood, has great potential for exploring characteristics of lung function, such as gas exchange and uptake [51]; details of [129]Xe dissolved-phase imaging are discussed in Section 2.6.

2.4 Phase-based Calibration Method for HPG MRI

Calibrating the transmitter voltage (flip angle) for each subject is a standard procedure that is performed for every clinical MRI exam. The relationship between the radiofrequency (RF) power output to the transmit coil and the B_1 field produced depends on the size, orientation, geometry, and composition of the subject. This calibration is critical for obtaining consistent and optimum image quality, and is thus integrated into the software of commercial MR scanners. However, established transmitter calibration procedures for ^1H acquisitions, either amplitude-based [52] or phase-based [53] methods, typically use high-flip-angle (90° or greater) RF pulses and are often iterative.

Because of the non-equilibrium nature of hyperpolarized-gas magnetization, calibration methods used in proton acquisitions are not suitable for hyperpolarized gases. In most of the current hyperpolarized-gas studies at our institution, a calibration procedure is done at the beginning of every study. Subjects inhale a small dose of hyperpolarized gas (50-200 ml; a smaller volume [50-100 ml] for ^3He and larger volume [>100 ml] for ^{129}Xe), and then the calibration pulse sequence is executed. The transmitter calibration is then extracted from signals created by excitation with a series of RF pulses, with spoiling of transverse magnetization and a short repetition time (TR) between pulses. Neglecting T_1, this yields directly the signal depletion caused by B_1 from which the correct calibration voltage can be determined [54, 55]. Results of the calibration are written to a log file. The calculated frequency and calibration voltage (or scaling factor to the flip angle for particular sequences) are set manually for the rest of the studies using the same RF coil. This whole process is manual and requires a separate dose of hyperpolarized gas. We will call this the amplitude-based method in the scope of this
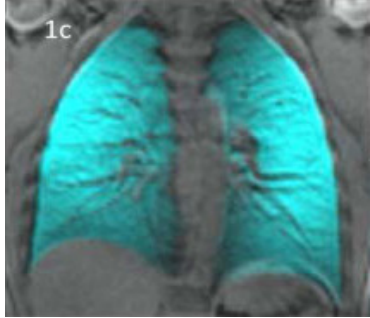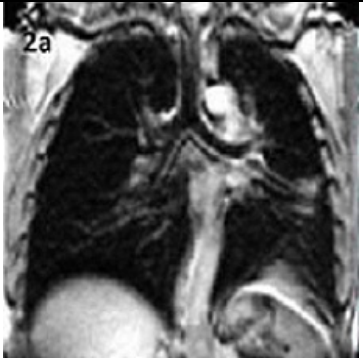
dissertation. This amplitude-based method depletes all (or most, see Figure 2.3) of the available magnetization and also requires iterative excitation, yielding a relatively long acquisition time.   Thus this method is not suitable to be appended at the beginning of an imaging or spectroscopy pulse sequence. Also, the accuracy of this method is dependent on T_1 relaxation (or oxygen induced T_1 variation) [56] and also B_1 field inhomogeneity [60]. We need a calibration design which is fast, accurate enough, and consumes very little magnetization, thus can be integrated into the beginning of an arbitrary sequence.
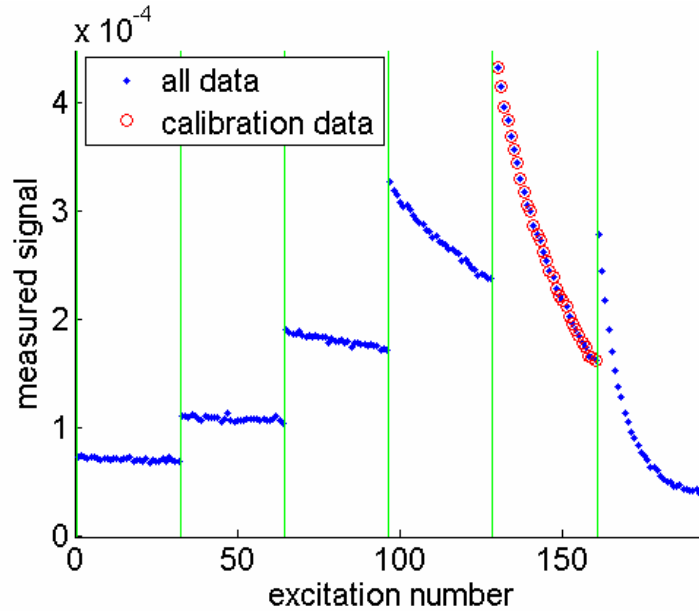
Figure 2.3.   Amplitude of measured signals versus excitation number from the amplitude-based method [54]. The pulse sequence includes up to 8 "blocks," each of which contains a series of 32 excitation RF pulses with the same flip angle.   The flip angle for a given block is double that for the previous block. The block with the highest signal magnitude (red circles) is used to calculate the transmitter voltage by fitting a mono-exponential decay to the signals.

2.5 Combined ^{3}He and ^{1}H Acquisition

Hyperpolarized-gas magnetic resonance imaging shows potential to offer high resolution images of ventilated lung airspaces [5, 6, 35, 36], while conventional proton (^{1}H) MR imaging of the chest [65, 66] can provide reasonable depiction of lung parenchyma and high resolution imaging of the surrounding structures such as the chest wall, heart and major vessels. Acquisition of both hyperpolarized-gas and ^{1}H image sets is considered important for interpreting the anatomic and physiological changes of the lung [67], and has proven to be valuable in disease assessment [67, 68].

Figure 2.4. Combined ^{3}He and ^{1}H acquisitions	^{1}H Images	^{3}He Image Overlaid on ^{1}H image
a. Lung images acquired from a healthy volunteer, showing excellent registration between ^{3}He and ^{1}H images. Adapted from [72] with permission.		
b. Images from a patient with lung cancer and COPD showing tumor in the left lung. The upper part of the lung is poorly ventilated in the ^{3}He images. Adapted from [72] with permission		

Previously, such a combined acquisition required multiple breath-holds due to relatively long acquisition times for both the ^{3}He and ^{1}H acquisitions. Retrospective

image registration cannot completely eliminate residual errors [69], particularly since temporal synchronicity between image sets is lost [70]. With hardware development for rapid switching between resonance frequencies, frequency multiplexing and dual-tuned RF coils, and improvement of imaging-sequence techniques [71], acquisition of both [3]He and ^{1}H image sets in one breath-hold period becomes feasible and spatially-registered images obtained during the time course of the same breath hold are found to be helpful for identifying and quantifying ventilation defects [72]. Figure 2.4 shows acquisition results from a healthy subject (upper images), in which the [3]He and ^{1}H images show excellent spatial registration, and from a patient diagnosed with lung cancer and COPD (lower images); images are reproduced from [72] with permission. However, the total acquisition time using current techniques is still longer than 15 seconds in most cases, even when partial Fourier and elliptical scanning techniques are applied. This breath-hold duration may be difficult to endure, especially for diseased subjects. Therefore we seek acceleration of the existing imaging strategy, while maintaining sufficient image quality for diagnosis.

2.6 Gas Uptake Imaging using Hyperpolarized [129]Xe

2.6.1 Xenon Dissolved-phase and Lung Function

The primary function of the lung is exchange of respiratory gases. Impaired gas exchange in pulmonary disease can cause symptomatic shortness of breath, and in severe disease can progress to respiratory failure and death. Although our knowledge of gas-exchange status in individual patients is derived primarily from whole-lung measurements, gas exchange can vary substantially within the lung, especially for heterogeneous conditions like COPD and asthma. Thus, regional assessment of

ventilation and gas uptake would permit investigation of the fundamental process of gas exchange, and improve our understanding of how heterogeneous diseases such as COPD and asthma affect gas exchange.   In addition, the ability to easily and non-invasively quantify regional gas uptake may prove invaluable for evaluating new therapeutics for lung diseases.   Nonetheless, despite many recent advances in medical imaging technology, there is no clinical-imaging method that permits quantitative regional assessment of both gas delivery to the alveolar airspaces and gas uptake into the lung parenchyma and blood.

Hyperpolarized [129]Xe, because of its relatively high solubility in biological tissues and exquisite sensitivity to its environment, which results in large range of chemical shifts upon solution [76], is particularly useful in exploring characteristics of lung function, such as gas uptake and exchange. Following inhalation, multiple MR spectral peaks, associated with different compartments, can be detected inside the lung, with most of the [129]Xe staying in the lung airspaces ("gas-phase"), and a small fraction (about 1-2%) of [129]Xe dissolving into the lung parenchyma and blood ("dissolved-phase"), giving rise to relatively small peaks with chemical shifts of around 200 ppm from the gas-phase peak [77, 78, 79, 80]. Figure 2.5 shows a representative spectrum from a healthy human subject, reproduced from [81].
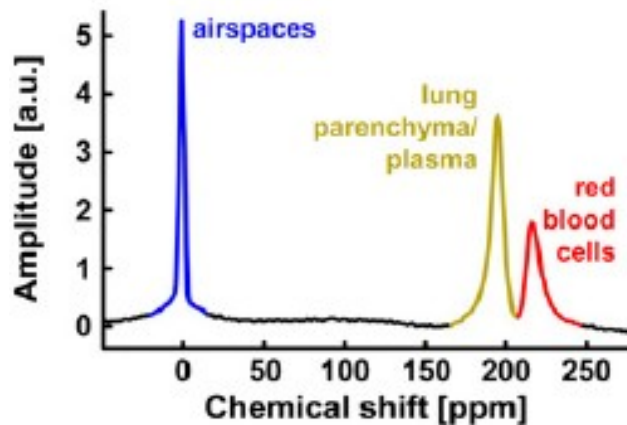
Figure 2.5. Representative ^{129}Xe spectrum from a healthy human subject, showing peaks at 0 ppm (gas-phase), 198 ppm (lung parenchyma/plasma) and 218 ppm (red blood cells). Adapted from [81] with permission.

Dissolved-phase xenon is in dynamic equilibrium with xenon in airspaces, driven by diffusion. The associated continual exchange of xenon atoms between the gas and dissolved compartments, which have distinctly different resonance frequencies, permits gas uptake and exchange to be assessed using hyperpolarized ^{129}Xe MRI. The quantitative characteristics of the exchange and uptake processes are determined by physiologically relevant parameters, such as the thickness of the blood-gas barrier [82], the ratio of the functional tissue volume to alveolar volume [83], and the surface-to-volume ratio [84].

2.6.2 MR Imaging of the Lung utilizing Dissolved-phase Xenon

Even though the fraction of xenon dissolved in the lung parenchyma and blood is small, early studies of the human lung proved it was possible to detect these compartments of dissolved-phase ^{129}Xe in whole lung spectra [79]. Images of dissolved-phase ^{129}Xe were subsequently acquired in small animals by using multiple inhalations of hyperpolarized gas [82, 85, 86]. However, such a multi-inhalation

protocol is not currently applicable to human studies. Muradian et al. [87] also demonstrated the possibility of obtaining gas-phase and dissolved-phase images in humans at low field strength (0.2T) by decomposing the total xenon signal using the 3-point Dixon method. With recent improvements in gas-polarization systems [88], liter quantities of hyperpolarized ^{129}Xe can be obtained with sufficiently high polarization to permit direct imaging of the dissolved phase in humans during a single breath-hold period.

In 2010, Cleveland et al. presented direct 3D imaging of ^{129}Xe dissolved in lung tissue and blood, using a 3-lobe sinc excitation RF pulse (applied 3826 Hz higher than the gas-phase peak) and a pseudo-randomly ordered radial pulse sequence [89]. This study represented a key milestone for the hyperpolarized-gas imaging field. Limited by gas polarization (5%-9%) and also a relatively long acquisition time, ^{129}Xe dissolved-phase images were not acquired simultaneously with ventilation images (which were acquired in a different breath-hold using a multi-slice 2D SPGRE sequence), although imperfection of the excitation RF pulse still excited a small fraction of the gas-phase signal (see below). Figure 2.6 shows 3D dissolved-phase images and multi-slice 2D gas-phase images acquired in a healthy subject with different spatial resolutions (reproduced from [89] with permission). Even though relatively high similarities were found between the dissolved-phase images and ventilation images as seen in the overlaid images (Figure 2.6C), mismatches are also seen. Because the absolute dissolved-phase signal intensity has no physical meaning, it is hard to distinguish pathological alterations in ventilation from those in tissue microstructure or blood flow, or to quantitatively analyze the associated information on lung-function available from such images, without

normalization of the dissolved-phase images to gas-phase images acquired simultaneously with the same resolution. Concerning incidental excitation of the gas-phase signal, Figure 2.7 shows a representative [129]Xe dissolved-phase image versus a control image acquired in the same position and in the same subject using identical acquisition parameters except the RF pulse was centered 3826 Hz below the gas peak (adapted from [89] with permission). Clearly, some gas-phase signals were detected in the control image, while ideally only thermal noise would be present in the control image.
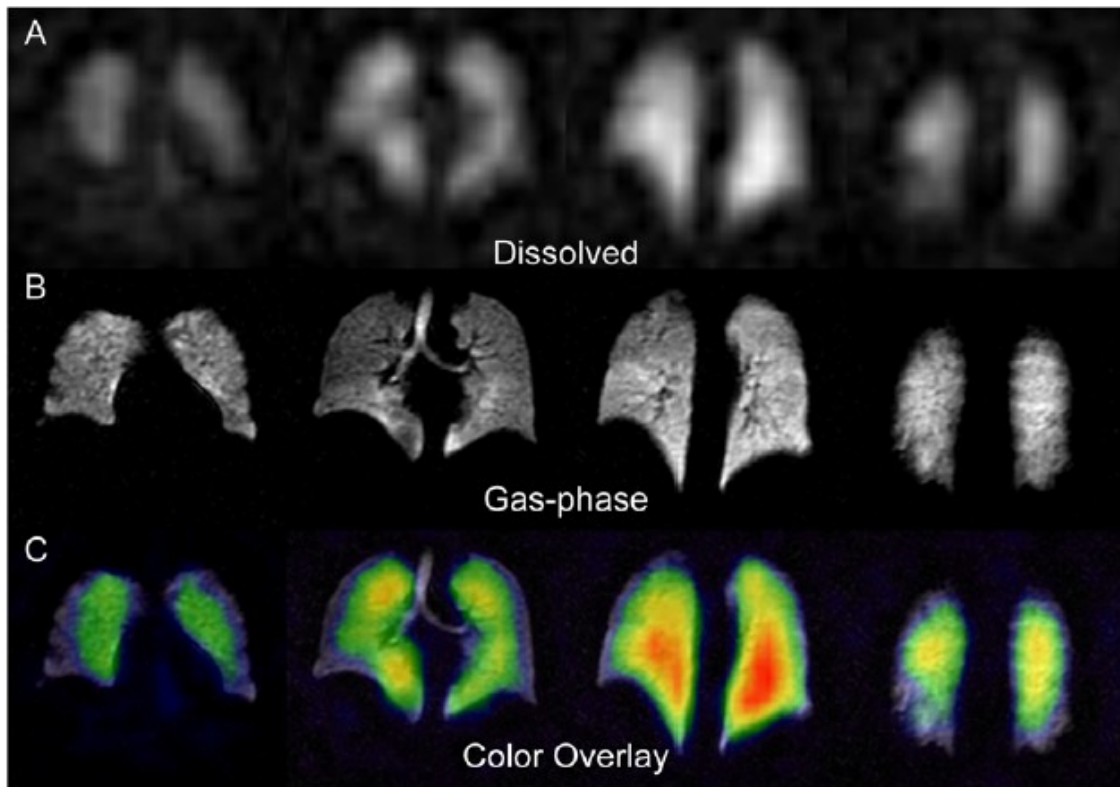
Figure 2.6.   3D [129]Xe dissolved-phase images (A, resolution 12.5*12.5*15 mm^3) and 2D ventilation images (B, resolution 3.2*3.2*15 mm^3) acquired in different breath-holds in a healthy subject. C. Dissolved-phase [129]Xe images from A displayed in color and overlaid on grayscale ventilation images from B.   Images reproduced from [89] with permission.

The large difference in chemical shift between dissolved-phase and gas-phase ^{129}Xe provides the possibility to acquire both components in the same image within one breath hold [81]. The simultaneously acquired ventilation images with matched spatial resolution provide an ideal basis for normalizing the dissolved-phase images, making regional quantification of gas uptake possible.
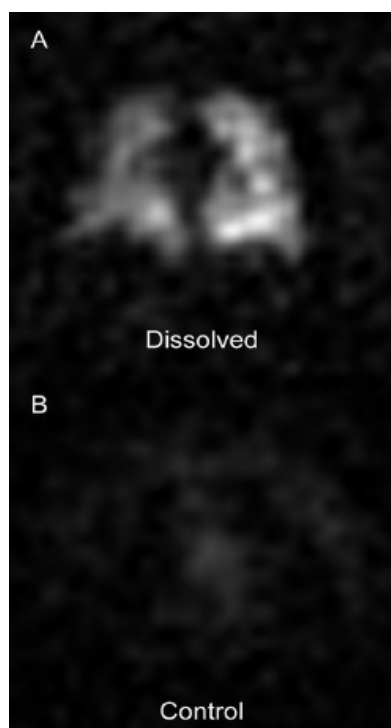
Figure 2.7. Representative dissolved-phase image (A), using an RF pulse centered 3826 Hz above the gas-phase resonance frequency, and control image [B] using identical acquisition parameters except the RF pulse was centered 3826 Hz below the gas peak. Images reproduced from [89] with permission.

The simultaneous acquisition of 3D dissolved-phase and gas-phase images in the human lung was realized in this fashion as described in [81]. A truncated sinc pulse was used to excite both the dissolved-phase and gas-phase ^{129}Xe signals at the same time; the gas-phase signals were excited using a small sidelobe in the RF-pulse excitation profile, as Figure 2.8A shows. The dissolved-phase and gas-phase images were separated in the frequency-encoding direction upon Inverse Fourier Transform (Figure 2.8B). A disadvantage of this method is that spatial resolution and receiver bandwidth are

inherently linked, so increasing the spatial resolution in the frequency-encoding direction requires the bandwidth to decrease, which in turn increases chemical-shift displacement along the frequency-encoding direction between the parenchyma/plasma and RBC components of the dissolved-phase signal, and forces a longer minimum TE unless half-echo sampling is used. A relatively long TE is problematic because T_2^* values for the dissolved-phase components are quite short (~2 ms) [90]. Another disadvantage is that the method cannot depict the parenchyma/plasma and RBC components separately, because of the relatively long TE and bandwidth limitations.
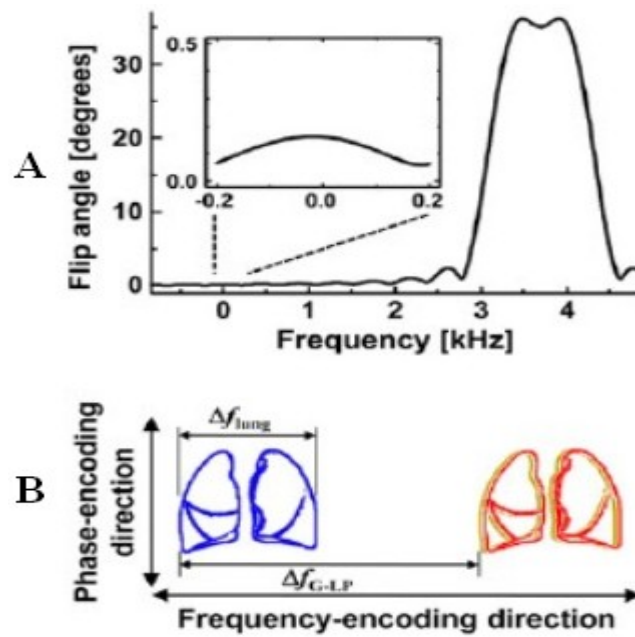
Figure 2.8. A.) Frequency response of the RF pulse used for the simultaneous acquisition in [81]. B.) Dissolved-phase and gas-phase components are separated along the frequency-encoding direction by properly choosing the imaging parameters. Adapted from [81] with permission.
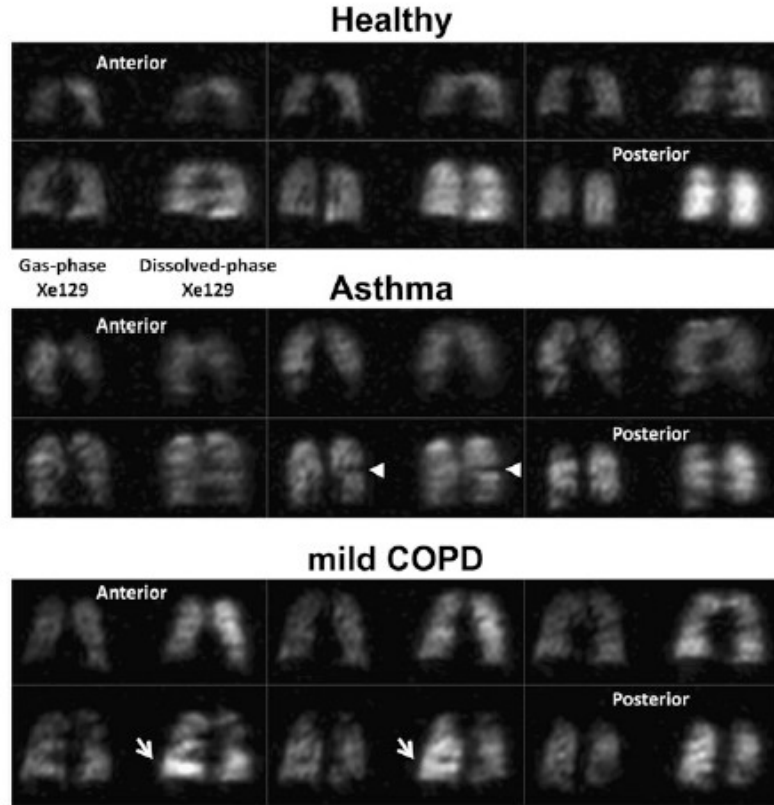
Figure 2.9. 3D images acquired in healthy (top), asthmatic (middle) and mild COPD subjects (bottom) [81]. Each panel shows the central six 20-mm-thick ^{129}Xe images (each slice contains gas-phase image on the left and dissolved-phase image on the right) from the respective acquisition. Sequence parameters included: TR 50ms, TE 2.8ms, flip angle at dissolved-phase 20°, bandwidth 110 Hz/pixel (6.2 ppm/pixel), and resolution 12x12x20mm^3. Images adapted from [81] with permission.

Figure 2.9 shows representative images acquired using the pulse sequence proposed in [81]. Relatively uniform distribution of signal is seen in both ventilation and gas-uptake images obtained from healthy subjects, while marked mismatching between ventilation and gas-uptake was detected in the two diseased subjects. Also note the relatively low SNR in the dissolved-phase images for all subjects.

For better assessment of the lung function using dissolved-phase xenon, we seek to simultaneously acquire dissolved-phase and gas-phase signals with higher image quality. Furthermore we attempt to separate the two components of dissolved-phase signals: xenon dissolved in lung parenchyma/plasma, and xenon dissolved in red blood cells, which will possibly provide clearer and more valuable information on lung function.

2.7 The Goal of this Dissertation Research

As noted in Chapter 1, the goal of this dissertation is to advance hyperpolarized-gas MRI by addressing three specific needs: (1) implementing robust and rapid calibration of the MR-scanner transmitter using negligible HPG magnetization; (2) accelerating combined acquisition of hyperpolarized-gas and proton image sets during a single breath hold; and (3) realizing quantitative regional assessment of gas uptake by lung tissue and blood using ^{129}Xe.   Our goal is achieved through the following three specific aims.

2.7.1 Specific Aim 1

Specific Aim #1 is to design and implement an optimized phase-based transmitter calibration method that yields accurate results from only a small fraction of the hyperpolarized-gas magnetization, and to validate this method against a commonly-used amplitude-based method in human subjects.   To permit integration at the beginning of any imaging pulse sequence, the proposed method requires less than 100 ms, and consumes no more than 5% of the hyperpolarized magnetization.   The method is designed to yield results comparable to the reference amplitude-based approach in the presence of B_0 and B_1 inhomogeneity representative of that encountered in human lung imaging.

2.7.2 Specific Aim 2

Specific Aim #2 is to accelerate the combined acquisition of ^{3}He and ^{1}H 3-D image sets by using the compressed sensing technique to achieve a breath-hold duration which is less than one-half of that required for the conventional approach. The undersampling pattern and reconstruction quality for both ^{3}He and ^{1}H imaging are evaluated using simulations based on fully-sampled data sets and using direct comparison of fully-sampled and undersampled data from the same subject. Finally, the performance of the accelerated and conventional acquisitions in depicting ventilation defects is compared in subjects with pulmonary disease.

2.7.3 Specific Aim 3

Specific Aim #3 is to develop an MRI pulse sequence that permits regional quantification of the tissue (lung parenchyma/plasma) and RBC fractions of the dissolved ^{129}Xe signal, relative to the associated gas ^{129}Xe signal, from a breath-hold acquisition of less than 20 s. This technique is tested in healthy subjects and validated against spectroscopic measurements of the dissolved-phase ^{129}Xe components in the lung. Finally, a pilot study is performed to compare tissue/RBC fractions in healthy subjects to those in at least 5 subjects with pulmonary disease.

Chapter 3

Implementation of Phase-based Calibration Method for Hyperpolarized Gas Studies

3.1 Introduction

3.1.1 Phase-based B_1 Mapping and Calibration Methods

For HPG imaging it would be desirable to have a calibration pulse sequence which is accurate, short and consumes just a small fraction of the total magnetization, and thus can be integrated into the beginning of any acquisition method. As an initial attempt, a low-flip-angle, phase-based method using composite hard RF pulses was described for calibrating the transmitter voltage when imaging hyperpolarized substances [57]. This method drove the magnetization in a square pattern in the transverse plane, returning it almost to the origin with each "cycle" of the pulse.   The phase of the final transverse magnetization was found to be related to the flip angle (α) for each segment of the composite hard RF pulse, as Figure 3.1 shows.   Analogous to most of the phase-based methods, to remove phase shifts from other sources, two measurements with different flip angles were performed, one using flip angle α and the other using $\alpha/3$.   The phase difference between these two measurements was calculated and fitted based on a Bloch equation simulation (Figure 3.1b shows examples of the Bloch equation simulation results and measured phase differences) to determine the actual flip angle, and thus the transmitter calibration voltage.   Several optimizations were made to improve the

sensitivity of this approach to B_1 variation, such as using flip angles of α and $-\alpha$ [58], breaking the transverse pathway into more sides, or using a pre-excitation RF pulse [59]. Nonetheless, further assessment showed that these methods yield relatively large error when the B_0 field is inhomogeneous [60].

At roughly the same time, Sacolick et al. [61] proposed a novel B_1 mapping method based on the Bloch-Siegert shift, which represents the shift of the precession frequency when spins experience RF pulses that are off-resonance or that do not excite any transverse magnetization [62, 63, 64]. The net result of an off-resonance RF pulse is the Bloch-Siegert phase shift φ_{BS}. The equations below (Eq. 2.1 and Eq. 2.2 reproduced from [61]) give the relationship among φ_{BS}, the B_1 field for an RF pulse of amplitude $B_1(t)$ and frequency $\omega_{RF}(t)$.

$$\varphi_{BS} = B^2_{1,peak} \int_0^T \frac{(\gamma B_{1,normalized}(t))^2}{2\omega_{RF}(t)} dt = B^2_{1,peak} \times K_{BS}$$

[Eq. 2.1]

$$B_1(t) = B_{1,peak} \times B_{1,normalized}(t)$$

[Eq. 2.2]

K_{BS} is the Bloch-Siegert shift constant of the RF pulse, and $B_{1,peak}$ is the maximum amplitude of the off-resonance RF pulse.

Viewing these phase-based calibration methods in light of the formalism presented by Sacolick et al [61] reveals that the sidelobe behavior of the off-resonance portion of the calibration pulse is critical for maintaining accuracy in the presence of off-resonance signals, especially when the prepulse part of the calibration pulse sequence has a low flip angle as may be dictated by peak B_1 limitations, which occur in practice due to the relatively low output power for the typical broadband RF transmitter available on

commercial MR scanners, or may be required so that the calibration consumes only a small fraction of the available magnetization, which is desirable for HPG applications.
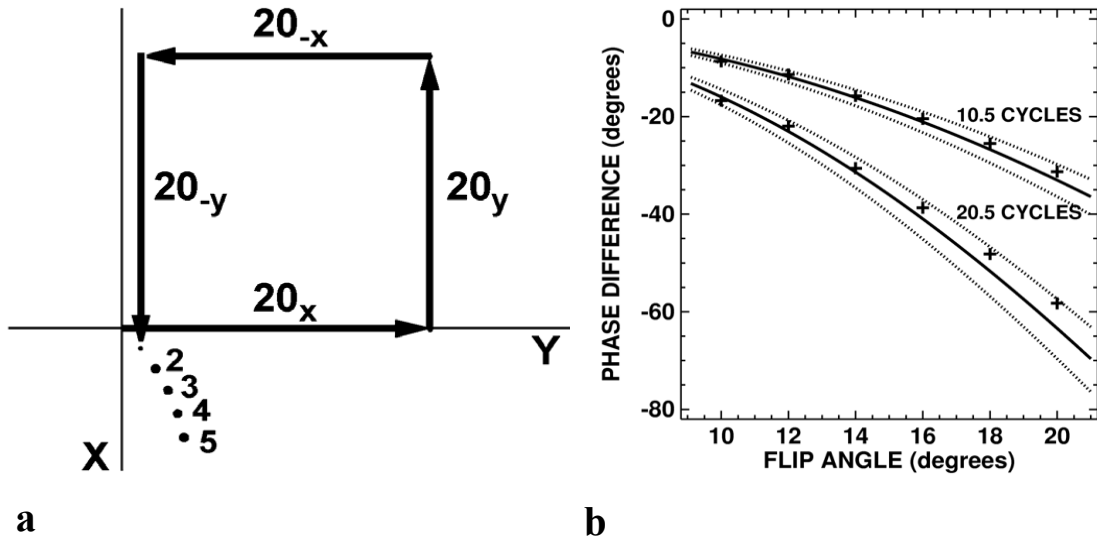
Figure 3.1.   a.) Path of the magnetization in the transverse plane for a $20°_x$, $20°_y$, $20°_{-x}$, $20°_{-y}$ composite RF pulse b.) Theoretical (lines) and experimental (+) phase differences versus flip angle for 10.5-cycle (4 ms) and 20.5-cycle (8 ms) RF pulses. Both diagrams reproduced from [57].

By combining the previous work [57, 58, 59, 60] and Bloch-Siegert shift theory [61], we demonstrate for Specific Aim 1 that a low-flip-angle, phase-based method can be obtained which is robust to B_0 inhomogeneity effects even for relatively low peak B_1 values, and thus would be practical for hyperpolarized-gas studies. Since the proposed method consumes only a small amount (< 5%) of the hyperpolarized magnetization and is relatively fast (< 100 ms), it can be integrated into the beginning of any imaging pulse sequence without substantial effect on the image quality, and easily repeated as needed without requiring additional hyperpolarized gas.

3.1.2 Relationship between Phase-based Calibration/B_1 Mapping Methods and Bloch-Siegert Shift Theory

Although not recognized in the original formulations, the phase-based hyperpolarized-gas transmitter-calibration methods, as described in detail in Section 3.1.1, are actually based on the Bloch-Siegert (BS) shift associated with off-resonance RF pulses [61]. Recalling the hard-pulse approximation concept used in Shinnar-Le Roux (SLR) RF-pulse design [92], methods for B_1 mapping or transmitter calibration using composite RF pulses with constantly increasing phase, as described for example in refs. [57-60], are based on the BS shift because an RF pulse with constant off-resonance frequency has a constantly increasing (or decreasing) RF-pulse phase and, from a discrete perspective, can be expressed as a series of hard pulses with varying amplitude and phase values (that is, as a composite RF pulse).

Consider the example shown in Figure 3.2, which includes three types of RF pulses: (1) four cycles of a 4-part composite RF pulse (normalized amplitude 1, phase 0°, 90°, 180°, 270°) applied in 2 ms; (2) four cycles of an 8-part composite RF pulse (normalized amplitude 1, phase 0°, 45°, 90°, 135°, 180°, 225°, 270°, 315°) applied in 2 ms; and (3) a 2-ms hard RF pulse applied at an off-resonance frequency of 2 kHz. Figure 3.2a plots the corresponding frequency excitation profiles, while Figure 3.2b shows the phase shift versus peak B_1 values for these three types of RF pulses. (For the composite RF pulses, the phase shift is calculated from the transverse magnetization obtained after applying the anti-clockwise and clockwise forms of the pulses, while for the off-resonance hard RF pulse the phase shift is calculated from the transverse magnetization obtained after applying the pulses at positive and negative off-resonance frequencies.) Both figures

show the trend that as higher time resolution (that is, more phase steps per cycle) is used for the composite RF pulse, the behavior of the composite RF pulse approaches that of the off-resonance hard pulse. In particular, the phase shift per unit B_1 increases and approaches the theoretical value predicted by Bloch-Siegert shift theory (Eq. 2.1, 2.2; red line in Figure 3.2b), which indicates that the composite RF pulse methods are actually using the Bloch-Siegert shift, but at lower temporal resolutions.

a   b
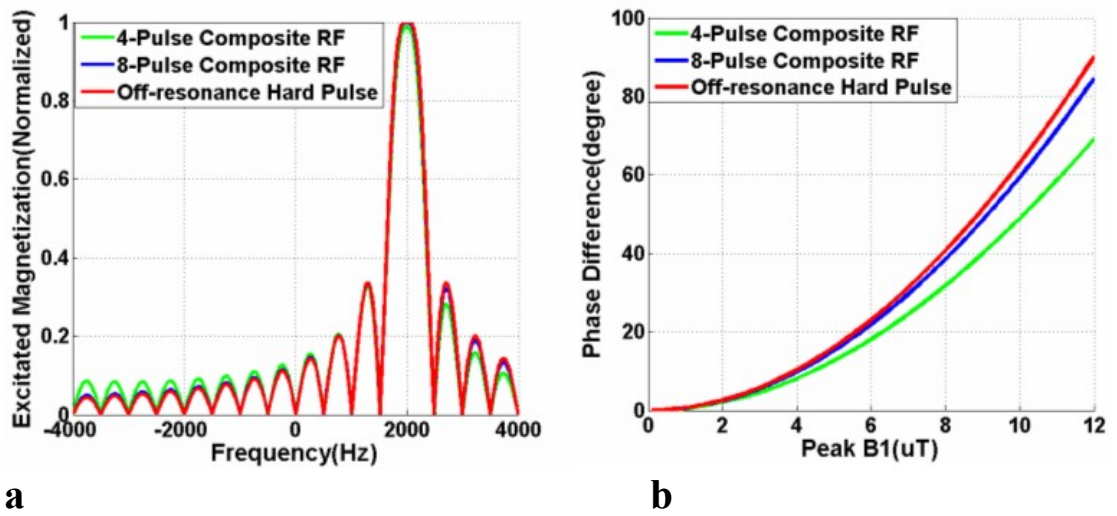
Figure 3.2. Relationship between composite RF pulses and an off-resonance hard RF pulse for the phase-based calibration/B_1 mapping method. (a) Frequency excitation profiles and (b) phase-shift versus peak B_1 value for 4-part and 8-part composite RF pulses and a hard RF pulse applied 2 kHz off-resonance.

3.1.3 Influence of B_0 and B_1 Field Inhomogeneity

The original implementations of the phase-based transmitter calibration method, based on composite hard RF pulses, are relatively more sensitive to B_0 inhomogeneity than B_1 inhomogeneity [60]. To obtain a clearer view of their performance, we

designed and implemented simulation tests for two phase-based methods using composite RF pulses (Method 1, phase-based method using composite RF pulses rotating in a circular trajectory; Method 2, phase-based method applying composite RF pulses in a circular trajectory after a pre-excitation RF pulse, as proposed by [59]) and for the amplitude-based calibration method [54] used in our hyperpolarized-gas studies (designated Method 3). The flip angle estimated by each method was calculated for two cases: (1) assuming a normal distribution of flip angles (to simulate B_1 inhomogeneity), and (2) assuming the flip angle is uniform but there is a normal distribution of off-resonance frequencies (to simulate B_0 inhomogeneity). The normal distributions were truncated at twice the full width at half maximum (FWHM) value. For B_1 inhomogeneity evaluations, the mean flip angle (FA_mean) for the distribution was varied between 10° and 40° per cycle for Methods 1 and 2, and between 5° and 30° for Method 3. (These values were chosen based on reasonable operating conditions for human imaging.) FWHM values for the flip-angle distributions (FA_fwhm) of 10%, 50% and 100% of FA_mean were considered. For B_0 inhomogeneity evaluations, FWHM values for the frequency distributions (FR_fwhm) of 1, 3 and 5 ppm were considered. Figure 3.3, reproduced from [60], shows the simulation results. In the presence of B_1 inhomogeneity, the behavior of the two phase-based methods is better than that for the amplitude-based method since the former methods yield approximately constant error regardless of the mean flip angle, and the error is relatively small unless the B_1 inhomogeneity is quite large. In contrast, the amplitude-based method is largely immune to B_0 inhomogeneity, while both phase-based methods show a high sensitivity to B_0 inhomogeneity, particularly at low flip angles. This is important for hyperpolarized-gas studies, because

most of these studies operate in this range because of the non-equilibrium nature of hyperpolarized magnetization. So we need a better off-resonance pulse which is robust to B_0 inhomogeneity effects even when working with low flip angles.
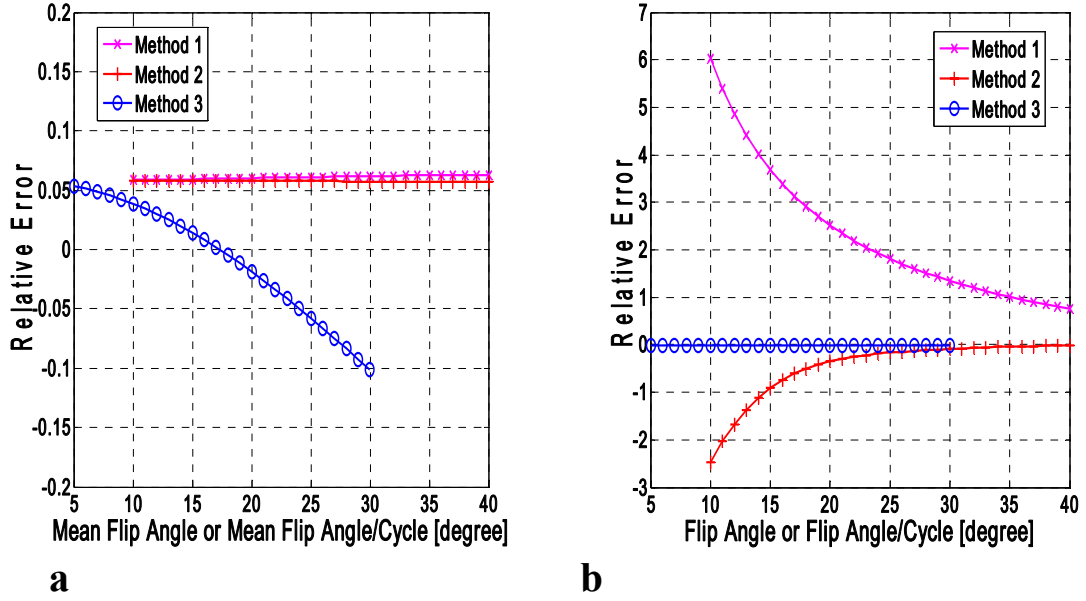
Figure 3.3. a.) Performance of three calibration methods in the presence of B_1 inhomogeneity for FA_fwhm=50% of the mean flip angle. b.) Performance of three calibration methods in the presence of B_0 homogeneity for FR_fwhm = 5 ppm.

3.2 Methods

3.2.1 Sequence Design

The sidelobe response of the off-resonance pulse directly determines robustness of the phase-based method to B_0 inhomogeneity effects (Figure 3.2a shows sidelobes of hard RF pulses), especially when a low-flip-angle excitation RF pulse is used and the calibration pulse sequence is operated at relatively low B_1. The Fermi pulse used in [53, 61] as the off-resonance pulse already has a comparatively low sidelobe. But for our

purposes, because we want to use minimal magnetization to yield relatively accurate calibration results, we cannot collect a spin echo signal, and so a Fermi pulse is not robust enough (shown in Figure 3.5). We thus designed a 10-ms SLR RF-pulse which has very "clean" sidelobe performance (that is, very low sidelobes) using the open-source MATPULSE tool (version 5.1) [93] (designed at flip angle 90°, time-bandwidth product 0.8 kHz, passband ripple 200%, rejection band ripple 1.e-6). The sensitivity (applied flip angle versus resulting phase difference) corresponding to the 10-ms SLR RF pulse is shown in Figure 3.4.
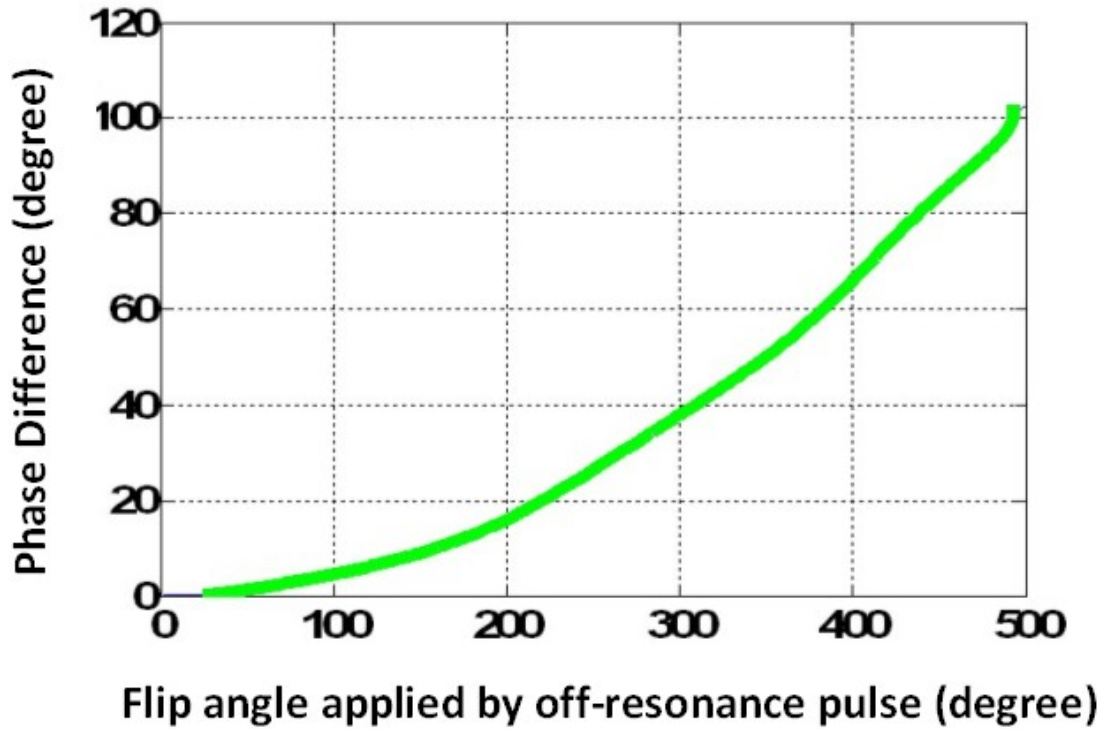
Figure 3.4. Sensitivity of the proposed phase-based calibration method using an SLR RF pulse [94]: applied flip angle versus resulting phase difference.

To evaluate theoretically the performance of this SLR pulse in an inhomogeneous B_0 field, a simulated normal distribution of off-resonance frequencies with a frequency resolution of 32 Hz, truncated at twice the full width at half maximum (FWHM) value of

320 Hz (6.6 ppm for ^{3}He at 1.5T) was used, while B_1 was assumed to be homogeneous. The performance of the phase-based method using the 10-ms SLR pulse and a Fermi RF pulse, which has been proposed in the literature for Bloch-Siegert B_1 mapping [61], was simulated at peak B_1 values ranging from 1 to 10 µT, with a step size of 0.1 µT. Predicted B_1 values from the two methods were compared with the corresponding input B_1 values to calculate the fractional error. Excitation RF pulses were set to 5° for a peak B_1 of 10 µT with a duration of 0.4 ms, which would be suitable for the transmitter-calibration procedure to be integrated with other pulse sequences. To provide a fair comparison, we chose pulse durations and off-resonance frequencies that yield the same sensitivity (the same K_{BS}). These values were: SLR RF pulse with duration of 10 ms applied at 1.5 kHz off resonance, and Fermi pulse with duration of 10 ms applied at 3.5 kHz off resonance. The performances of phase-based calibration methods using the SLR pulse and the Fermi pulse in the presence of B_0 inhomogeneity are shown in Figure 3.5.


a   **b**
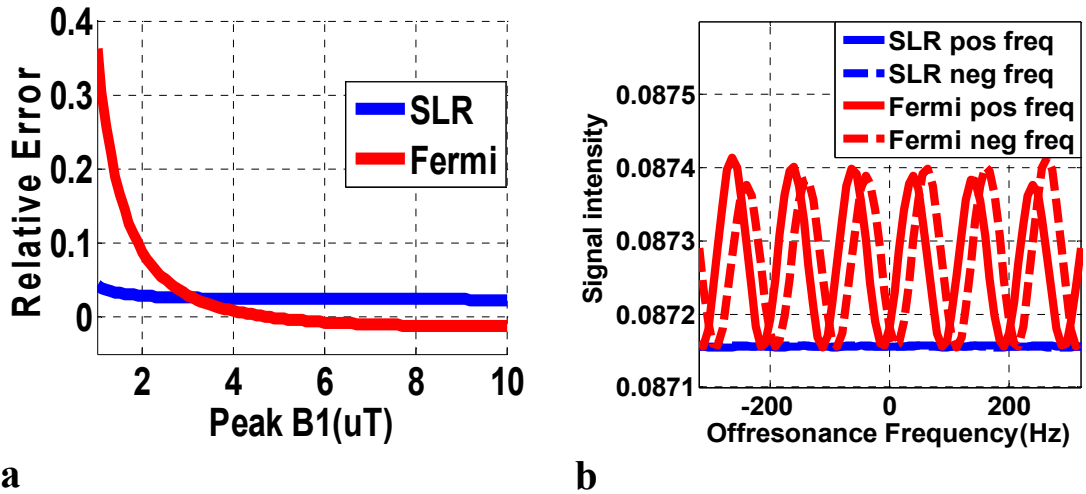
Figure 3.5.   a.) Performance of SLR and Fermi off-resonance RF pulses for normally distributed B_0 inhomogeneity. b.) Signal intensity variation near resonance that results from applying SLR or Fermi off-resonance RF pulses.

Both methods show a tendency of better performance towards higher peak B_1 values, which is due to the larger signal obtained from the excitation and the larger phase shift with increasing B_1. This trend is more obvious for the Fermi off-resonance RF pulse than for the SLR pulse, especially when the peak B_1 is below 3 μT. This difference would become larger (smaller) if the flip angle of the excitation RF pulse were decreased (increased), and is caused by on- or near-resonance magnetization unintentionally excited by the off-resonance RF pulse; the degree of this excitation is related to the rejection band ripple of the pulse. In the lower peak B_1 region, since the signal amplitude and phase shift are both relatively smaller, the phase of the integrated signal is more easily affected by magnetization excited by the rejection band of the off-resonance RF pulse. This effect also becomes larger at lower peak B_1 because more magnetization is left along the longitudinal axis. The effect of the unintended excitation from the off-resonance RF pulse can be seen in Figure 3.5b, which shows the signal intensity calculated at frequencies from -320 to 320 Hz (-6.6 to 6.6 ppm for ^{3}He at 1.5T) after applying the excitation RF pulse with a flip angle of 5° followed by either the SLR or Fermi off-resonance RF pulse applied with a peak B_1 of 10 μT, at both positive and negative frequencies. Greater signal oscillation is seen for the Fermi RF pulse, and the difference in the response for a positive versus negative off-resonance frequency degrades the result when integrated over signals from different off-resonance frequencies. The signal intensity performance for the SLR RF pulse is much better, although the SLR pulse has a somewhat larger phase variation for this case (result not shown). This poorer performance of the SLR RF pulse in phase variation leads to a larger error at high peak B_1 values compared with the Fermi RF pulse. For example, at 10 μT, the relative error

from the method using the SLR pulse is 2.3%, while that for the Fermi RF pulse is -1.2%. Nonetheless, this is not a significant issue for hyperpolarized-gas applications, which normally operate at peak B_1 values well below 10 μT.

Based on this SLR pulse, we implemented a gradient-echo-based pulse sequence for the phase-based transmitter calibration as illustrated by the pulse-sequence diagram shown in Figure 3.6. Two repetitions (only one of them shown in Figure 3.6) are included in the measurement, and each starts with a 0.4-ms non-slice-selective excitation RF pulse, followed by a 10-ms off-resonance SLR RF pulse (as discussed above) applied at +1.5 kHz relative to the ^{3}He resonance frequency for the first repetition and at -1.5kHz for the second, with K_{BS} = 50 radians/gauss^2 for each off-resonance RF pulse. The phase shift to flip angle (B_1) calibration for the off-resonance SLR RF pulse is calculated by a numerical Bloch equation simulation (see Figure 3.4). A gradient echo is obtained using a standard frequency-encoding gradient applied along the head-foot direction (from apex to base of the lung). Bipolar, sinusoidal spoiler gradients are applied at the end of each repetition to eliminate remaining transverse magnetization through gas diffusion. (A sinusoidal waveform is used to decrease eddy currents, which could result in an unintended phase shift between the two repetitions.) The TR is less than 30 ms, which should essentially eliminate any effects of motion between the two repetitions. For typical operating conditions, the peak B_1 of the SLR off-resonance RF pulse is between 2 and 6 μT.
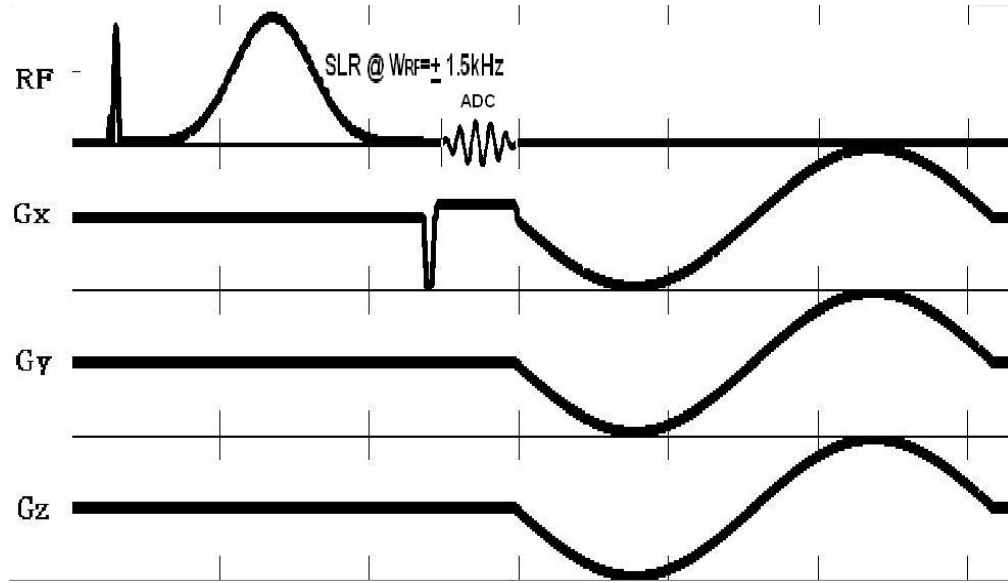
Figure 3.6. Sequence timing diagram for the phase-based calibration method. The SLR RF pulse is applied at ±1.5kHz with a duration of 10ms; only one acquisition is shown in the diagram.

As noted above, the signal is spatially resolved in the head-foot direction using a frequency-encoding gradient. Typical parameters include a receiver bandwidth of 390 Hz/pixel with 128-point resolution over a 300-mm field of view, so the signal from each point (following iFFT) corresponds to an axial slab of the lung with a thickness of 2.3 mm.

3.2.2 Calculation of Transmitter Voltage

Under current experimental conditions, we use a relatively low dose for calibration. In some measurements the measured SNR is not very high. Further, since the pulse sequence is based on gradient echo (GRE, as opposed to spin-echo, SE) signals, static field inhomogeneity may result in phase dispersion over the 2.3-mm thick axial slab that corresponds to each data point. For data points associated with significant B_0

inhomogeneity within the axial slab, wherein the signal intensity decreases due to phase cancellation, we found that phase values would be corrupted by several degrees or even tens of degrees depending on the seriousness of the cancellation (the SNR issue will be further discussed in Section 3.3).   To help mitigate this problem, noise and peak-signal thresholds are applied based on the signal magnitudes; the phase values from the resulting "valid" positions are weighted by the corresponding signal magnitudes and then averaged to yield the flip angle (B_1). The processing of the calibration data is split into the following four steps, as Figure 3.7 shows:

1.) Determine the lung regions with sufficient SNR. The current calibration procedure used in human studies at our institution is still run separately from the imaging pulse sequences (details are described in Section 3.6). Some studies, especially those using ^{3}He, use a very small dose of gas for calibration. This leads to signals with low SNR (as low as 2-5 for the phase-based calibration). Eq. 3.1 shows the relationship between the standard deviation of the phase value of the signal (in degrees) and the SNR of the magnitude signal. For example, when the SNR of the magnitude signal is 5, the standard deviation of the measured phase, σ_{phase}, is 11°, which is sufficiently large to affect the accuracy of the phase-based calibration method because normally the phase difference measured is in the range from 10° to 40°.

$$\sigma_{phase} = \frac{180^0}{\pi(SNR_{mag})}$$

[Eq. 3.1]

To ensure reasonable accuracy of the phase-based calibration method, two thresholds are applied, and only the regions with signal intensities larger than both of the thresholds are used for subsequent calculations: a.) noise threshold, which is set at 10 times the

standard deviation of the noise and is important for cases which have relatively low SNR; and b.) signal threshold, which is set at 1/8 of the peak signal and is useful for high SNR acquisitions. The specific threshold values were determined heuristically based on typical data from human studies.

2) Calculate the phase difference, after phase unwrapping, induced by the off-resonance RF pulses applied at positive and negative frequencies.

3) Calculate the mean phase difference using the magnitude of the corresponding signal as a weighting factor.

4) Determine the actual mean flip angle (or mean B_1 value) for the region of interest. This value is obtained from the sensitivity curve for the phase-based method, as shown in Figure 3.4, through interpolation or curve fitting. Given the actual mean flip angle, the transmitter calibration voltage is calculated using Eq. 3.2:

$$V_{cal} = \frac{FA_{nor}}{FA_{act}} * V_{app},$$ **[Eq. 3.2]**

where V_{cal} denotes the calculated transmitter calibration voltage, FA_{nor} represents the nominal flip angle applied by the phase-based calibration sequence, FA_{act} corresponds to the actual mean flip angle determined in this step, and V_{app} represents the actual transmitter voltage applied for the phase-based calibration pulse sequence.
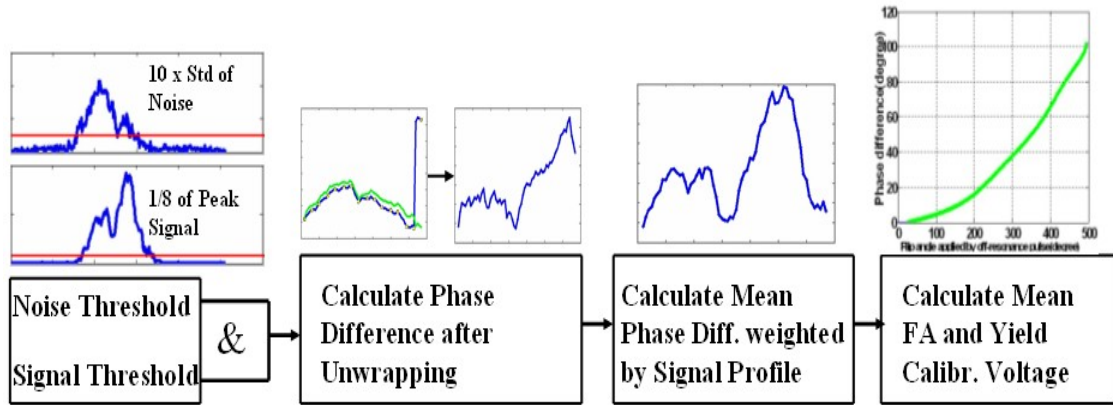
Figure 3.7. Data analysis schematic for the phase-based transmitter calibration method. Four steps are followed to calculate the transmitter calibration voltage.

3.2.3 Verification using B_1 Mapping in Phantom Test

Accurate calibration of the transmitter is crucial to guarantee satisfactory image quality. In this regard, an important step is to verify the calibration accuracy in the presence of both B_0 and B_1 inhomogeneity. Because it is very challenging to obtain three-dimensional B_0 and B_1 maps in conjunction with the calibration results in humans, we designed a phantom test to indirectly verify the performance of the calibration procedure. Two plastic 2-L water bottles, each containing doped water (1.25g $NiSO_4$ and 5g NaCl per L), were placed side-by-side on the scanner table with the long axis of the bottles parallel to the direction of the static magnetic field (i.e., the z axis). This configuration mimics that of the human lung when a subject lays supine on the scanner table. Spatially-registered B_0 and B_1 maps were acquired together with phase-based calibration data (measurement parameters provided below). For comparison to the calibration data, the B_1 map was integrated over axial slices to calculate the average flip angle corresponding to each point along the frequency-encoding (z) direction. To help separate the effects of B_0 & B_1 inhomogeneity, versions of the phase-based calibration

37

based on gradient echoes and spin echoes were tested [53, 61]. In addition, the measured B_0 and B_1 data was incorporated into a theoretical model (based on the Bloch equations) of the calibration procedure to permit comparison of the theoretically predicted performance in the presence of B_1 inhomogeneity to the experimental measurements.

An interleaved 3D gradient-echo pulse sequence was used for both the B_0 and B_1 acquisitions. Pulse sequence parameters included: B_0 map: TE1/TE2 2.0/2.8 ms; flip angle 90°; B_1 map: TE 2.0 ms, flip angle 1/flip angle 2 40°/80°. Common parameters included: TR 2000 ms; spatial resolution 6.2 x 6.2 x 6.2 mm^3; and matrix 64 x 32 x 128. The data were acquired on a 1.5T MR scanner (Magnetom Avanto, Siemens Medical Solutions, Malvern, PA).

3.2.4 Comparison with Amplitude-based Method in Human Studies

For hyperpolarized-gas imaging studies at our institution, we have routinely used a signal-amplitude based iterative method for transmitter calibration [54] (Method 3 mentioned in Section 3.1.3). As noted in Section 2.4, this method is used at the beginning of each imaging session, separate from the image acquisitions, and requires a dedicated inhalation of hyperpolarized gas. The method operates as follows (see also Section 2.4 and Figure 2.3). Starting with a transmitter setting that yields a flip angle known to be less than 12°, a series ("block") of 32 excitation RF pulses are applied (TR 9.1 ms), each using the same transmitter setting. The magnitude of the MR signal is sampled following each RF pulse, and spoiler gradients are applied before application of the next RF pulse. A relatively short TR is chosen to avoid unnecessary contamination of

the flip-angle measurement by T_1 relaxation. After each block of 32 RF pulses, the transmitter setting is doubled, and another block of 32 RF pulses is applied. This procedure is repeated until the transmitter setting reaches a pre-set transmitter voltage limit. The actual flip angle is then calculated by fitting a mono-exponential decay to the data from the "optimal" block, which is the block with the highest signal from its first excitation.

To obtain a fair evaluation of our proposed phase-based transmitter calibration method using an SLR RF pulse, we implemented a pulse sequence that combines our phased-based method proposed in Sections 3.2.1 and 3.2.2 with the amplitude-based method as described above and in [54]. Thus, one calibration dose of hyperpolarized gas yields both phase-based and amplitude-based results. Figure 3.8 shows the flow chart for this pulse sequence. The phase-based method is executed first because it consumes only a small fraction of the magnetization. The combined pulse sequence was used to obtain transmitter calibration data for ^{3}He and ^{129}Xe imaging studies performed at our institution in healthy subjects and in subjects with lung disease. Comparison data from more than 100 studies has been obtained.

3.2.5 Measuring the Magnetization Consumption of Phase-based Calibration Method

One of the advantages of the phase-based calibration method is that much less magnetization (less than 5% of the initial magnetization) is required compared to the amplitude-based method (almost complete depletion of the initial magnetization). To obtain a direct measurement of the SNR reduction associated with the phase-based calibration sequence, we designed an experiment based on a ventilation-imaging pulse

sequence: 1.) ventilation imaging only; 2.) phase-based calibration sequence followed by ventilation imaging in one breath hold. A balanced steady-state free-precession ("TrueFISP") pulse sequence was used as the ventilation-imaging sequence.

| Frequency calibration | → | Phase-based transmitter calibration | → | Amplitude-based transmitter calibration |
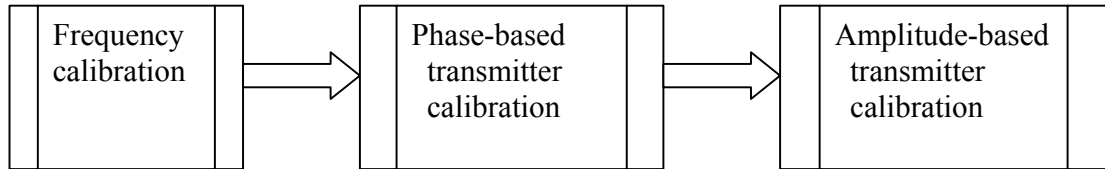
Figure 3.8. Flow chart of the pulse sequence used for calibration at our institution, combining both amplitude-based and phase-based calibration methods.

3.3 Results

3.3.1 Verification using B_1 Mapping in Phantom Test

Our preliminary theoretical analysis (Section 3.1.3) indicated robustness of the phase-based calibration method using an optimized SLR RF pulse even for relatively severe B_0 and B_1 inhomogeneity, and especially for B_0 inhomogeneity. Thus, we expect that the phase behavior of the (gradient-echo-based) calibration method throughout the phantom will be consistent with the performance predicted theoretically based on the B_0 and B_1 maps, and also consistent with the spin-echo version of the phase-based method proposed by [53], which serves as a secondary reference. In the phantom tests, the neck and bottom regions of the bottles generally showed the most B_0 inhomogeneity. In regions with a severely inhomogeneous B_0 field, large phase variations might exist within the slice corresponding to a given point along the frequency-encoding direction. This would induce significant signal cancellation, which would affect the final phase value by

only a small amount if sufficient SNR remains, and also affect the final calibration results if amplitude weighting is used to integrate over a region of interest (ROI).

The phantom test results are shown in Figure 3.9. B_0 and B_1 maps were acquired at the same position and with the same voxel dimension along the frequency-encoding direction as the calibration pulse sequences. As illustrated by the B_1 map at the top of the right column in Figure 3.9, there was B_1 variation from the middle to the edge of each bottle in all three directions, ranging from -20% to -5% of the nominal 40° flip angle. At the bottom of the water phantoms, there was a B_0 field variation in the range from -6 to -1 ppm caused by the susceptibility interface; in the central area, the magnetic field was relatively homogeneous, ranging from -1 to 1 ppm. In some regions of the neck of the bottle, the B_0 field was between +2 and +4 ppm, as indicated by the B_0 map of one of the slices shown at the bottom of the right column in Figure 3.9. The first (left) column of Figure 3.9 shows theoretically predicted profiles of the signal amplitude and phase along the z axis (direction of the static magnetic field), which were derived considering the measured B_1 values for each voxel. Each data point in the profile represents integration over a slice perpendicular to the frequency-encoding direction. Corresponding experimental amplitude and phase profiles from the spin-echo and gradient-echo versions of the calibration pulse sequence are shown in second and third columns of Figure 3.9, respectively. Compared with the amplitude and phase behavior predicted theoretically based on B_1 measurements, the spin-echo based calibration method yielded a more accurate measurement, especially in regions of large B_0 inhomogeneity, such as the top and bottom of the bottles. In these regions, the gradient-echo based method suffered from signal cancellation, indicated by the smaller signal amplitude values measured in

these regions, as shown in the third column of Figure 3.9.   In these regions, the phase

values for the gradient-echo version were also affected by several degrees (lower part of

third column of Figure 3.9), but these values were nonetheless still reasonably close to

the theoretical values.   The results in Figure 3.9 also show that phase errors exist in the

presence of substantial signal cancellation, so using amplitude values as a threshold to

judge the validity of phase-difference values is a useful standard in producing accurate

calibration results from the gradient-echo based transmitter-calibration method.
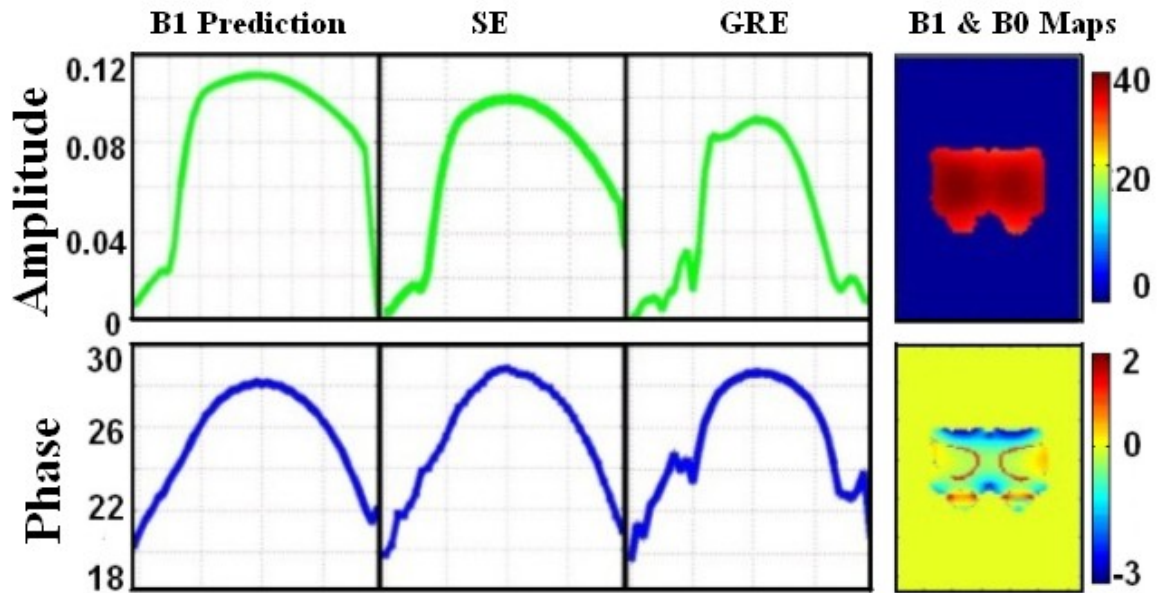
Figure 3.9.   Signal amplitude and phase profiles (unit: degrees) along the long axis of the bottles from the theoretical calculations (left column, predicted based on the B1 mapping results), and the spin-echo (SE [53], second column) and gradient-echo (GRE, third column) versions of the phase-based transmitter calibration method. B_1 (upper, unit: degrees) and B_0 (lower, unit: ppm) maps corresponding to a slice through the center of the bottles are shown in the right column.

3.3.2 Comparison with Amplitude-based Method in Human Studies

For ease of comparison, amplitude-based measurement results are converted to the equivalent phase difference, which the phase-based method would measure for the flip-angle predicted by the amplitude-based measurement, using the following procedure: 1.) The 32-pulse block is chosen which has the highest signal magnitude while yielding calibration results that are no more than 10% different from those for the block immediately before it. (In its standard form, the amplitude-based method picks the "best" block as that with the highest signal magnitude [Figure 2.3], but we found this leads to a 5-15% error in the final estimation in the presence of relatively large B_1 inhomogeneity.) At each readout position for this block, the actual flip angle is calculated based on fitting the signal decay curve consisting of 32 points from the 32 readouts following the repeated RF excitations. 2.) The measured flip angles are used to predict the phase difference that the phase-based method would measure for the corresponding readout position. 3.) Results from both methods are compared at the "valid" positions for the phase-based method, as determined using the criteria illustrated in Section 3.2.2.
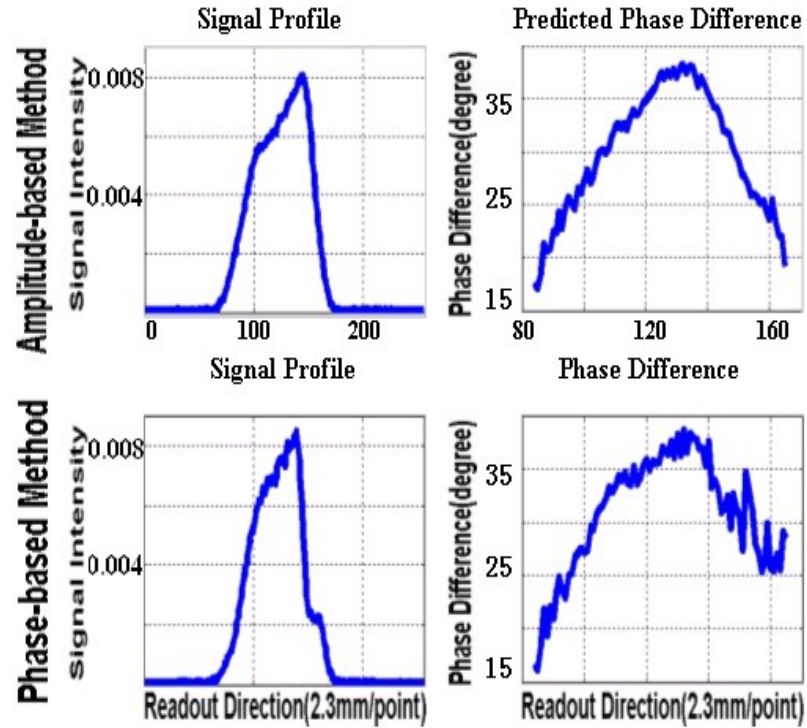
Figure 3.10. Phase-based calibration results and amplitude-based calibration results (converted to equivalent phase differences) obtained in one acquisition from a healthy subject.

Figure 3.10 shows the comparison of the signal-intensity profile and equivalent phase differences for the amplitude-based calibration method to the corresponding values for the phase-based calibration method for a healthy subject who participated in a ^{129}Xe lung-imaging study. The readout direction, shown left to right in the plots, corresponds to the head-to-foot direction in the subject. We see from Figure 3.10 that the signal-intensity profile measured by the phase-based method is very similar to the one measured by the amplitude-based method, except at the base of the lung (readout indices larger than 150). The phase behavior measured by the phase-based method is also fairly close to the predicted results from the amplitude-based method, except at the base of the lung. This is reasonable because, in healthy subjects, the ventilation of the lung is

homogeneous and so the B_0 field is relatively uniform, except at the base of the lung in the vicinity of the diaphragm interface. For example, Figure 3.11 shows measured B_1 mapping results in a healthy subject's lung, reproduced from [57]. The phase difference (Figure 3.11c) is relatively homogeneous except at the base of the lung (arrows in Figure 3.11a, b).
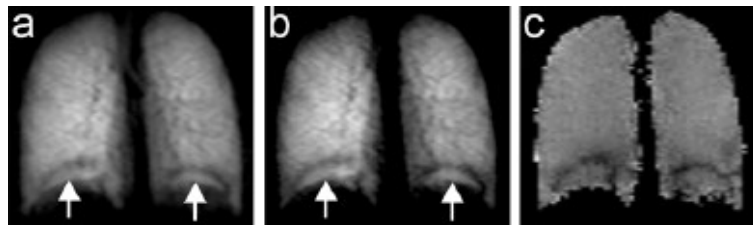
Figure 3.11. Coronal ^{3}He lung images acquired in a healthy subject using the α, α/3 phase-based B_1 mapping method proposed in [57].

For diseased subjects with marked ventilation defects, the signal-intensity profile measured by the phase-based method often appears much noisier than that for the amplitude-based method. Even so, the phase values measured with the phase-based method (after thresholding) generally remain very similar to the predicted values from the amplitude-based method, as shown for a subject with asthma presented in Figure 3.12. Nonetheless, the signal-intensity behavior for the phase-based method affects the associated weighting factors.

Figure 3.12. Phase-based calibration results and amplitude-based calibration results (converted to equivalent phase differences) obtained in an asthmatic subject.
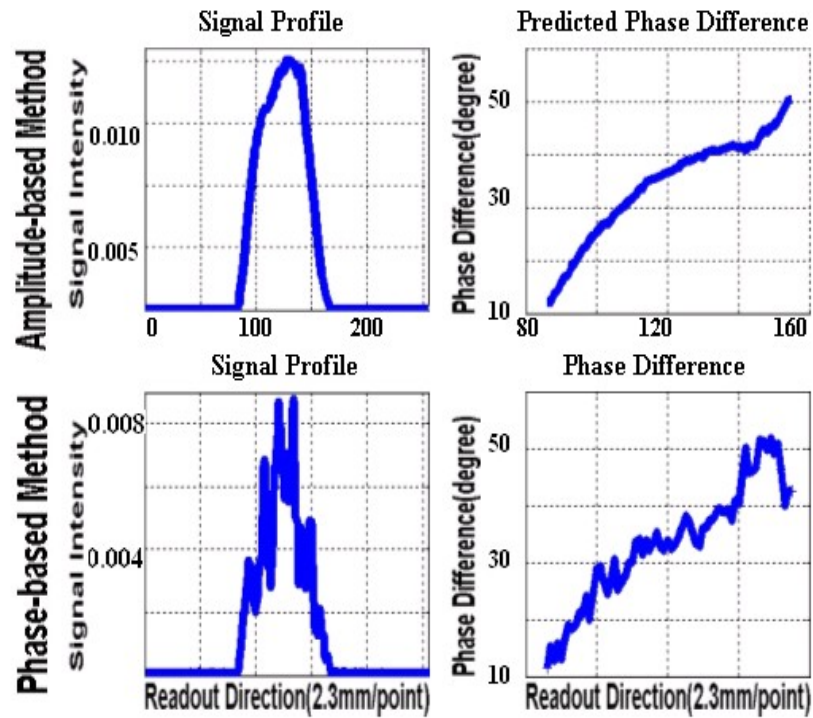
The hybrid phase-based/amplitude-based transmitter-calibration pulse sequence was used to compare the two methods in 81 [3]He and 73 [129]Xe human studies. The correlation coefficient between results from the two methods was 0.99 for [3]He studies and 0.98 for [129]Xe studies (Figure 3.13). The maximum difference between results from the two methods was less than 10%.
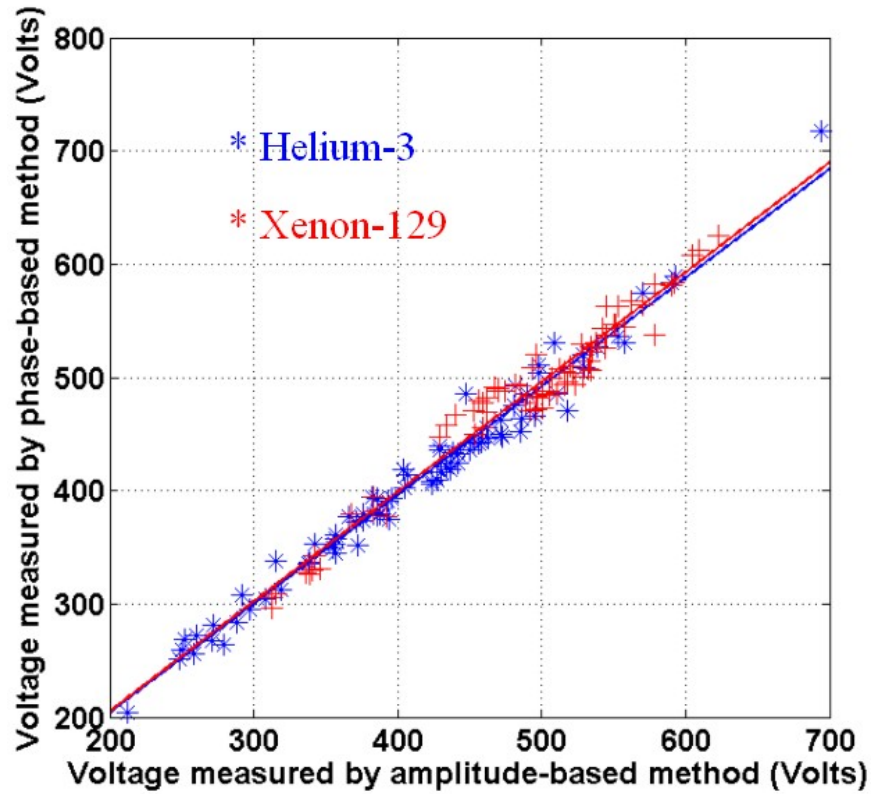
Figure 3.13. Calibration results shown as transmitter voltage measured by the phase-based method versus transmitter voltage measured by the amplitude-based method from all healthy and diseased subjects in ^{3}He and ^{129}Xe studies.

3.3.3 Magnetization Consumption of Phase-based Calibration

Three comparison studies were done to measure the SNR degradation caused by applying the phase-based calibration method before imaging acquisitions. Results are shown in Table 3.1. In general, the SNR values measured from the acquisitions which included the phase-based calibration method were very close to the ones without the calibration. All of the calculated SNR ratios were more than 90%. Theoretically, using a 10° flip angle for the excitation RF pulse of the calibration should consume less than 3%

of the total magnetization, while using a 5° flip angle should consume less than 1%. However, in practice, there are other factors which may affect the accuracy of the estimated magnetization consumption. In particular, the net magnetization in the ^{3}He dose administered to the subject is directly proportional to the resulting image SNR. Errors in estimation of the net magnetization will therefore affect our estimate of the magnetization consumed by the phase-based calibration.

Table 3.1. SNR comparison from image acquisitions without (SNR 1) and with (SNR 2) the phase-based calibration.

	Test 1 (FA=10°)	Test 2 (FA=5°)	Test 3 (FA=5°)
SNR 1/ Dose (mmol)	62.0 / 7.7	87.7 / 8.0	93.9 / 7.7
SNR 2/ Dose (mmol)	59.3 / 7.8	84.4 / 7.9	87.3 / 7.7
SNR Ratio	94%	97%	92%

3.4 Discussion and Conclusion

Compared with the amplitude-based calibration method [54], the phase difference from which B1 is estimated using the phase-based method does not rely on the flip angle of the excitation pulse, but depends on the peak B1, pulse duration and off-resonance frequency of the off-resonant RF pulse, based on the Bloch-Siegert Shift [Eq. 2.1]. Thus the phase-based calibration method can produce valid B1 mapping/calibration results as long as the excited signal is above the noise level. In contrast, the amplitude-based method measures the signal amplitude decaying following the excitation pulses. A few excitation RF pulses with relatively large flip angle or larger number of excitation RF pulses with small flip angle can both yield accurate results, although both of these configurations theoretically consume more magnetization than the phase-based method.

Robustness against B_0 field inhomogeneity is crucial for the phase-based calibration method [60]. Inhomogeneous B_0 field affects the performance of the phase-based calibration method in two respects. First, the off-resonance RF pulse produces unwanted excitation of magnetization from the longitudinal axis; spins located in different B_0 fields experience different B_1 fields from the off-resonance RF pulse, which gives rise to fluctuation of the magnetization excited by the excitation RF pulse, as Figure 3.5 shows. The phase of the signal accumulated from spins located in a wide range of B_0 fields will be affected by this fluctuation. Second, the phase shifts of spins after experiencing the off-resonance pulses are also subject to the B_0 field where the spins are located, as indicated by Eq. 2.1. Theoretical simulation shows the designed SLR pulse, because of its cleaner (lower) side bands, yields less error in Gaussian distributed inhomogeneous B_0 field, compared with the Fermi pulse, when working in low peak B_1 situations. (In higher peak B_1 situations, due to the slightly larger error induced by SLR pulse to the phase shifts, the method using the SLR pulse shows slightly larger error than the one using Fermi pulse.).

Because of the non-equilibrium nature of the hyperpolarized gas signal, the calibration sequence collects a gradient echo signal. A relatively long echo time (about 10ms) is used for the phase-based method because the duration of the off-resonance pulse is proportional to the phase shift obtained based on the Bloch-Siegert shift [Eq. 2.1]. However, on the other hand, this relatively long echo time increases the chance for phase dispersion within the slabs perpendicular to the read-out direction when the B_0 distribution is inhomogeneous, and causes a drop of signal intensities in those regions due to signal cancellation within slabs, such as at the neck and base of the bottles shown in Figure 3.9, and the base of the lung shown in Figure 3.10.

Transmitter calibration provides an average B_1 or flip angle over a volume of interest. In the healthy human lung, except for the B_0 field variation at the air tissue interface near the diaphragm, most of the regions have a relatively homogeneous B_0 field distribution, as Figure 3.11 shows. In diseased subjects, this situation becomes complicated. Nonetheless, with a relatively robust phase behavior, the phase-based calibration method shows consistent results with the amplitude-based method among a large number of human tests. We postulate this was because, even though there was B_0 inhomogeneity within the ventilated region of the human lung, in general most of the regions were still homogeneous or had relatively smooth variations instead of abrupt changes. The influence of the magnetization cancellation in very inhomogeneous B_0 fields was limited in that it did not substantially affect the global calibration value obtained from averaging over the selected ROI.

In conclusion, we implemented a phase-based calibration method for hyperpolarized-gas studies, which has duration of less than 100 ms and consumes less than approximately 5% of the initial magnetization, thus permitting integration into the beginning of any imaging pulse sequence. In theoretical simulations, the phase-based method using the designed SLR pulse showed robust performance against B_0 inhomogeneity effects, yielding less than 5% relative error in the operating range of peak B_1 for HPG calibration procedures (1 μT to 10 μT). Through B_1 and B_0 mapping, phantom tests provided a comprehensive assessment of the phase-based method. Compared with the amplitude-based method [54] and the phase-based method using a spin-echo sequence [53], the phase-based method maintained relatively accurate phase behavior, yet induced magnetization cancellation in regions with inhomogeneous B_0 field due to its relatively

long echo time. This may affect the final calibration result, which is determined by the averaged phase values weighted by signal amplitudes over the ROI. So far, in over 100 human studies, the phase-based method showed fairly high consistency with the amplitude-based method we routinely use for calibration. The correlation coefficient between the results measured by these two methods was above 0.98, and none of the differences between these two methods exceeded 10% of the result from the amplitude-based method. Further evaluation of the accuracy of this method can be done by acquiring 3D B_1 mapping simultaneously with the phase-based calibration method. Similarly, the impact of B_0 inhomogeneity effects on the accuracy of the phase-based method can be measured through simulation based on spatially registered 3D B_0 mapping results acquired simultaneously.

Chapter 4

Acceleration of Combined ^{3}He and ^{1}H Acquisitions using CS Technique

4.1 Introduction

4.1.1 Compressed Sensing Technique

Compressed-sensing (CS) theory reveals that signals or images having a sparse representation in some domain can be reconstructed from randomly undersampled k-space data provided that an appropriate nonlinear reconstruction strategy is used [73]. Figure 4.1 shows a simple example of how the CS technique works: a sparse signal can be sampled below the Nyquist limit if the sampling pattern is appropriately designed to induce sufficiently small incoherent noise. The signal is recovered using an iterative reconstruction that detects signals by thresholding, and removes already detected signals and associated incoherent noise generated due to the random undersampling, allowing detection of additional signals.   This is repeated until the residual is sufficiently small.

The CS technique, which enables acceleration of the acquisition via the undersampling, seeks converged solutions in the sparsifying domain by minimizing the L1 norm [73], as Eq. 4.1 shows, where m is the image data (or k-space data) corresponding to the object, F_s denotes the Fourier Transform, and ψ corresponds to the sparsifying transform chosen for the application. This transform can be total variation, wavelet transform, differences between time frames, etc., or any combination of them.

The boundary condition shown in this equation controls the fidelity of the reconstruction compared to the measured data. An L2 norm is shown here, while in practice in some situations, an L1 norm can be used, depending on signal types and optimization requirements.

$$\textbf{minimize} \quad \|\psi m\|_1$$
$$\textbf{s.t.} \; \|F_s m - y\|_2 < \varepsilon$$

[Eq. 4.1]

Randomness is very important for the CS technique, because sampling below the Nyquist limit causes signals to interfere. If the interference becomes larger than the signal itself and cannot be removed, signal will be lost. The Transform Point Spread Function (TPSF; the conventional point spread function can be viewed as the TPSF when no sparsifying transform is used) is commonly used to investigate the interference generated by the undersampling pattern in the sparsifying domain. The TPSF represents the contribution of a unit-intensity pixel located at position i to a pixel located at position j, and can be calculated using Equation 4.2 [73]. In practical situations, the TPSF of the contribution of a pixel at the origin to the whole image domain is calculated, and the sizes of the sidelobes are measured to assess the performance of an undersampling pattern.

$$TPSF(i; j) = e_j^* \psi F_s^* F_s \psi e_i$$

[Eq. 4.2]

Application of the CS method in hyperpolarized-gas imaging can help reduce the acquisition time by requiring fewer RF pulses, while maintaining or even increasing the basic signal-to-noise ratio (SNR) by permitting higher flip angles, because of the non-equilibrium nature of hyperpolarized-gas magnetization. This can be achieved without the need for a multi-channel RF coil, as required for parallel-imaging techniques. The CS method applied to hyperpolarized-gas imaging has been validated by simulation

results and undersampled acquisitions with an acceleration factor of 2 [74], and extended to an acceleration factor of 3 for 2D imaging using prior knowledge of ^{1}H lung images acquired on the same subject [75], while still maintaining relatively good image quality.
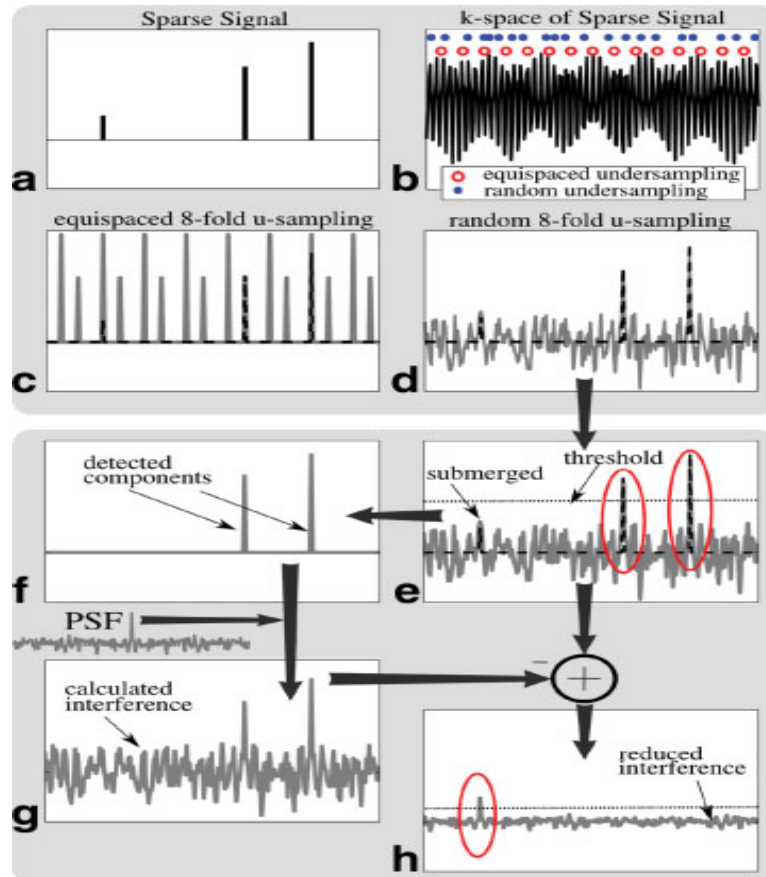
Figure 4.1. Basic example illustrating the compressed-sensing technique. a.) A sparse signal with two strong components and one weak component. b.) *k* space of the signal and two different sampling schemes: equally-spaced samples and randomly-spaced samples c.) Aliasing in the recovered signal after Inverse Fourier Transform for 8-fold undersampling with equally-spaced samples; the signal cannot be recovered. d.) Incoherent noise seen in the signals after Inverse Fourier Transform for 8-fold randomly undersampled data. e-f.) The two strong components are detected using a threshold while the weak component is buried in

the noise. g.) Signal corresponding to the two strong components and the noise (interference) they generate for the random undersampling pattern. h.) After subtracting (g) from (e), the weaker signal is also recovered after lowering the threshold. This figure is reproduced from [73] with permission.**

4.1.2 Potential of Accelerating the Combined ^{3}He and ^{1}H Acquisitions

Using a Cartesian trajectory, 3D imaging applications are inherently favored for the CS technique, because, for 3D, two phase-encoding directions allow more freedom to generate a random undersampling pattern which yields less incoherent noise.   Figure 4.2 shows an example of 2D and 3D undersampling patterns (adapted from [74] with permission).   Simulation results [74] show that undersampling in 3D acquisitions has great potential for acceleration. So, it is highly desirable and applicable to apply the CS technique to combined ^{3}He and ^{1}H acquisitions to address the long breath-hold durations imposed by current methods; this is the thrust of Specific Aim 2. By evaluating the undersampling pattern using fully-sampled datasets acquired in healthy and diseased subjects, we will be able to generate an optimal undersampling pattern for lung imaging (for both hyperpolarized gas and proton images), and shorten the total acquisition time to less than 10s, which is easily tolerable for most subjects. The undersampled, CS-reconstructed image sets are compared with their fully-sampled counterparts to evaluate the reconstruction fidelity.

The efficiency and potential of compressed sensing relies highly on the sparsity of the images of interest in the sparsifying domain, which means the images must have a sparse representation (relatively few significant non-zero values) in a known transform domain.

Although some MR acquisition types yield sparse data in the image domain (for example, MR angiograms), most MR images are not especially sparse in the image domain. However, they do typically exhibit transform sparsity because the images have a sparse representation in terms of some transforms such as a wavelet transform [73].
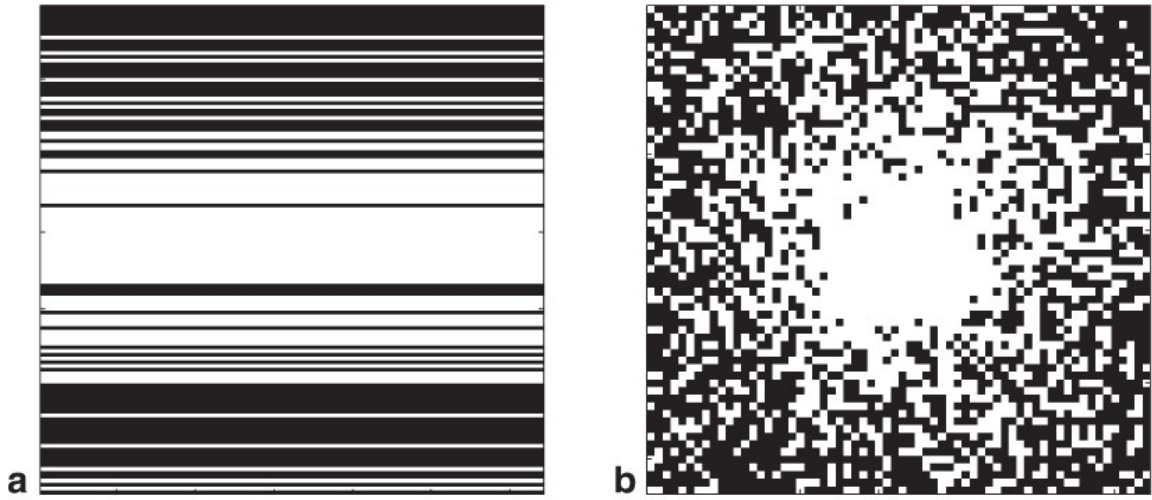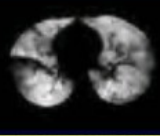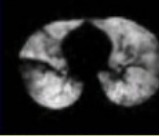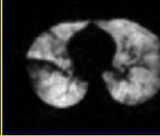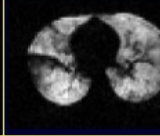
Figure 4.2. Examples showing 2D and 3D undersampling patterns: a.) 2D CS undersampling pattern with acceleration factor of 2. White lines denote sampled _k_-space lines. b.) 3D CS undersampling pattern with acceleration factor of 3, showing the sampled _k_-space lines (white points) in the two phase-encoding directions. Images reproduced from [74] with permission.

The sparsity of ^{3}He ventilation images was evaluated by testing a variety of lifted wavelet transforms on data acquired from healthy subjects and subjects with lung disease (asthma or cystic fibrosis [CF]). The lifted Cohen-Daubechies-Feauveau 9/7 (CDF 9/7) wavelet [95] was chosen because the ^{3}He ventilation images generally demonstrated a high degree of sparsity in this domain. Specifically, our calculations indicate that most ^{3}He images reconstructed with as few as 10% of the principal CDF 9/7 wavelet

coefficients yield a mean absolute percentage error (MAPE, discussed in Section 4.2.4) of less than 10% compared to the original image, as shown in Figure 4.3. This suggests that lung [3]He images are sparse in this wavelet domain, although not that sparse because of the smaller image size compared with high resolution ^{1}H image sets (for our study, image sizes are restricted to ~100 in both phase-encoding directions, with a spatial

Figure 4.3. Sparsity of a representative [3]He ventilation image in the CDF 9/7 domain.

resolution of 3.9 mm), since based on CS theory [73], an N-dimensional vector that is k-sparse can be completely recovered using on the order of k*logN measurements [96]. Thus, without use of a multi-channel RF coil, an acceleration factor of 3 to 4 is suggested as the maximum we should use to achieve satisfactory reconstruction fidelity.

4.2 Methods

4.2.1 Undersampling Pattern

Compressed sensing relies on incoherent interference of aliasing in the sparse transform domain. The transform point spread function (TPSF) of the undersampling pattern (as described above) and the signal behavior of specific datasets together determine the characteristics of aliasing interference. To determine an optimal sampling-density scheme for our application, we chose previously acquired [3]He image

data to perform retrospective simulation tests. The ^{3}He image data used for these simulation tests were acquired in a healthy subject (female, age 25) using a rigid chest ^{3}He RF coil (Rapid Biomedical, Rimpar Germany) and TR/TE 1.78/0.75 ms, in a subject with CF (male, age 23) using a flexible chest ^{3}He RF coil (Clinical MR Solutions, Brookfield, WI) and TR/TE 1.78/0.75 ms, and in a subject with asthma (female, age 21) using the rigid chest ^{3}He RF coil and TR/TE 1.86/0.79 ms.   A 3D balanced steady-state free-precession (TrueFISP) pulse sequence was used with common parameters including a matrix of 128 x 80 x 60, spatial resolution of 3.9 x 3.9 x 3.9 mm^3, receiver bandwidth per pixel of 1085 Hz, and flip angle of 9°.   All measurements were performed on a 1.5-T commercial MR scanner (Magnetom Avanto, Siemens Medical Solutions, Malvern, PA).

Simulation followed three steps: 1) generate 9 Poisson disc sampling-matrix "pools" with uniform sampling density from 10% to 90%, with an increment of 10%; 2) generate two sampling-density schemes (polynomial weighting [73] and exponential weighting [97]) with different density distributions, and for each power density function draw sampling points from the same matrix position out of the sampling-matrix pool with the nearest density to obtain the undersampling pattern (i.e., variable-density Poisson disc sampling); and 3) undersample representative datasets by applying these sampling matrices and then compare the corresponding reconstructed images with fully-sampled images.   Figure 4.4 shows how the reconstruction performance for polynomial weighting varied with the change of weighting factors for datasets from a healthy subject and from subjects with asthma or CF.   For the polynomial weighting scheme, the minimum mean absolute percentage error and maximum structural similarity index both occurred for a power of 2.   The optimal sampling scheme for exponential weighting [97]

(results not shown in Figure 4.4) showed a density distribution similar to the polynomial weighting scheme at a power of 2, and so the polynomial weighting scheme at a power of 2 was selected for our work. Figure 4.5 shows an example of the power density function and sampling scheme we selected for the ^{3}He data. Based on an analogous analysis for proton images, exponential weighting with a factor of 1.5 was selected because this yielded better reconstruction performance for all datasets tested.
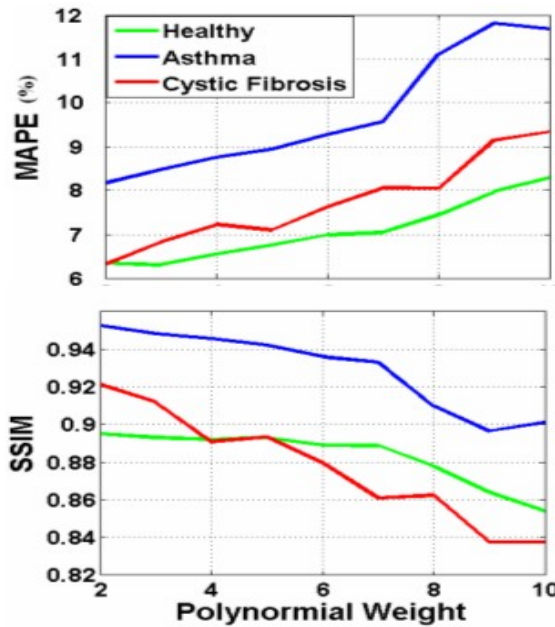
Figure 4.4.   Mean absolute percentage error (MAPE) and structural similarity index (SSIM) as a function of the power for the polynomial weighting density function for ^{3}He lung image sets from healthy and diseased subjects (simulation).   See Section 4.2.4 for a description of the MAPE and SSIM metrics.

4.2.2 Experimental Setup and Imaging Protocols

For experiments in this project, ^{3}He gas was polarized by collisional spin exchange with an optically-pumped rubidium vapor using a custom-built system. All experiments were performed under a Physician's IND for imaging with hyperpolarized ^{3}He using a protocol approved by our institutional review board.   Informed consent was obtained in all cases.

Helium and proton studies were performed using a 1.5-T whole-body scanner (Magnetom Avanto, Siemens Medical Solutions) equipped with the multi-nuclear option and a chest ^{3}He RF coil (Rapid Biomedical). This RF coil included circuits for signal blocking at the proton resonance frequency to permit proton MRI to be performed with
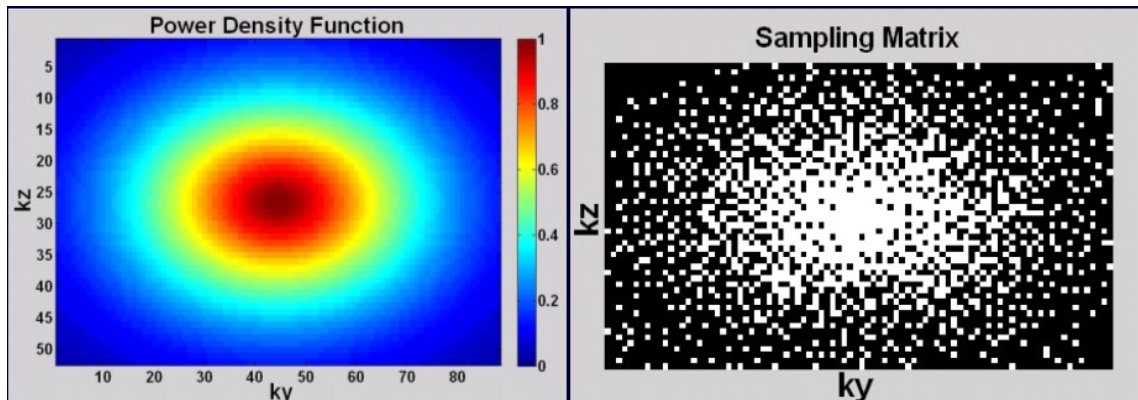
Figure 4.5. Example of the power density function and undersampling pattern used for ^{3}He acquisitions.

the ^{3}He coil in place.   The subject was positioned supine on the scanner table with the ^{3}He RF coil around their chest.   Breath-hold scout images were obtained using conventional proton MRI for positioning of the ^{3}He acquisitions.   Next, the subject inhaled a gas mixture containing approximately 50 ml of hyperpolarized ^{3}He and a breath-hold acquisition was performed for calibration of the scanner center frequency and transmitter voltage.   For the combined ^{3}He/^{1}H acquisitions, the subject inhaled ^{3}He gas and held their breath for approximately 10-20s. The ^{3}He acquisition was performed first, follow by a short pause (less than 0.5 s, due to switching the coil), and the ^{1}H acquisition was then executed.

In total, 9 healthy subjects and 3 diseased subjects participated in 13 studies for this compressed-sensing study (Table 4.1), which can be divided into 4 groups based on specific purposes and imaging protocols:

1.) ^{3}He imaging only: Two healthy subjects were scanned with ^{3}He acquisitions only to test the undersampling pattern and compressed-sensing reconstruction algorithms. Sequence protocols were the same as those for the ^{3}He sequence in group 2.

2.) Comparison in different breath-holds: Three healthy subjects and one subject with CF were scanned with combined ^{3}He/^{1}H acquisitions. One healthy subject was scanned with full sampling (x1) and undersampling with an acceleration factor (R) of 2 (x2). The other two healthy subjects and the CF subject were scanned with x1 and x3 sampling; fully-sampled and undersampled data were acquired in different breath-holds. A 3D balanced steady-state free-precession (TrueFISP) pulse sequence [71] was used for both ^{3}He and ^{1}H. Parameter settings included: ^{3}He: TR/TE 1.86/0.79 ms, matrix 128x88x52; and ^{1}H: TR/TE 1.79/0.74 ms, matrix 128x110x64. Common parameters for both scans included: flip angle 9°, spatial resolution 3.9x3.9x3.9 mm^3, bandwidth/pixel 1085 Hz. Total acquisition time was reduced to 4.3 s for ^{3}He and 6.6 s for ^{1}H at a random-undersampling acceleration factor of 2, and to 2.8 s for ^{3}He and 4.1 s for ^{1}H at an acceleration factor of 3, compared with 6.7 s for ^{3}He and 9.7 s for ^{1}H for the fully-sampled scans. (To keep the total acquisition time below 20 s, the fully-sampled scans used elliptical sampling of the phase-encoding steps [i.e.,

the "corners" of k space were not sampled]. The accelerated scans did not use elliptical sampling.)

3.) Comparison in one breath-hold: Fully sampled and undersampled acquisitions were incorporated into one breath-hold to directly compare the image sets without encountering a position change between scans due to different breath-hold positions. Because the duration of combined ^{3}He/^{1}H acquisitions is too long for the subject to hold their breath for fully-sampled and undersampled acquisitions for both nuclei, ^{1}H and ^{3}He acquisitions were tested separately with x1 and x3 acquisitions for a given nucleus incorporated into one breath-hold. One healthy subject was tested with a ^{1}H acquisition using x1 and x3 acceleration factors, and 3 healthy subjects were tested with a ^{3}He acquisition using x1 and x3 acceleration factors. Protocols used were the same as those for group 2.

4.) Comparison of ventilation defects in different breath-holds for diseased subjects: We used advanced registration and segmentation methods to quantitatively compare the ventilation defects found in fully-sampled and CS-reconstructed undersampled images acquired from diseased subjects. Two asthmatics were scanned with the combined acquisition using x1 and x3 acceleration factors obtained in different breath-holds. For these studies, a GRE pulse sequence was used for the ^{1}H acquisitions, and three protocols were implemented to better accommodate subjects with different lung sizes. Parameter settings included: ^{3}He: TrueFISP pulse sequence, flip angle 9°, TR/TE 1.86/0.79 ms, matrix 128x72x44 (small), 128x80x52 (medium) or

128x88x60 (large), bandwidth/pixel 1085 Hz; and ^{1}H: GRE pulse sequence, flip angle 10°, TR/TE 1.80/0.78 ms, matrix 128x100x56 (small), 128x110x64 (medium) or 128x120x72 (large). Spatial resolution was 3.9x3.9x3.9 mm^3 for all acquisitions.   Total acquisition time was 5.4 s for small subjects, 7.0 s for medium subjects and 8.5 s for large subjects at an acceleration factor of 3, compared with 9.8 s for small subjects, 12.8 s for medium subjects and 15.7 s for large subjects with full sampling after applying elliptical scanning and the partial Fourier technique.

Table 4.1. Subject and acquisition information for compressed-sensing studies.

Group	Sub.	Number	Acquisition	Breath-hold	^{1}H Seq.	Protocol
1	H	2	^{3}He, x1/x2/x3	Different	TrueFISP	Fixed size
2	H	1	Combined x1/x2	Different	TrueFISP	Fixed size
	H	2	Combined x1/x3	Different	TrueFISP	Fixed size
	CF	1	Combined x1/x3	Different	TrueFISP	Fixed size
3	H	1	^{1}H, x1/x3	Same	TrueFISP	Fixed size
	H	3	^{3}He, x1/x3	Same	N/A	Fixed size
4	A	2	Combined x1/x3	Different	GRE	3 options

H = healthy, A = asthma.

4.2.3 Image Reconstruction

Undersampled images were reconstructed using the SparseMRI Toolbox by M. Lustig [**73**]. Reconstructions were achieved by seeking minimal solutions of the L1 norm of the wavelet transform and the total variance (TV) norm, while restricted by the data consistency terms, as Eq. 4.3 shows. m denotes the reconstructed complex images, F_s

denotes the undersampling Fourier transform, y represents the measured *k-space* data, Ψ is the CDF 9/7 wavelet transform we chose for HPG imaging, TV is the total variance norm, and λ_1 and λ_2 control the weighting of the different sparsifying transforms and are also related to the expected noise levels of acquired data. λ_1 and λ_2 are determined by the specific data types. In our work, optimized values λ_1 of 0.001 and λ_2 of 0.003 were used based on simulation results from acquired data.

$$\left\| F_s m - y \right\|_2 + \lambda_1 \left\| \Psi m \right\|_1 + \lambda_2 TV(m) \qquad \textbf{[Eq.4.3]}$$

Reconstruction of the CS acquisitions was implemented in MATLAB (MathWorks, Natick, MA). The calculation times for reconstruction were approximately 20 minutes for ^{3}He datasets and 30 minutes for ^{1}H datasets using a desktop PC (Optiplex GX745, Intel Core 2 CPU 6400, 2.13 GHz, 2 GB RAM, Dell Inc, Round Rock, TX).

4.2.4 Evaluation of CS Reconstruction Fidelity

Two metrics were used for direct comparison of fully-sampled and CS reconstructed undersampled images, and apply for all simulation tests (applying undersampled pattern to fully-sampled datasets and comparing the reconstructed images with fully-sampled images), and for studies from group 2 and group 3:

1). Mean absolute percentage error (MAPE): This is obtained by taking the ratio of the amplitude of difference images to the amplitude of the fully-sampled images, and then averaging the resulting values over a region of interest (typically, the ventilated lung region as determined by applying a noise threshold to the fully-sampled images).

2). Structural similarity index metrics (SSIM) [99]: SSIM ranges from -1 to 1, with the maximal value of 1 obtained only for the case of two identical sets of data. Similarity

index maps were calculated from the fully-sampled and compressed-sensing images, and a mean index was calculated by averaging the indices from the ventilated region of the lung.

Direct quantitative comparison between fully-sampled and undersampled acquisitions for ^{3}He ventilation images, even acquired in the same breath-hold, may still be affected by factors, such as diaphragm movement and the non-equilibrium nature of hyperpolarized magnetization, which are not related to the compressed-sensing technique [100]. Considering that the major application of ^{3}He ventilation imaging is to distinguish normally-ventilated areas from those with poor ventilation (ventilation "defects"), an automated segmentation method [101] was proposed recently for quantifying ventilation defects in ^{3}He images using ^{3}He/^{1}H multivariate templates to register and segment the ^{3}He images [102]. Using this approach, in the studies of group 4, we sought to compare and quantify the ventilation defects found in fully-sampled and CS-reconstructed undersampled ^{3}He image sets acquired in the same subjects but during different breath-holds.

Registration and segmentation followed four steps: 1) Image sets were N4 bias corrected to eliminate signal intensity variation due to B_1 inhomogeneity effects. 2) Whole-lung masks were generated for the fully-sampled and CS ^{1}H image sets based on registration with an ^{1}H image-labeled template generated from eight subjects' ^{1}H chest images. 3) The CS ^{1}H image was registered to the fully-sampled ^{1}H image to provide the mapping of the undersampled ^{3}He ventilation image to its counterpart acquired in the fully-sampled acquisition. 4) Lung regions were segmented into 4 classifications based on signal intensities, with two of them (Label 1, 2, combined as Class 1) representing the

poorly-ventilated regions and the other two (Label 3, 4, combined as Class 2) representing the normally-ventilated regions. Label overlays between the two segmented and labeled maps were measured using the Dice metric after combining the poorly-ventilated labels and the normally-ventilated labels. Registration and segmentation scripts are available in the Advanced Normalization Tools (ANTs) package [103].

4.3 Results

4.3.1 Undersampled ^{3}He Acquisitions

Contiguous coronal sections of the lung of a healthy subject from study group 1 are shown in Figure 4.6 for fully-sampled and accelerated (R = 2; R = 3) 3D ^{3}He acquisitions. No major differences between the fully-sampled and accelerated images sets were observed. For example, the small pulmonary nodule (an incidental finding in this healthy subject) was clearly seen in all three image sets (arrows). The acquisition time for the undersampled datasets was reduced to 4.3 s (R = 2) and 2.8 s (R = 3) from 6.7 s for the fully-sampled acquisition.

A simulation-based evaluation (using the fully-sampled dataset) of reconstruction fidelity for ^{3}He data from this subject for acceleration factors of 2 and 3 was investigated (Figure 4.7). The MAPE and SSIM values over the lung region calculated by retrospectively undersampling the fully-sampled data were 5.1% and 0.94, respectively, for R = 2, and 6.6% and 0.91, respectively, for R = 3. Although quite minor in both cases, differences for R = 3 are clearly larger than those for R = 2; these differences indicate that some fine detail was not preserved in the CS reconstruction. The increase seen in the difference images is consistent with lower similarity indices observed in some

regions of the lung for the R = 3 case compared to the R = 2 case. Nonetheless, we felt that the performance of the R = 3 case was sufficient to warrant further evaluation of three-fold acceleration.
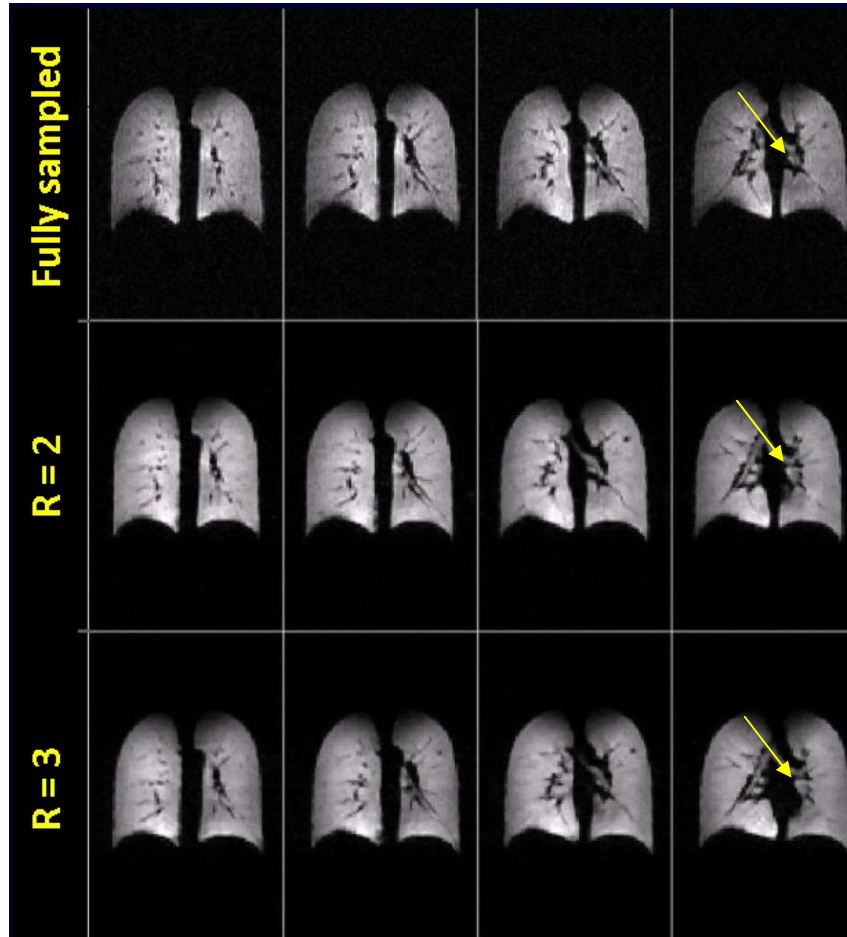
Figure 4.6. ^{3}**He ventilation images acquired with full sampling and undersampling with factors of 2 (R=2) and 3 (R=3) from a healthy subject in study group 1.**

4.3.2 Comparison of Fully-sampled and Undersampled Image Sets Acquired in Different Breath-holds

All subjects in study group 2 underwent combined ^{3}He and ^{1}H scans with full sampling and under-sampling acquired in different breath-holds. Figure 4.8 (reproduced

from [98]) shows images reconstructed in three planes from one of the healthy subjects. Although there is slightly elevated incoherent noise behavior in the CS-reconstructed images, especially apparent in the transverse view, the CS images generally match the fully-sampled images well. Since the fully-sampled images and CS images were acquired in different breath-holds, there was a position shift between the two acquisitions, which can be identified by comparing four contiguous slices selected from the two datasets, as Figure 4.8b shows.
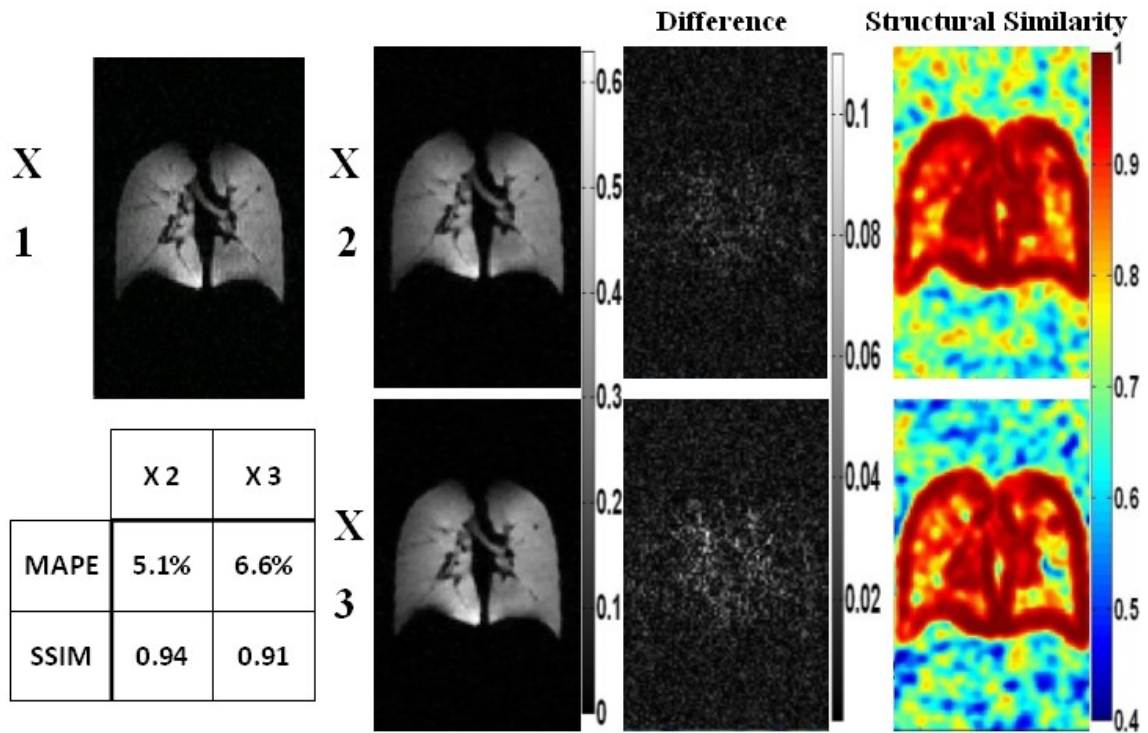
Figure 4.7. Evaluation of reconstruction fidelity by simulation based on fully-sampled ^{3}He datasets acquired in one of the healthy subjects in study group 1. Difference images and structural similarity maps for fully-sampled versus x2 acceleration, and fully-sampled versus x3 acceleration, are shown on the right.
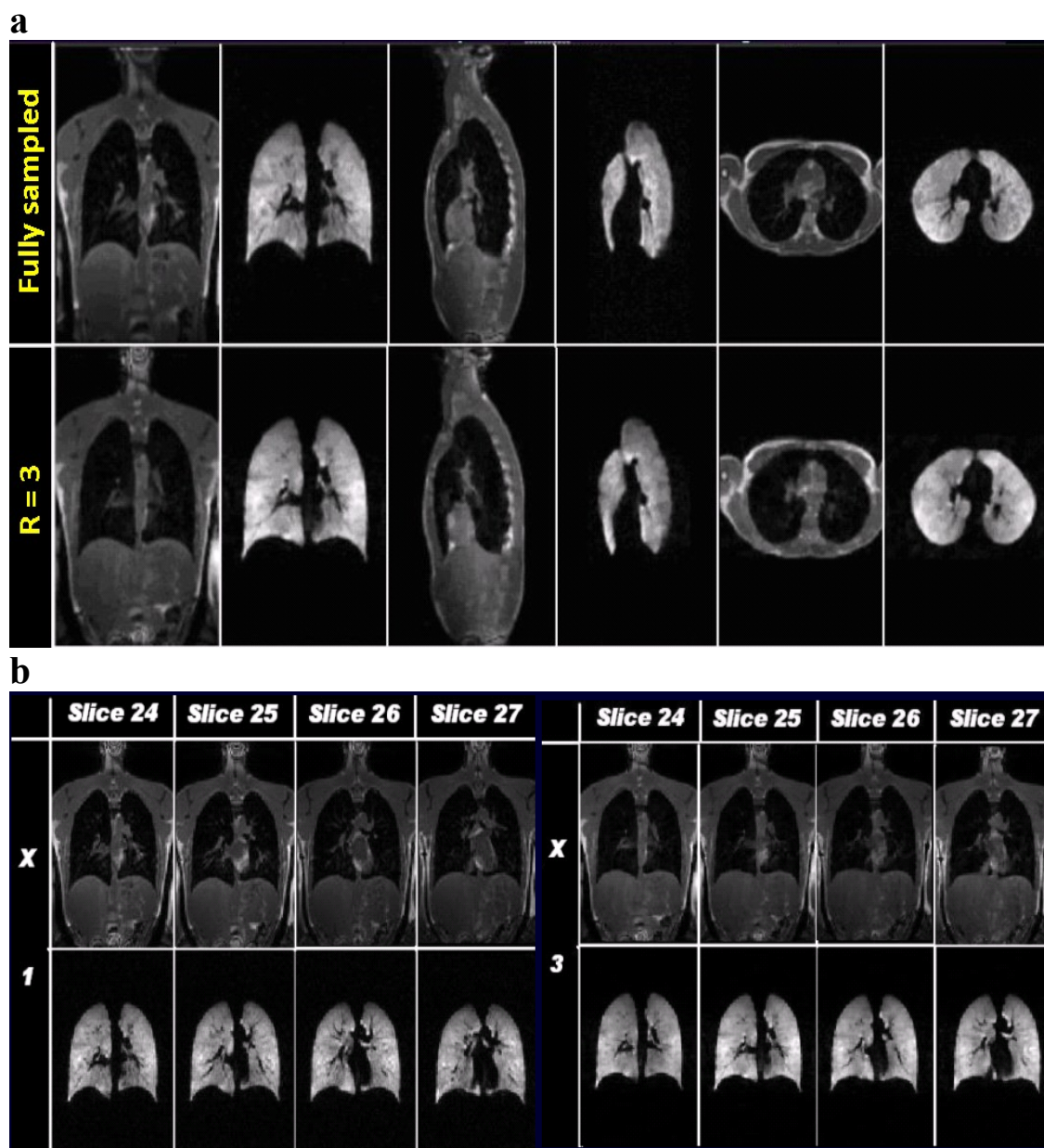
Figure 4.8. a.) Fully-sampled images versus compressed-sensing images with R=3, acquired from one of the healthy subjects in study group 2, shown in 3 orthogonal planes. b.) Contiguous coronal images.

a

b
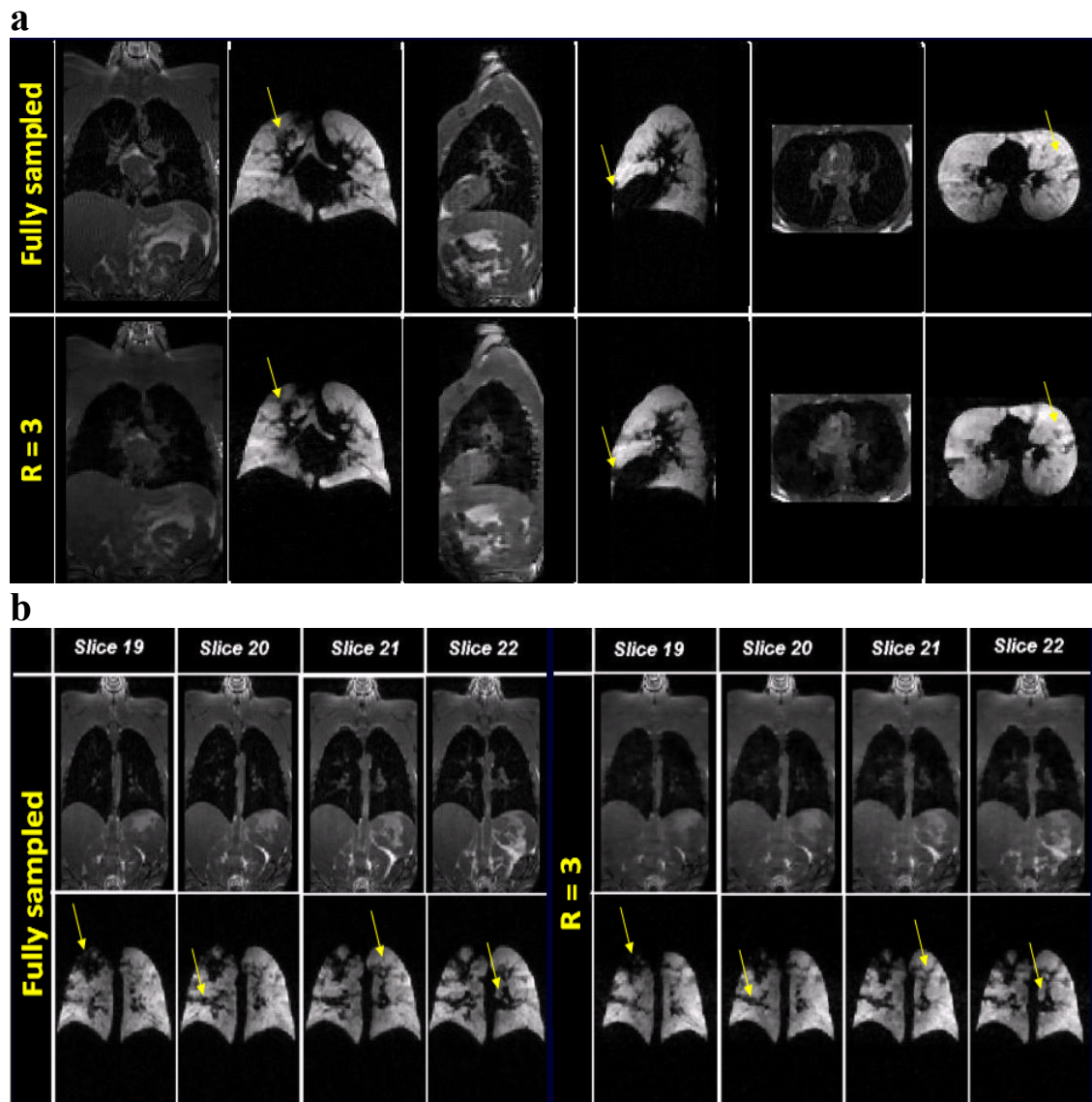
Figure 4.9. a.) Fully-sampled images versus compressed-sensing images with R=3, acquired from the cystic fibrosis subject in study group 2, shown in 3 orthogonal planes. b.) Contiguous coronal images. Yellow arrows indicate some of the ventilation defects.

Images reconstructed in three planes from a CF subject in group 2 are displayed in Figure 4.9, with corresponding contiguous coronal images shown in the lower row.

Similar ventilation defects can be identified in both the fully-sampled acquisition and the undersampled acquisition as indicated by yellow arrows in the ^{3}He images. But, because of patient movement and ventilation variation between breath-holds (which, in our experience, is more prominent in diseased subjects), the undersampled and fully-sampled image sets are clearly not identical, and thus direct quantitative comparison on an image-by-image basis is challenging. We describe results for quantitative comparison of ventilation defects between fully-sampled and undersampled acquisitions in Section 4.3.4.

Simulations analogous to those discussed in Section 4.3.1 were performed based on the fully-sampled datasets acquired for the three healthy subjects in study group 2. All MAPE values were below 10% and all SSIM values were above 0.9, as shown in Table 4.2.

Table 4.2. Simulation of reconstruction fidelity (x1 versus x3 acceleration) on fully-sampled ^{3}He/^{1}H datasets acquired in the three healthy subjects in class 2.

^{3}He images	Healthy 1	Healthy 2	Healthy 3
MAPE	6%	7%	7%
SSIM	0.93	0.92	0.94
^{1}H images			
MAPE	9%	8%	8%
SSIM	0.93	0.93	0.94

4.3.3 Comparison of Fully-sampled and Undersampled Image Sets Acquired in the Same Breath-hold

To provide a more direct verification of reconstruction fidelity, beyond the indirect evaluation discussed above, we acquired fully-sampled and undersampled acquisitions in the same breath-hold for subjects in group 3. ^{3}He and ^{1}H acquisitions were performed in

separate scans because combining them would require too long of a breath-hold time (24-30 s). One healthy subject was scanned using the ^{1}H pulse sequence with full sampling and undersampling (R=3) in a single breath hold; the undersampled data were acquired first. Similarly, three healthy subjects were scanned using the ^{3}He pulse sequence with full sampling and undersampling (R=3) in a single breath hold. For the first two subjects, the undersampled data were acquired first, the same as for ^{1}H, while for the third subject, an additional fully-sampled data set was acquired at the end (acquisition order: fully sampled, undersampled [R=3], fully sampled; flip angle 7.9° for optimal SNR).

Results from the ^{1}H comparison are presented in Figure 4.10 (reproduced from [100]), with the upper row showing representative images for full sampling and the middle row showing corresponding images reconstructed from undersampled data. In general, a high level of similarity was found between the two image sets, as indicated by a MAPE of 9.6% and mean SSIM index of 0.90 over all signal-containing regions in the 3D coronal slices. These values are very similar to those calculated by applying the same undersampling pattern to fully-sampled data and then comparing the resulting CS-reconstructed images to the original fully-sampled images (Table 4.2 and bottom row of Figure 4.7), even considering the difference brought by heart movement during the acquisitions, which is fairly prominent in the similarity index maps in Figure 4.10.

In contrast, the similarity values for the ^{3}He acquisitions were not as good as those for the ^{1}H acquisitions: the MAPE and SSIM values calculated by comparing the fully-sampled (acquired first for the third subject) and undersampled image sets were 17% and 0.72, and 16% and 0.74, respectively, for the first two subjects (flip angle 9°), and 13%

and 0.77, respectively, for the third subject (flip angle 7.9°).   The relatively worse indices

obtained for ^{3}He appear to arise from at least 2 factors unrelated to the actual performance

of the undersampled acquisition with CS reconstruction: 1) diaphragm movement between

acquisitions, which can be clearly seen in the difference images in the 3rd row of Figure

4.11 (scaled to the maximum of each image), where a relatively large signal difference is

present at the lung-diaphragm interface; and 2) the non-equilibrium nature of
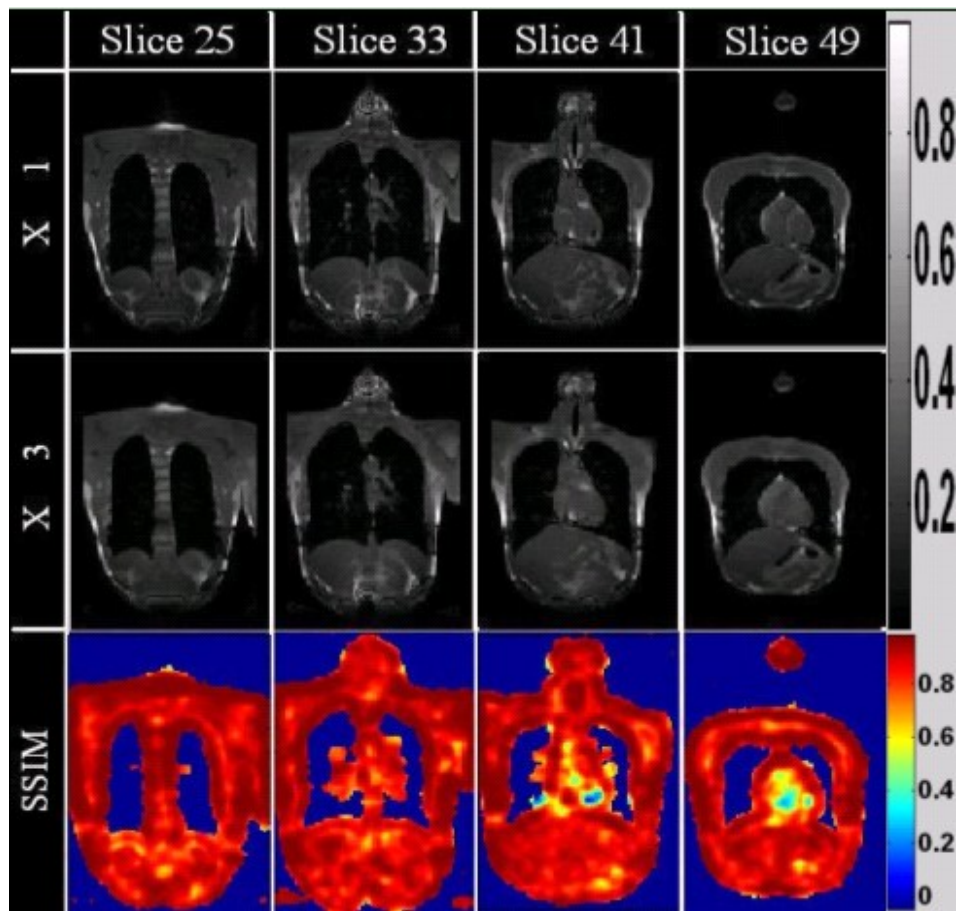
Figure 4.10. Comparison of representative images from fully-sampled (top row) and x3 undersampled ^{1}H acquisitions obtained in one breath-hold.

hyperpolarized-gas magnetization and B_1 inhomogeneity of the RF coil. Since

undersampled and fully-sampled datasets are acquired sequentially, the signal intensity

decreases roughly 15-20% for the second ^{3}He acquisition based on the flip angle used, while noise remains constant from acquisition to acquisition. Also, B_1 inhomogeneity gradually modifies the relative signal-intensity distribution within ventilated regions of the lung. These factors may explain the relatively low SSIM indices appearing in most of the uniformly-ventilated regions of the lung (4th row of Figure 4.11), while in regions containing vessels or edges, the similarity indices were much higher.

CS-reconstruction of data from the fully-sampled image set acquired in one healthy subject in group 3 (simulation performed for one central coronal slice) offers further insight on these issues, as shown in Table 4.3 and Figure 4.12. After applying the undersampling pattern with R=3 (R3a* in Figure 4.12), the CS-reconstructed image yielded a MAPE of 8.4% compared with the fully-sampled image, while the SSIM index was 0.88. After adjusting the signal intensity at each pixel of the reconstructed undersampled image (because of the signal decay caused by the train of RF pulses) based on a B_1 map acquired simultaneously with the image data (R3b* in Figure 4.12), the MAPE increased somewhat to 8.5%, while the SSIM index was essentially unchanged. Then, adding noise at a level consistent with the consumption of magnetization during the actual acquisition (R3c* in Figure 4.12), the MAPE increased to 11%, while the SSIM index decreased to 0.81; these
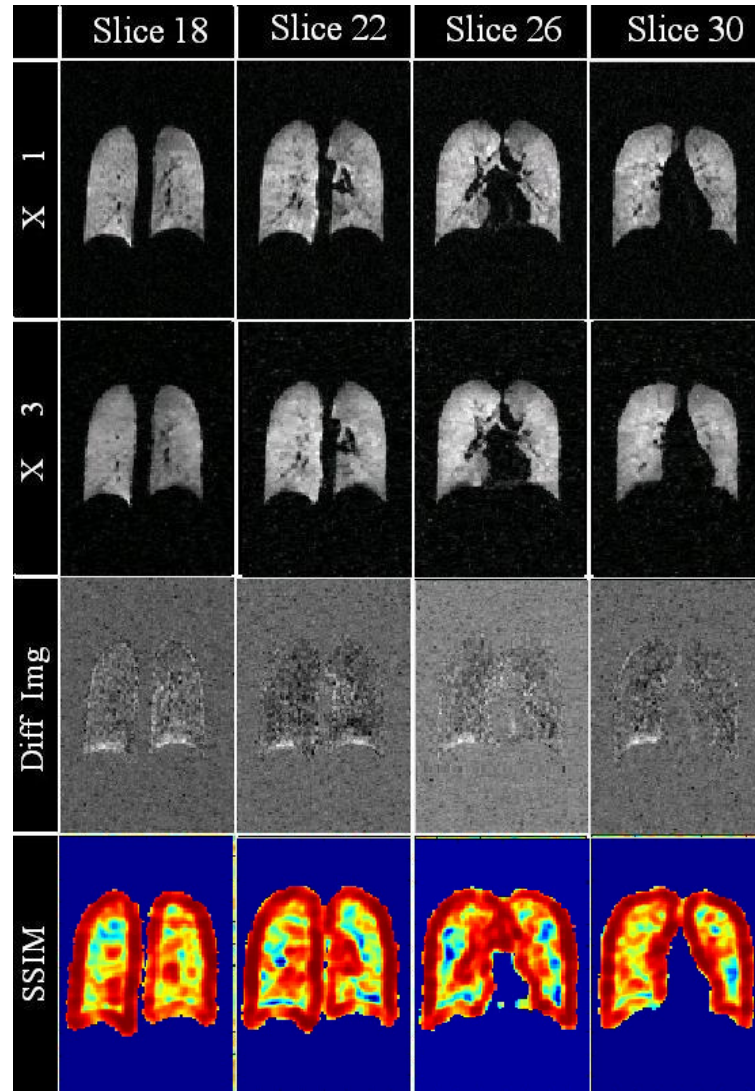
Figure 4.11. Comparison of representative images from fully-sampled (top row) and x3 undersampled (second row) ^{3}He acquisitions obtained in one breath-hold. Diaphragm movement was easily detected from the difference images (third row) even though the two image sets were acquired in the same breath-hold.

values are close to the best indices from the real comparison. This suggests that both B_1 inhomogeneity and SNR loss (due to consumption of the hyperpolarized magnetization) affect the comparison, with SNR being the larger factor. The effect of these factors is also supported by comparison of the two fully-sampled data sets acquired in this subject, which

yielded a MAPE of 23% and a SSIM value of 0.68; both of these values are worse than those for the fully-sampled versus undersampled [3]He data.

Table 4.3. Simulation of reconstruction fidelity (central slice from one healthy subject) compared with actual acquisition.

Fully-sampled (R1) vs.	Undersampled from R1 (R3a*)	Undersampled with intensity adjustment (R3b*)	Undersampled with intensity and noise adjustment (R3c*)	Actual undersampled acquisition (R3)
MAPE	8.4%	8.5%	11%	16%
SSIM	0.88	0.88	0.81	0.74

*indicates simulation based on fully-sampled datasets for comparison with actual undersampled acquisition.
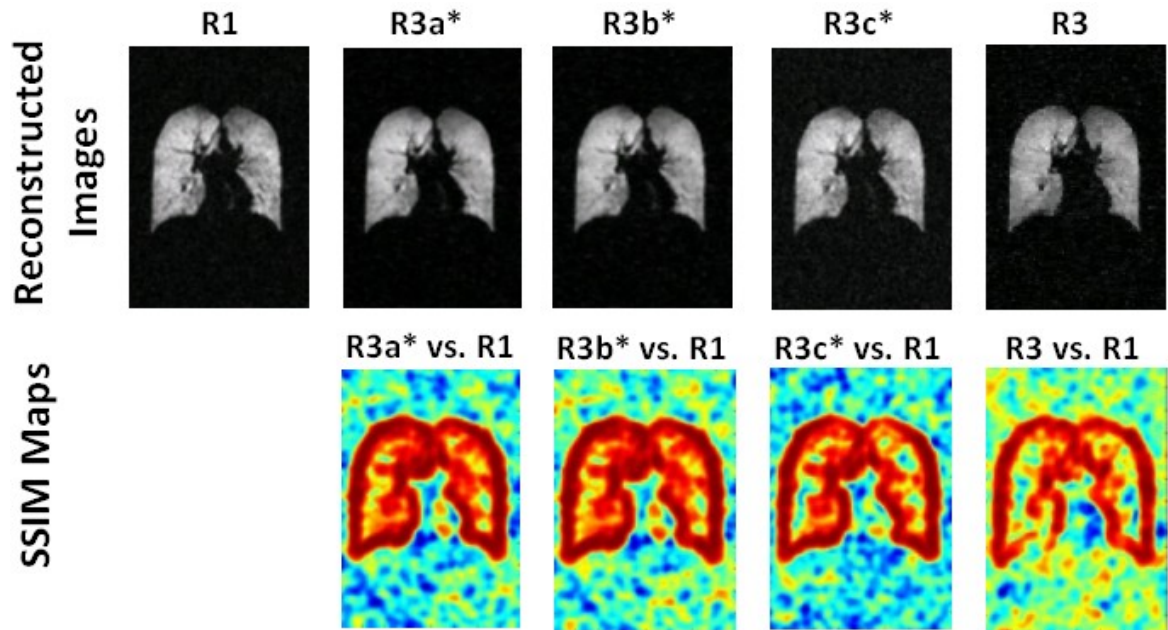
Figure 4.12. Upper row shows reconstructed images from fully-sampled data obtained by undersampling R1 by a factor of 3 (R3a*); by, in addition, adjusting the signal intensity for the signal decay predicted for the excitation RF pulses based on B_1 mapping results (R3b*); and by, in addition, increasing the noise level to be consistent with signal decay (R3c*). R3 is the acquired undersampled image. Lower row shows the similarity index maps calculated between the various undersampled images and the fully-sampled image.

4.3.4 Comparison of the Ventilation Defects using [1]H-Image-masked Segmentation

To date, we have imaged two asthmatics (subjects S1 and S2) in study group 4 and compared the fully-sampled and undersampled image sets acquired in different breath-holds using the [1]H-masked segmentation method described in Section 4.2.4. Means of the Dice metric of the overlaid labels are reported in Table 4.4, showing good agreement between the two segmentations. The mean Dice values calculated from Class 2, which corresponds to the normally-ventilated areas, are high --

Table 4.4 Label overlap between the fully-sampled and undersampled (R=3) acquisitions.

Subject / Mean Dice	S1	S2
Total	0.85	0.78
Class 1 (label 1,2)	0.80	0.76
Class 2 (label 3,4)	0.95	0.91

both larger than 0.9. The mean Dice values obtained from Class 1, representing poorly-ventilated regions, are lower. Reviewing the underlying ventilation images, this appears to be at least partly due to actual variations of the ventilation defects between breath holds (e.g., yellow arrows in Figures 4.13 and 4.14) rather than artifacts from the CS reconstruction. Figure 4.13 shows an example of 3-planes of both the fully-sampled and CS ventilation images, and the respective labeled segmentation maps from subject S2. The ventilation defects identified by segmentation are very close but not completely identical. Some defects appeared worse in CS images (yellow arrows, Figure 4.13) while others appeared worse in fully-sampled images (yellow arrows, Figure 4.14).
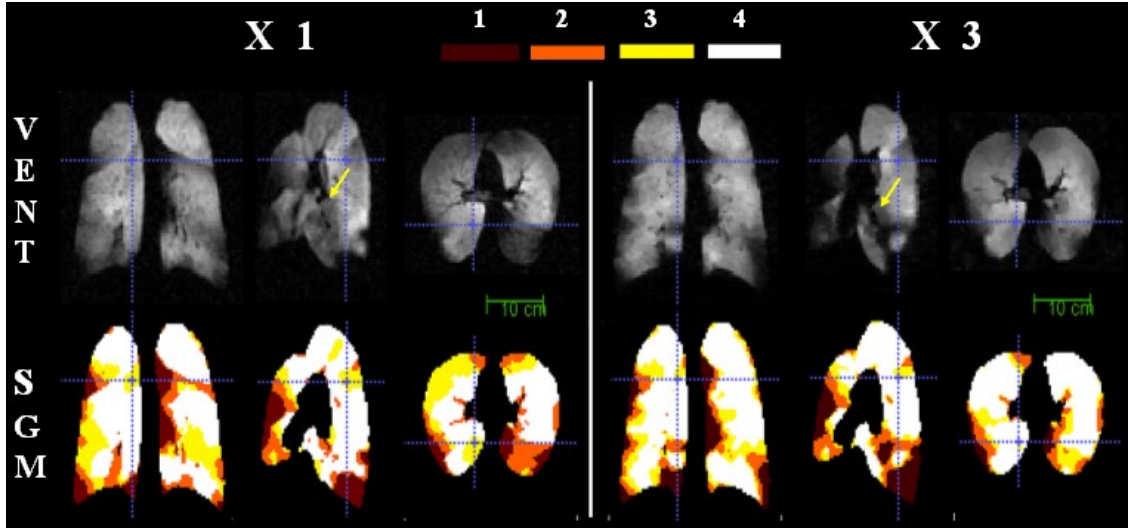
Figure 4.13. Fully-sampled (X1) versus CS (X3; R=3) acquisitions. Coronal, sagittal and axial ^{3}He ventilation images are shown with the corresponding segmentation maps.

4.4 Discussion and Conclusion

By undersampling *k*-space followed by compressed-sensing reconstruction, we were able to acquire spatially registered ^{3}He and ^{1}H images with 3.9-mm isotropic resolution in a breath-hold of less than 7 s. The undersampling pattern used in this work was generated based on simulation results on fully-sampled datasets from previous human scans.

Consistency between the fully-sampled and CS image sets was first verified by visual comparison, as well as indirectly by using undersampling and reconstruction of fully-sampled image sets [98]. Direct, quantitative comparison of fully-sampled and CS images was implemented separately for ^{3}He and ^{1}H acquisitions by incorporating the fully-sampled and undersampled ^{3}He or ^{1}H scans into a single breath-hold. Undersampled, CS-reconstructed ^{1}H images showed relatively high similarity to fully-sampled images. Somewhat lower similarity indices were found for direct comparison of fully-sampled and

CS [3]He image sets, most of which appeared to be caused by factors unrelated to the CS technique, such as diaphragm movement and the non-equilibrium nature of hyperpolarized magnetization [100]. So, we turned to image registration and segmentation methods to directly compare the ventilation defects found in fully-sampled and undersampled image sets acquired in different breath-holds. While relatively high similarities were found between the segmentation results, differences were observed and, at least in part, appear to be due to real variation of ventilation defects between breath holds rather than artifacts related to the CS acquisition. Future work will be focused on diseased subjects; by combining the fully-sampled and undersampled acquisitions into a single breath-hold, we may be able to use the registration and segmentation algorithms demonstrated above to compare the ventilation defects. Without the variation between breath-holds, a relatively fair comparison can be made.

Figure 4.14. Coronal fully-sampled (X1) versus CS (X3; R=3) [3]He ventilation images and corresponding segmentation maps.

Chapter 5

Regional Mapping of Gas Uptake by Red Blood Cells and Tissue using Hyperpolarized ^{129}Xe

5.1 Introduction

5.1.1 Separation of the Dissolved-phase Components

As introduced above in Figure 2.5, the primary peaks in an MR spectrum of ^{129}Xe in the healthy human lung correspond to ^{129}Xe in the lung airspaces (0 ppm, by definition), dissolved in lung parenchyma and blood plasma (~198 ppm), and bound to hemoglobin in RBCs (~218 ppm) [81]. Early research in rats using a Dixon-based technique [82] demonstrated the substantial potential value of discriminating the individual contributions from parenchyma/plasma and RBCs for understanding the physiological consequences of pulmonary disease. Studies in rabbits from our group [91], using the method described in [81], showed a periodic variation in dissolved-phase signal intensity with echo time, consistent with T_2* decay superimposed on a signal variation from the evolution of the phase difference between the parenchyma/plasma and RBC transverse magnetizations, as shown in Figure 5.1 (reproduced from [91]): the dissolved-phase signal dropped rapidly up to a TE of around 4.5 ms, and then leveled off or increased slightly. The modulation period of about 9 ms (111 Hz) agrees well with the 106 Hz frequency separation of the

primary dissolved-phase resonances in rabbit lung at 1.5 T. Also shown in Figure 5.1 is that, by manipulating the sequence parameters (repetition time and flip angle [FA]), the weighting of the image can be substantially changed from highlighting the contribution of dissolved ^{129}Xe near the gas-exchange sites to focusing more on the downstream blood pool. These studies support the possibility of acquiring dissolved-phase images at different echo times and separating the two compartments -- lung parenchyma/plasma (these two components are referred to using the single term "tissue" for the remainder of this dissertation) and RBCs -- using a Dixon-based algorithm. If gas-phase ventilation images can be acquired simultaneously to permit normalization of the dissolved-phase signals, regional quantitative mapping of gas uptake by tissue and RBCs will be feasible and will provide valuable information for assessing lung function and disease. This is the goal of Specific Aim 3.

5.1.2 Water-fat Separation - Hierarchical IDEAL Method

For proton MRI, the frequency separation between water and fat is roughly 3.5 ppm, corresponding to 220 Hz at 1.5 T. While the separation between RBCs and tissue is between 18 and 20 ppm, the corresponding frequency difference is roughly 320Hz to 350Hz at 1.5 T, which is similar to the fat-water difference due to the low gyromagnetic ratio of ^{129}Xe. The T_2^* of ^{129}Xe in RBCs ranges from 1.7 to 2.2 ms, while the T_2^* of ^{129}Xe in tissue ranges from 1.9 to 2.3 ms, for the study protocols we used in this work (lung inflation level, TR and flip angle for exciting dissolve-phase signals; see T_2^* values in Tables 5.2 and 5.3).
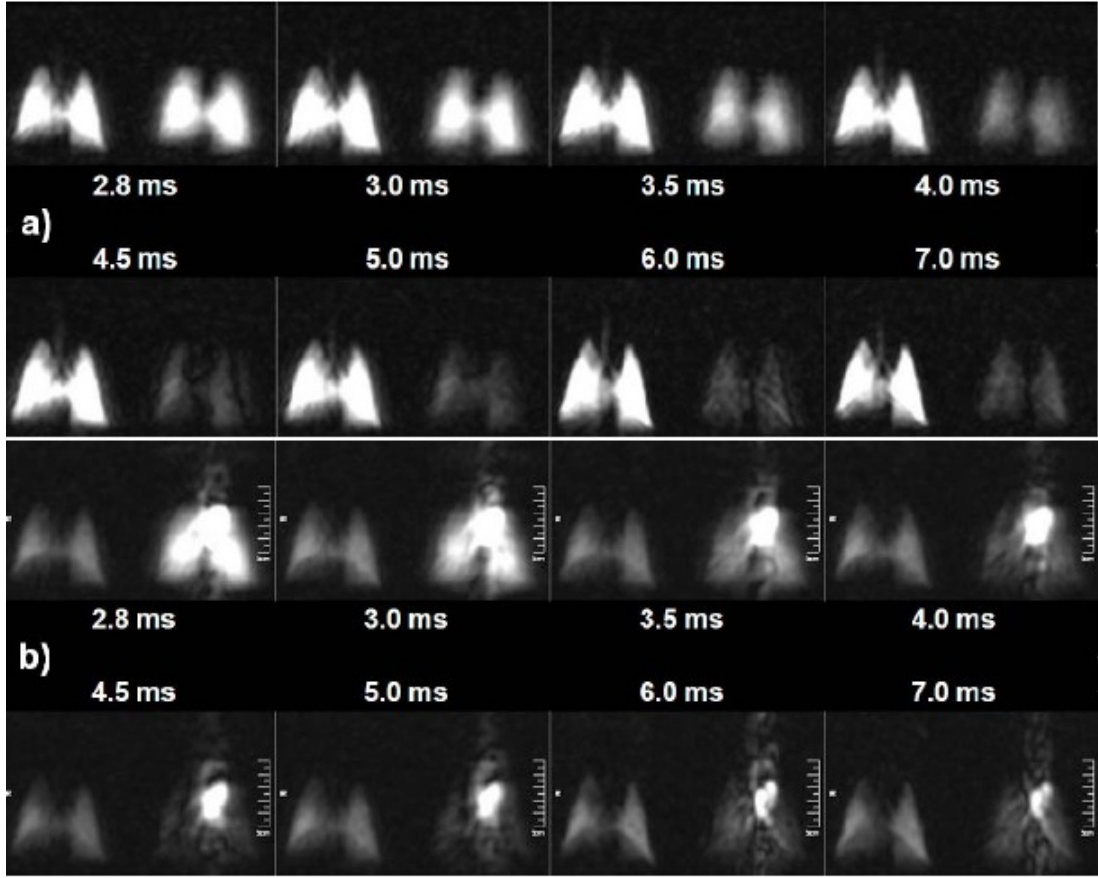
Figure 5.1. **Representative images of simultaneous dissolved-phase (right side of image) and gas-phase (left side of image) acquisitions obtained using the pulse sequence from [81]. Dissolved-phase images acquired at increasing echo times show a periodic variation in signal intensity. a.) Dissolved-phase signals are weighted by ^{129}Xe near the gas-exchange sites (FA 80°, TR 50ms). b.) Dissolved-phase signals are weighted by ^{129}Xe in the downstream blood pool (FA 40°, TR 400ms). Images reproduced from [91].**

As described below, our acquisition can provide a reference B_0 field map from the gas-phase data. However, in practice, the dissolved-phase signal can arise from regions with no gas-phase signal due to exchange and blood transport. Based on this situation, we have focused our efforts so far on the Hierarchical IDEAL method [110, 111, 112] to perform separation of the RBC and tissue components. The Hierarchical IDEAL method

for achieving spectral separation of the components, which was developed for fat-water separation, makes use of the properties of the Fourier Transform of three (or more) points of image data, acquired at equally-spaced echo times [113], to seek optimal field estimation (B_0 and R_2^*), starting from the full field of view and moving to smaller regions. The basic idea of Hierarchical IDEAL is suitable for xenon dissolved-phase imaging under current experimental conditions because the acquired images suffer from relatively low SNR, especially the last echo images. Hierarchical IDEAL methods estimate the field (B_0 and R_2^*) at a gross level, and then use the gross estimation as an initial guess and seek local solutions around this initial guess. This process definitely helps reducing the estimation error due to noise compared with other water-fat separation algorithms [114, 115].

5.2 Methods

5.2.1 Human Subjects

All human experiments were performed under a physician's Investigational New Drug (IND) application for MR imaging with hyperpolarized [129]Xe using a protocol approved by our Institutional Review Board. Written informed consent was obtained from each subject after the nature of the procedure had been fully explained.

The study group for imaging was composed of 5 healthy, nonsmoking subjects, 3 current or past smokers including 1 clinically-healthy subject who had smoked for 15 years and 2 with smoking-related COPD (GOLD Stage III), and 2 subjects with asthma (Table 5.1). Spirometry was performed immediately before and after the imaging session using a hand-held device (Koko; PDS Ferraris, Louisville, CO). Per IND requirements, 12-lead

electrocardiography (HP Pagewriter XLi; Hewlett Packard Co., Palo Alto, CA) was performed in subjects 40 years or older immediately before and after MR imaging. Female subjects received a urine pregnancy test prior to imaging and were excluded from participation if pregnant.   Before the subject was placed in the RF coil for MR imaging, a test dose of xenon (not hyperpolarized) was administered.   The subject was excluded from participation if the test dose was not well tolerated. Throughout the imaging session the subject's heart rate and oxygen saturation level were monitored (3150 MRI Patient Monitor; Invivo Research Inc., Orlando, FL), and the subject was assessed for central nervous system (CNS) side effects of the inhaled xenon.   All studies were supervised by a physician.

Table 5.1.   Subject demographics and baseline spirometry results.

Subject[a]	Age	Sex	FEV_1 %pred[b]	FEV_1/FVC[c]
H1	18	F	119	0.87
H2	21	F	105	0.86
H3	21	F	108	0.90
H4	21	F	91	0.81
H5	54	M	128	0.75
S1	40	M	86	0.69
S2	55	F	39	0.57
S3	58	M	46	0.42
A1	53	M	95	0.56
A2	16	M	100	0.73

[a]H, S and A denote healthy, smoker and asthmatic subjects, respectively.
[b]Percent-predicted value for forced expiratory volume in 1 second (FEV_1).
[c]Ratio of FEV_1 to forced vital capacity (FVC).

5.2.2 Experimental Setup

^{129}Xe polarization

Enriched xenon gas (87% ^{129}Xe) was polarized by collisional spin exchange with an optically-pumped rubidium vapor using a prototype commercial system (XeBox-E10; Xemed, LLC, Durham, NH), based on the flowing approach for hyperpolarized-gas production, that provided gas polarization of approximately 40%. Immediately before MR imaging, the desired volume of hyperpolarized ^{129}Xe gas was dispensed into a Tedlar bag (Jensen Inert Products, Coral Springs, FL) and connected to one arm of a plastic Y connector. A second Tedlar bag containing medical-grade nitrogen was connected to the other arm of the Y connector. Starting from residual lung volume (maximum expiration), the subject inhaled the contents of the two bags and was then instructed to suspend respiration for the duration of data collection. For the dissolved-phase image acquisitions, the total gas volume was approximately one-third of the subject's FVC as determined by spirometry.

MR Measurement

MR acquisitions were performed using a 1.5T commercial whole-body MR scanner (Avanto; Siemens Medical Solutions, Malvern PA) equipped with the multinuclear imaging option. Two ^{129}Xe RF coils were used for the experiments, including a flexible, circularly-polarized, vest-shaped chest RF coil (Clinical MR Solutions, Brookfield, WI) and a rigid, custom-built, linearly-polarized chest RF coil. Both RF coils were blocked at the proton resonance frequency to permit proton MRI to be performed with the ^{129}Xe

RF coil in place.   The subject was positioned supine on the scanner table with the ^{129}Xe RF coil around their chest.   Breath-hold scout images were obtained using conventional proton MRI for positioning of the ^{129}Xe acquisitions.   Next, the subject inhaled a gas mixture containing approximately 200 ml of hyperpolarized ^{129}Xe and a breath-hold acquisition was performed for calibration of the scanner center frequency and transmitter voltage (as discussed in Chapter 3).   For the 3D dissolved-phase image acquisition, the subject inhaled a gas mixture containing approximately 1 L of hyperpolarized ^{129}Xe. In one of the healthy subjects, one smoker and one asthmatic (subjects H3, S2 and A1 in Table 5.1), the 3D dissolved-phase image acquisition was repeated, on the same day for the healthy and smoker subjects, and on different days for the asthmatic.

In a subset of the subjects (two healthy, all smokers, one asthmatic), coronal ^{129}Xe diffusion-weighting images covering the lung volume were also acquired for calculation of apparent diffusion coefficient (ADC) values using the following pulse-sequence parameters: TR/TE 13.8/9.4 ms, flip angle 8.5°, voxel volume 6 x 6 x 25 mm^3, b values 0 and 10 s/cm^2.

Pulmonary Function Tests

In addition to spirometry, a subset of the diseased subjects received full pulmonary function tests to measure their lung volume, diffusion capacity, airway resistance and arterial blood gases as part of their participation in an independent lung-imaging study.

5.2.3 Sequence Design

RF Pulse Design

Since the gas-phase magnetization in the lung following inhalation of hyperpolarized [129]Xe is roughly 100 times larger than the dissolved-phase magnetization, it is critical for the RF pulse used to excite dissolved-phase signals to provide extremely low excitation at the gas-phase frequency to achieve separate excitation of dissolved-phase and gas-phase signals. Using the SLR algorithm for RF pulse design, we designed an optimized RF pulse for this application (reject-band ripple, 0.001%; duration, 1.3 ms). A water phantom (phantom SNR, 140) was used to experimentally verify performance of this RF pulse. Figure 5.2 shows the frequency response of this pulse and the phantom test results using the RF pulse as an excitation pulse with duration of 1.3 ms. We see that, when applied at a selected frequency, the RF pulse yields no visible excitation at 3660 Hz away from this frequency (3660 Hz is the gas-, dissolved-phase frequency difference at 1.5 T). This result indicates that, when applied at the dissolved-phase resonance frequency, the RF pulse should yield negligible excitation of gas-phase [129]Xe in the lung.
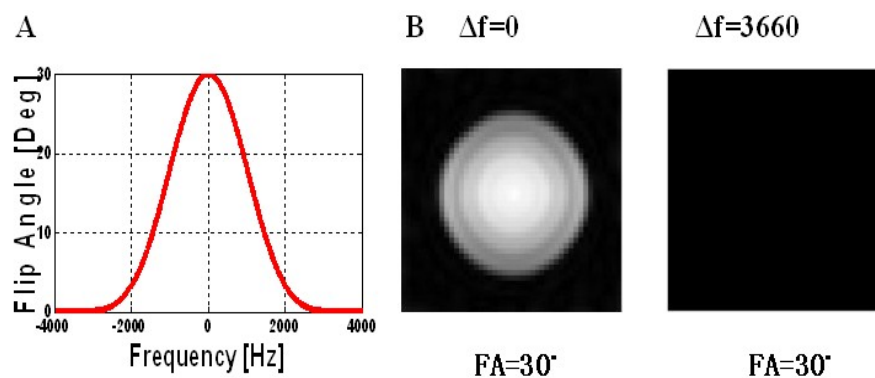
Figure 5.2. A.) RF-pulse frequency response from -4000 to 4000 Hz. B.) Images of a water phantom obtained by applying the RF pulse (flip angle [FA] 30°) at the resonance frequency (Δf = 0 Hz) and 3660 Hz away from the resonance frequency.

Multi-echo 3D Radial Sequence

Successful implementation of a Dixon-based (or an optimized version such as IDEAL) method [104-107] for accelerated spectroscopic imaging of the tissue and RBC fractions requires that there are a small number (for example, two) of distinct resonances, fairly close in frequency, and that the phase differences among the corresponding signals evolve linearly with time. As discussed in Section 5.1.1, our preliminary results from rabbits [91], as well as results in rats from Driehuys et al [82], indicate that a Dixon-based method provides the data necessary to separately depict the tissue and RBC components, and thus we chose this approach for our current work. Specifically, we implemented a pulse sequence based on radial k-space sampling that, to permit separation of the two dissolved-phase frequency components using an IDEAL-type method [106,107], collects three echoes for dissolved-phase [129]Xe following each excitation RF pulse applied at a frequency midway between those for the tissue and RBC resonances (+3660 Hz from the gas phase at 1.5T), and, to permit calculation of a B_0 map for reference, collects two echoes for gas-phase [129]Xe following each excitation RF pulse applied at the gas-phase frequency. Figure 5.3 shows the pulse-sequence timing diagram for one repetition of the combined gas-phase, dissolved-phase multi-echo 3D radial acquisition.

Three-dimensional radial imaging was used because the very short T_2* values of dissolved-phase [129]Xe require short echo times to obtain adequate signal-to-noise ratios. A radial-out (half-echo) acquisition was used for the first echo of both the dissolved-phase and gas-phase portions of the pulse sequence to provide the shortest TE possible. The TR and flip-angle values can be adjusted to modify the contributions (i.e.,

relative amount and physical location) from the dissolved-phase compartments, yielding a total acquisition time of less than 10 sec or greater. In this work, however, fixed TR and flip-angle values were used to permit comparison among subjects. The pulse-sequence parameters included: TR 19 ms, TE1/TE2/TE3 0.74/2.36/3.98 ms for the dissolved phase and TE1/TE2 0.74/2.36 ms for the gas phase, flip angle 23° for the dissolved phase and 0.4° for the gas phase, and acquisition time 11 sec. Our current implementation provides 3D image sets covering the whole lung with a voxel volume of 7.6 x 7.6 x 17 mm^3, with the largest voxel dimension in the anterior-posterior direction. Undersampling was used to accelerate the acquisition. The corresponding acceleration factors were 2.8 for the half echoes and 1.4 for the full (symmetric) echoes. The golden-angle method was used for arranging the undersampling scheme among radial cones [108]. To provide whole-lung data for comparison with the image-based results, the pulse sequence also included collection of a free-induction decay (FID) for dissolved-phase ^{129}Xe at the end of the acquisition. The whole-lung values for the RBC fraction of the total dissolved-phase signal should closely match corresponding quantities calculated from the mean of values derived from 3D image sets. This data also permits estimation of the frequency difference between resonances and the average T_2* values. The FID was acquired using the same excitation RF pulse as the imaging portion of the pulse sequence. The data-acquisition period was 54 ms, starting 0.74 ms from the center of the RF pulse.
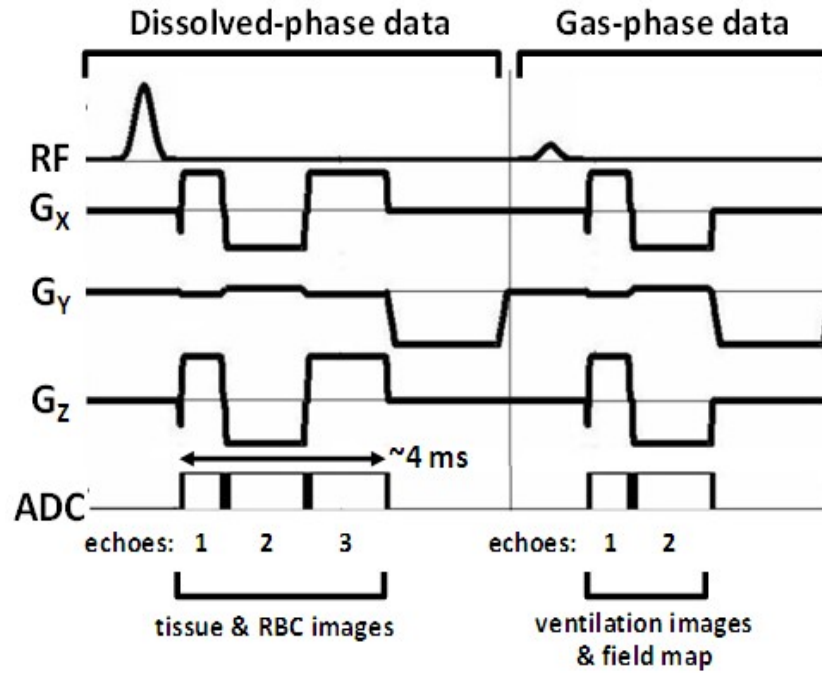
Figure. 5.3. Timing diagram for acquiring dissolved-phase and gas-phase ^{129}Xe images. During each TR, three echoes (a half-echo and two symmetric echoes) of dissolved-phase data are collected for calculation of tissue and RBC images, followed by two echoes of gas-phase data for calculation of ventilation images and a field map.

Protocol Optimization

Because of the very short T_2^* of dissolved-phase ^{129}Xe (about 2ms [90]), the choices for echo times are limited. But, choices for the TR and flip angle for the dissolved-phase signals are comparatively flexible. A simulation designed for optimization of the imaging SNR versus TR and FA was performed in MATLAB (Mathworks Inc., Natick, MA, USA), assuming T_1 of the gas phase is 20 s, T_1 of the dissolved phase is 6 s, the mean transit time of the exchange process between the gas phase and dissolved phase is 25 ms [117], the volume fraction of dissolved-phase to gas-phase xenon is 2%, FA for the gas phase is 0.4°, and the number of RF excitations is 520 (based on the imaging protocol).

The result of this simulation is shown in Figure 5.4. The maximum SNR occurs when the FA of the dissolved-phase excitation equals 24° and TR is 10 ms. However, the minimal TR of the 3D radial pulse sequence proposed above is 17 ms. For the studies in this dissertation, we used TR 19 ms and FA 23° for the dissolved-phase signals. The predicted SNR of this setting is shown by the black arrow in Figure 5.4. In future studies we plan to investigate whether the SNR can be improved by adjustment of the TR and FA values.
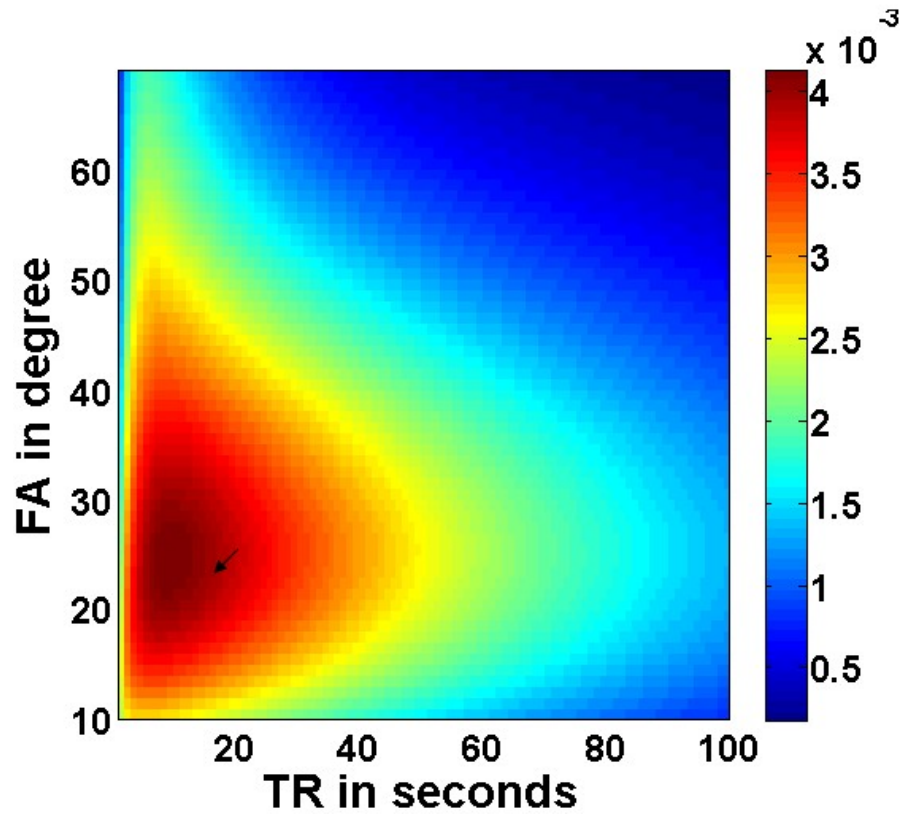
Figure 5.4. Predicted SNR for 3D dissolved-phase imaging versus flip angle (FA) and repetition time (TR). Arrow indicates the protocol we used in all human studies.

5.2.4 Image Reconstruction

The undersampled 3D radial image data were reconstructed using the quadratic penalized weighted-least-squares (QPWLS) via preconditioned conjugate gradients (PCG) algorithm [109]. To suppress image blurring secondary to depletion of the non-equilibrium hyperpolarized-gas magnetization during the acquisition, signal decay was compensated by normalizing the signal intensities for each echo time by the corresponding echo data recorded midway through the acquisition.

5.2.5 Separation of Tissue and RBC Components using the Hierarchical IDEAL Method

As discussed in Section 5.1.2, the multi-resolution approach of Hierarchical IDEAL, starting from the full image, subdivided into multiple overlapping regions, is particularly suitable for our study because, for current experimental conditions, the third echo of the dissolved-phase signals normally has a relatively low SNR of 7-10. Estimation of field and R2* ($1/T_2$*), moving from a larger image scale to a smaller scale, helps to reduce the estimation error. Also, in diseased subjects, regions with ventilation defects will lack gas-phase signal, but could still have dissolved-phase signal; acquiring B_0 maps in these regions using the gas-phase signals is thus inherently difficult.

We modified the Hierarchical IDEAL method to adapt it to our application. The reference B_0 maps acquired from the gas-phase images are used as an initial field map guess for the Hierarchical IDEAL method to separate the components, which helps to reduce the residual errors of estimation. For all subjects, the final B_0 field map output by the Hierarchical IDEAL algorithm was, in ventilated regions of the lung, within 10 Hz of

the input field map calculated from the two gas-phase echoes, which indicated that the B_0 and average T_2^* estimations were relatively accurate.
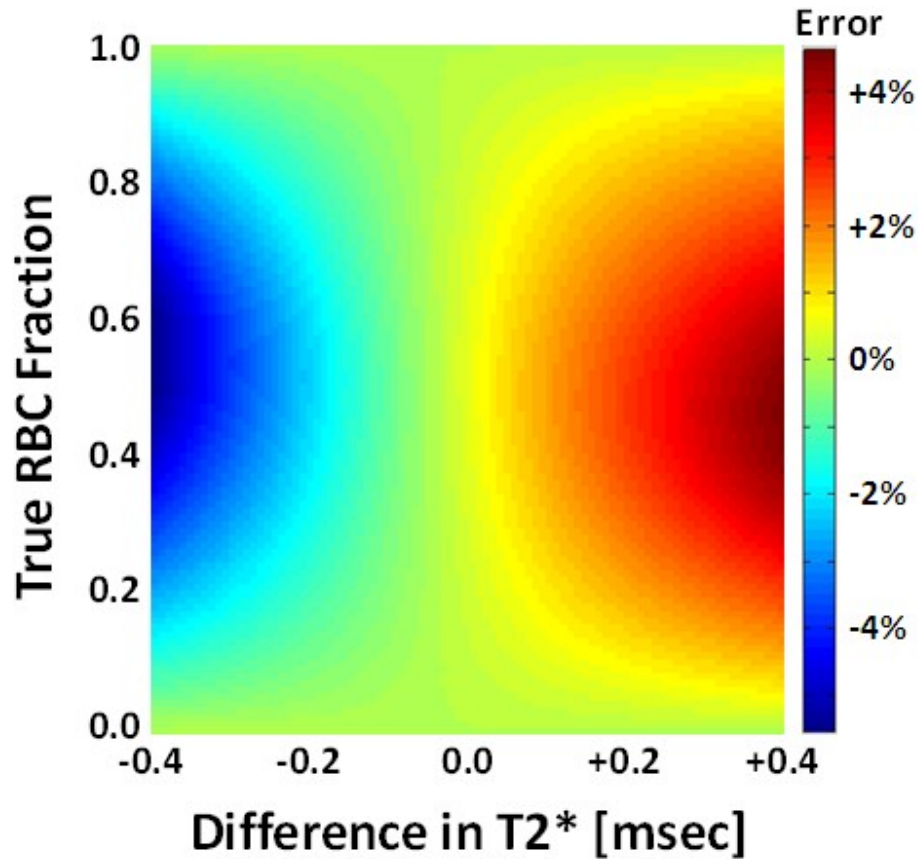
Figure 5.5. Theoretical prediction of the effect of a difference between the T_2^* for RBCs and that for tissue on the accuracy of tissue/RBC separation using the Hierarchical IDEAL algorithm. The predicted percentage error is shown as a function of the true (input value for the calculation) RBC fraction and the difference in T_2^* values, assuming a typical T_2^* value of 2.2 ms for tissue. For typical in-vivo values for T_2^* differences and RBC fractions we measured so far, the expected error is approximately 3% or less.

Because the T_2^* of dissolved-phase [129]Xe is particularly short (~2ms, [90]), and is comparable to the echo times, a difference between the T_2^* values of [129]Xe dissolved in tissue and RBCs may induce errors in the estimated amounts of these two components. To obtain an estimate of the impact of T_2^* variation among components on the accuracy of

the predicted component fractions, we performed a theoretical calculation using the Hierarchical IDEAL algorithm to determine the difference between input and estimated RBC fractions as a function of the T_2^* value for RBCs, assuming a typical T_2^* value of 2.2 ms for tissue. The theoretical calculations indicated that a difference between the T_2^* for RBCs and that for tissue should yield only minor errors in the predicted amounts of RBCs and tissue comprising the total dissolved-phase signal as determined using the Hierarchical IDEAL algorithm. Figure 5.5 shows the theoretically predicted percentage error in the fraction of RBCs as a function of the difference between the RBC and tissue T_2^* values. Over the range of differences expected in vivo (see T_2^* values in Tables 5.2 and 5.3), the maximum absolute error is approximately 5% and occurs when the RBC and tissue fractions are both about 0.5. For an RBC fraction of 0.3 or less, as typically found with our measurements in vivo, the absolute error is approximately 3% or less. This results also suggests that variations in T_2^* values across the lung, and within the range considered, should generate relatively small errors in the estimated amounts of RBCs and tissue comprising the total dissolved-phase signal.

5.2.6 Ratio Maps and Statistical Analysis

Coronal images depicting the distribution of ^{129}Xe dissolved in tissues and RBCs were calculated for each subject from the three dissolved-phase echoes using the Hierarchical IDEAL method [110-112], programmed in MATLAB. To eliminate background regions from subsequent analysis, a mask was created from the first echo of the dissolved-phase images using a signal-intensity-based threshold, and applied to the corresponding tissue and RBC images.

Because absolute dissolved-phase signal intensities have no physical meaning, four ratios were calculated for comparison among subjects; the ratios included total dissolved-phase signal (estimated for an echo time of zero) to gas, tissue-to-gas, RBC-to-gas, and RBC-to-tissue. For the RBC-to-tissue ratio, an additional mask, created from the tissue images using a signal-intensity-based threshold, was used to suppress isolated regions that exhibited high RBC signals but essentially no tissue signal, such as the heart. For comparison to gas, tissue and RBC images, coronal tissue-to-gas, RBC-to-gas and RBC-to-tissue ratio maps are presented on scales of 0.0 to 1.0, 0.0 to 0.5, and 0.0 to 0.7, respectively. For one subject with asthma who exhibited elevated RBC-to-tissue ratios, corresponding maps are presented on a scale of 0.0 to 1.0.

At each coronal slice position, mean values for the four ratios described above were calculated from the corresponding values within the ventilated region of the lung. To permit comparison of the slice-by-slice ratios among subjects with different lung sizes in the anterior-to-posterior direction, the values were plotted on a normalized scale, where 0 corresponds to the most anterior slice and 1 corresponds to the most posterior slice. Results from repeated acquisitions in three subjects were compared by calculating the difference between ratio values on a slice-by-slice basis and then averaging the absolute values of these differences, and also by calculating the difference between corresponding whole-lung values.

The mean and standard deviation of the four ratios were also calculated for the lung as a whole. Similarly, whole-lung mean values for the RBC fraction of the total dissolved-phase signal were calculated for comparison to corresponding values derived from FID data.

The whole-lung mean values for the ratios of total dissolved-phase signal to gas, tissue-to-gas, RBC-to-gas, and RBC-to-tissue from healthy subjects were compared to those from smokers and asthmatics using a two-tailed unpaired t-test. The RBC fractions derived from FID data were compared to those calculated from image data using a two-tailed paired t-test. A p-value of 0.05 or less was considered to be statistically significant.

5.2.7 FID Processing

As mentioned above, a free induction decay of the dissolved-phase signals was collected immediately following the imaging data for every 3D dissolved-phase/gas-phase acquisition. By analyzing the FIDs, certain properties of the ^{129}Xe dissolved in human lungs could be characterized at the global (whole-lung) level, including the fraction and T_2* values for the RBC and tissue (parenchyma/plasma) components for healthy and diseased subjects. This offered a global reference for analysis of the separated components by the Hierarchical IDEAL method, and also provided valuable information for optimizing the imaging protocols.

To explore the dependence of ^{129}Xe dissolved-phase signals on the degree of lung inflation, we also analyzed FIDs collected as part of Chemical Shift Saturation Recovery (CSSR) [116] experiments which were performed on 3 healthy subjects. These FIDs were acquired 100 ms after saturation of the dissolved-phase using flip angle 40-50°, readout duration 31 ms, and start time 0.7 ms. Excitation RF pulses were applied 3660 Hz above the gas-phase resonance frequency. FIDs were collected at three lung-inflation levels for each subject: (a) residual volume (RV), (b) after inhaling a gas volume of 1/2 forced vital capacity (FVC) from RV, and (c) total lung capacity (TLC). Because the excitation RF

pulse used in CSSR studies (Gaussian) generated a substantial signal from the gas phase, we filtered out the gas-phase signal in three steps: 1.) Filter out the dissolved-phase signals using a low-pass filter; 2.) Fit the real and imaginary parts of the gas-phase signals to a mono-exponential decay; and 3.) Subtract the fitted gas-phase signals composed of real and imaginary parts (fitted separately) from the original FIDs.

The complex FIDs were fitted to a bi-exponential decay model using 1stOPT (7D Soft High Tech. Inc., Beijing China). Parameters in the fit included R2* ($1/T_2$*) values, chemical shifts (resonance frequencies), fractions for the tissue and RBC components, and an initial phase difference between the components, as Eq. 5.1 shows.

$$s(t) = p * [f_r * e^{-j(w_r*t+\theta)-R2_r^**t} + (1-f_r) * e^{-j(w_t*t+\theta+\alpha)-R2_t^**t}] \quad \textbf{[Eq. 5.1]}$$

Parameters:

$s(t)$:   FID signal collected; p: theoretical signal intensity at echo time zero;

f_r :   RBC fraction; w_r: chemical shift of RBC component in rad/s;

θ :   common phase term; w_t: chemical shift of tissue component in rad/s;

α :   phase difference between RBC and tissue components;

t   : time;

$R2_r^*$:   R2* value of RBC component; and

$R2_t^*$:   R2* value of tissue component.

5.3 Results

5.3.1 Healthy Subjects

Multi-echo Dissolved-Phase Images
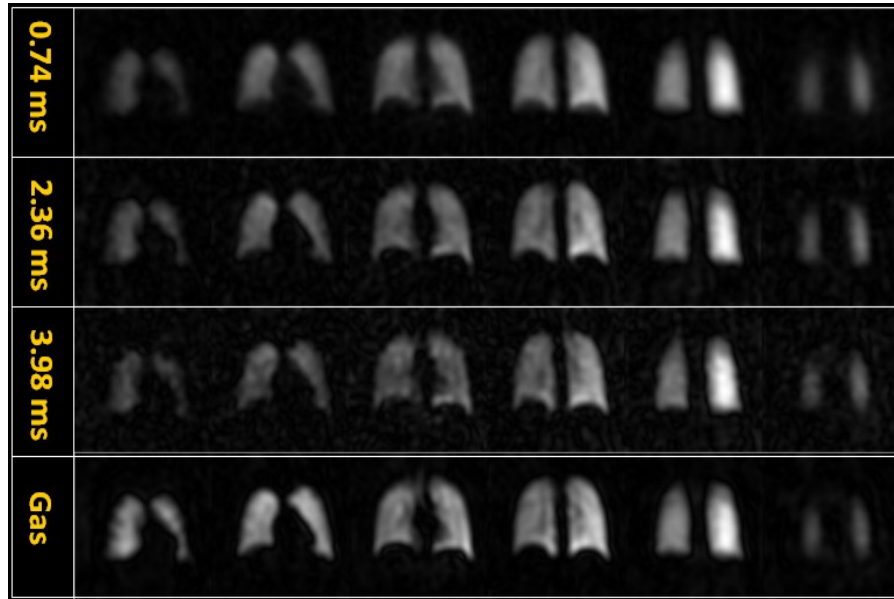
Figure 5.6. Dissolved-phase images at three echo times and gas-phase images acquired from healthy subject H3 using the 3D radial pulse sequence.

As described in Section 5.2.3, the 3D radial pulse sequence collects 3 echoes of dissolved-phase data and 2 echoes of gas-phase data. Figure 5.6 shows an example from healthy subject H3, presenting the images corresponding to the three echoes of dissolved-phase data and the second echo of gas-phase data from top row to bottom, reconstructed using the quadratic penalized weighted-least-squares (QPWLS) via preconditioned conjugate gradients (PCG) algorithm [109]. All of the gas-phase and dissolved-phase images show relatively uniform distribution of signals over the lung region, which is expected in healthy subjects. (The obvious left versus right signal

difference seen toward the posterior of the lung was caused by B_1 inhomogeneity in the flexible chest RF coil.)   Each echo of the dissolved-phase images is windowed based on its own maximum and minimum signal-intensity values.
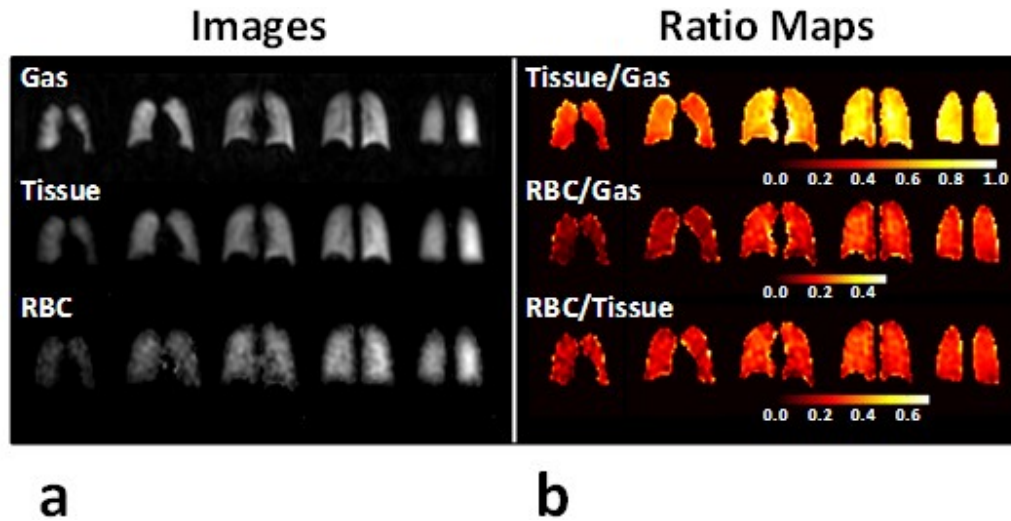
Figure 5.7. a.) Coronal gas, tissue and RBC images acquired from healthy subject H3. b.) Calculated tissue-to-gas, RBC-to-gas and RBC-to-tissue ratio maps.

Separation of the RBC and Tissue Components

As we discussed in Section 5.2.5, by using the Hierarchical IDEAL method with B_0 maps acquired from gas-phase images as an initial guess for the field map, we were able to separate the tissue and RBC components of ^{129}Xe dissolved in tissue and RBCs. Four of the healthy subjects (H1-H4) demonstrated generally uniform distributions of gas-phase signal intensities throughout the lung volume, and uniform dissolved-phase signal intensities within each coronal image slice, as demonstrated by the example shown in Figure 5.7a from healthy subject H3. Healthy subject H5, who is much older than the other healthy subjects, was found to have several ventilation defects in the gas-phase images. All healthy subjects showed increased dissolved-phase signal intensities toward the posterior of the

lung as also observed in previous studies [81, 89], consistent with the well-known gravity-dependent gradient in lung tissue density from anterior to posterior in the supine position. Regional maps were calculated on a pixel-by-pixel basis after thresholding to eliminate noise (Section 5.2.6). Analogous to the dissolved-phase signal intensities themselves, the tissue-to-gas and RBC-to-gas ratio maps clearly showed the anterior-to-posterior gradient.   However, the RBC-to-tissue ratio was more uniform from anterior to posterior, and was slightly higher in the mid-coronal slices for the subject shown in Figure 5.7b.
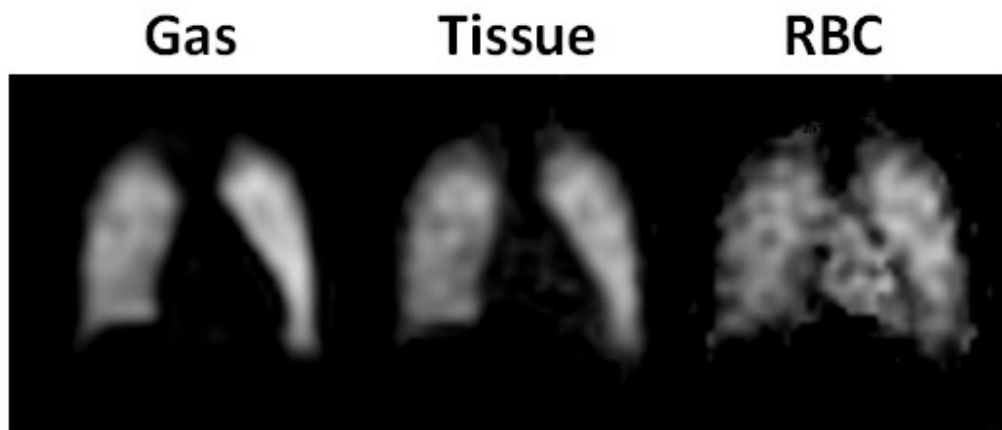
Figure 5.8. Representative coronal gas, tissue and RBC images from healthy subject H2. The RBC signal from the left ventricle of the heart (right) was clearly seen in this subject.

Portions of large vessels and/or part of or even the whole shape of heart chambers could be seen in the RBC images of some subjects, such as in the central slice in Figure 5.7a and also in Figure 5.8.   We postulate the variation in appearance of these structures among subjects might be associated with a variation of heart rate among subjects.

Mean Ratios in Coronal Slices
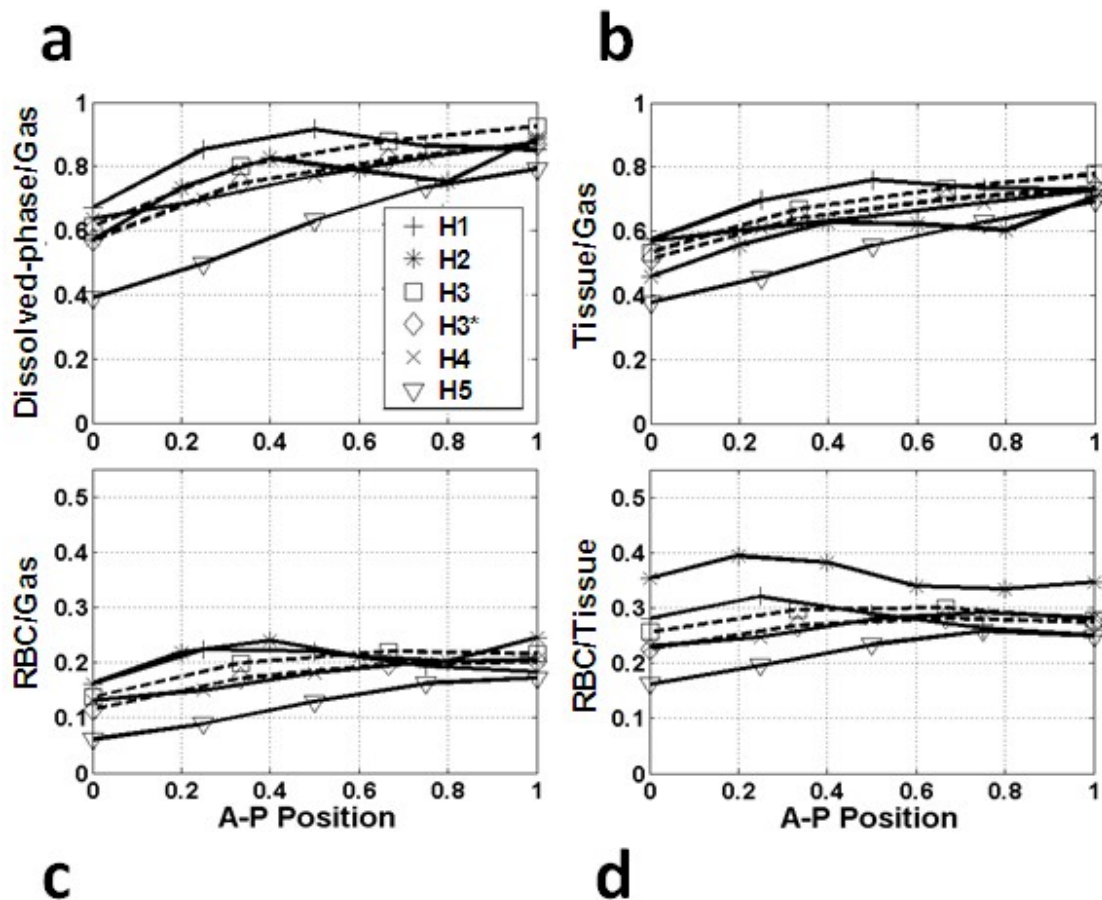
Figure 5.9. Calculated slice-by-slice ratios for all healthy subjects. Plots show the mean values for (a) total dissolved-phase to gas, (b) tissue-to-gas, (c) RBC-to-gas, and (d) RBC-to-tissue ratios for each coronal slice as a function of position along the anterior-posterior (A-P) direction. A value of 0 for A-P position corresponds to the most anterior slice and 1 corresponds to the most posterior slice. Subject H3 was imaged twice on the same day; H3* represents the repeated imaging. The values for this subject are plotted using dashed lines. The values of all ratios for H5 were generally lower than those from the other healthy subjects.

The four ratios that were calculated for each coronal slice are plotted in Figure 5.9 for the five healthy subjects, and the means and standard deviations of the ratios for the whole lung are plotted in Figure 5.16 (all subjects). The total dissolved-phase to gas,

tissue-to-gas, and RBC-to-gas plots show the general trend of increasing values from anterior to posterior, as discussed above, while the RBC-to-tissue ratio is generally flatter from anterior to posterior, but varies among subjects.   The slice-by-slice and whole lung values for all ratios (except RBC-to-tissue ratios for subject H2) were similar among healthy subjects H1 through H4, while the values for subject H5 (the oldest subject) were generally lower.

Comparison with ADC

Diffusion-weighted imaging was performed in healthy subjects H4 and H5, who had whole-lung ADC values of 0.033 ± 0.013 and 0.045 ± 0.009 cm^2/s (mean $\pm$ standard deviation), respectively, which were comparable to those for healthy subjects of similar age in the study of Kaushik et al [118], although our maximum b value (10 s/cm^2) was lower than that of Kaushik et al (12 or 18.76 s/cm^2).

5.3.2 Diseased Subjects Compared with Healthy Subjects

Multi-echo Dissolved-Phase Images

Smokers

The three smokers showed moderate to severe ventilation defects in ^{129}Xe gas-phase images. Subject S1, a clinically-healthy subject who had smoked for 15 years, showed just some minor defects in ventilation images and dissolved-phase images, most of which were located in the upper part of the lung (close to the apex), while the two subjects with smoking-related COPD (S2 and S3, GOLD Stage III) showed severe defects in the ventilation images. For subjects S2 and S3, the total dissolved-phase signals were much lower than those of the healthy subjects, which led to relatively low SNR in the multi-echo

dissolved-phase images. Also, their dissolved-phase images were very non-uniform. Figure 5.10 shows the three-echo dissolved-phase and second-echo gas-phase images acquired from the first acquisition in subject S2. (Because the SNR for the third-echo of dissolved-phase images acquired in subject S3 was relatively low, which adversely affects separation of the two components, only the total dissolved-phase results are shown for this subject.)

Asthmatics
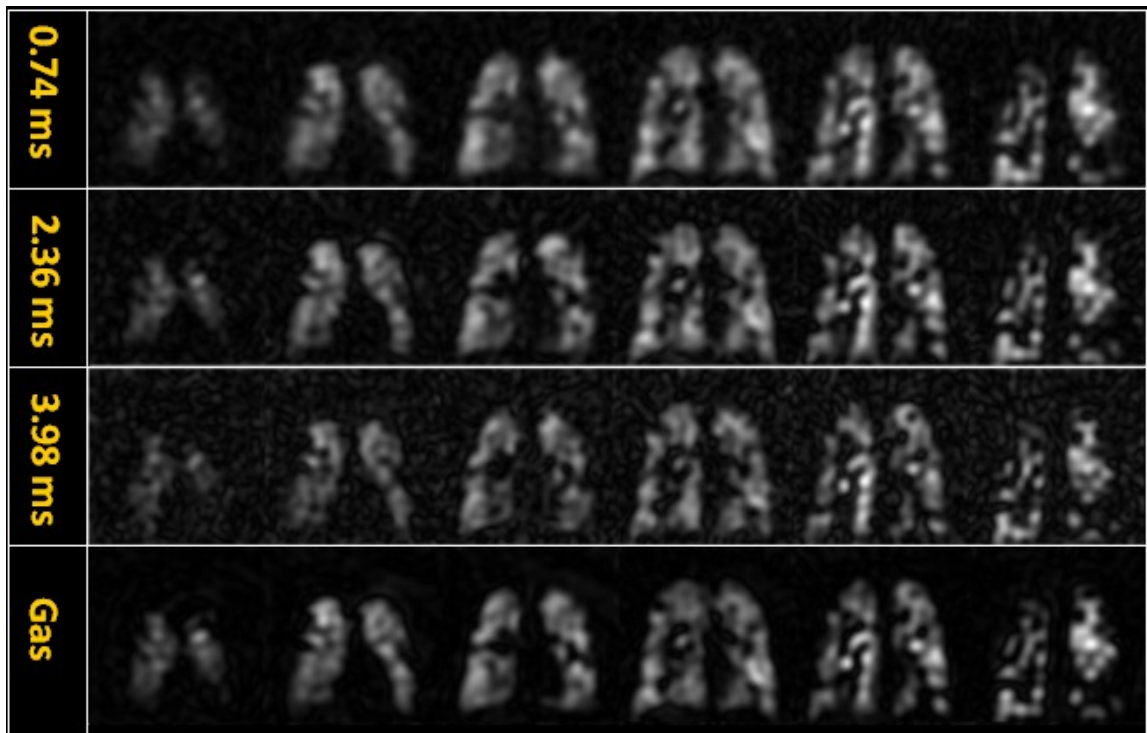
Figure 5.10. Dissolved-phase images at three echo times and gas-phase images acquired from COPD subject S2 using the 3D radial pulse sequence.

The two asthmatics included in this study were quite different in age (A1, 53 years; A2, 16 years). The older subject A1 showed relatively more ventilation defects, which varied between the two acquisitions (studies denoted by A1 and A1*, acquired on different days), while the younger subject A2 had just several minor defects or lower signal-intensity regions in both ventilation and dissolved-phase images. Figure 5.11

shows the three-echo dissolved-phase and second-echo gas-phase images acquired from subject A1.
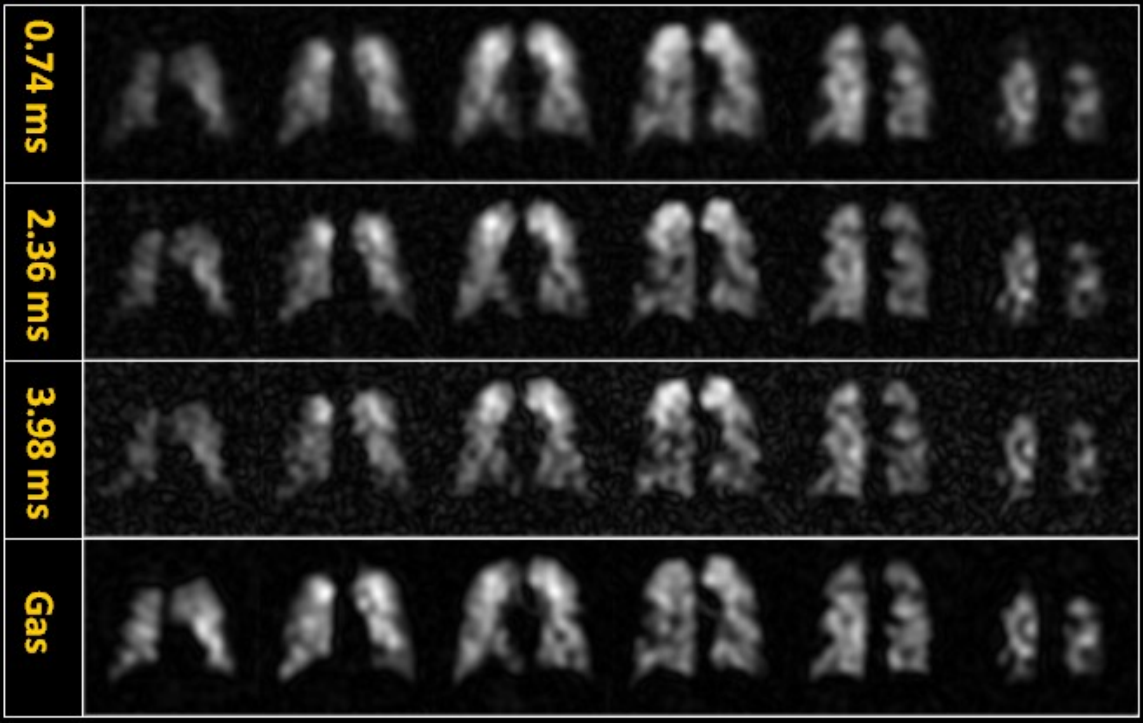
Figure 5.11. Dissolved-phase images at three echo times and gas-phase images acquired from asthmatic subject A1 using the 3D radial pulse sequence.

Separation of the RBC and Tissue Components

Smokers

Similar to the total dissolved-phase images, separated RBC and tissue images from subject S1 were relatively homogeneous with some minor defects, while the ones from subject S2 (Figure 5.12) show numerous defects, and much more mismatching between tissue and RBC images. Furthermore, compared with the healthy subjects such as shown in Figure 5.7, the ratio values for subject S2 were much lower, and the ratio maps at each

coronal position were more inhomogeneous and devoid of the anterior-to-posterior gradient.
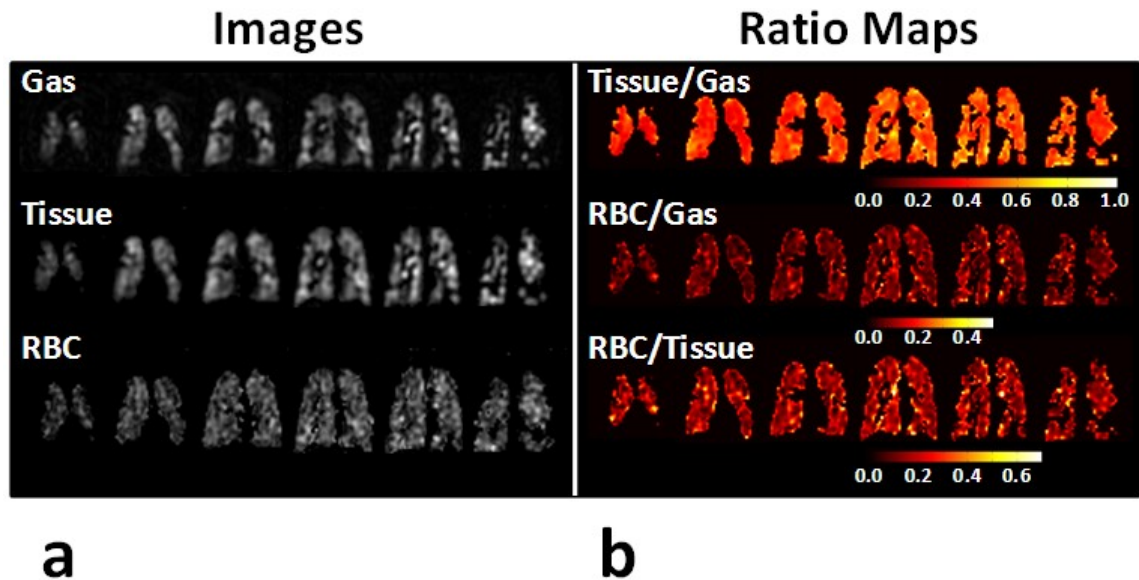
Figure 5.12. (a) Coronal gas, tissue and RBC images covering the whole lung, and (b) corresponding tissue-to-gas, RBC-to-gas and RBC-to-tissue ratio maps from subject S2 with COPD GOLD stage III. This subject showed many ventilation defects, inhomogeneous tissue and RBC images, and inhomogeneous ratio maps. The anterior-posterior gradient seen in healthy subjects was also absent.

Asthmatics

Gas, tissue and RBC images, as well as corresponding tissue-to-gas, RBC-to-gas and RBC-to-tissue ratio maps from the two asthmatics are shown in Figures 5.13 (A1) and 5.14 (A2). Both asthmatics exhibited ventilation defects, as expected. The ratio maps illustrate how both asthmatics differ from a healthy subject (Figure 5.7), but interestingly also how the two asthmatics differ substantially from one another, as discussed above. For example, while subject A2 showed relatively uniform tissue-to-gas ratios, subject A1 had elevated values in both apices in conjunction with reduced RBC-to-gas ratios (Figure

5.13b).   Subject A2 had some very high values for the RBC-to-tissue ratio (Figure 5.14b) in regions near ventilation defects in the gas-phase images.

Mean Ratios in Coronal Slices

Smokers

The values for the total dissolved-phase to gas, tissue-to-gas, and RBC-to-gas ratios for the smokers were generally lower than those for healthy subjects as seen in Figure 5.15 (slice-by-slice values for all diseased subjects compared to median values for healthy subjects).   While, compared to COPD, the clinically-healthy smoker (S1) had higher values for the total dissolved-phase to gas, RBC-to-gas, and RBC-to-tissue ratios. The tissue-to-gas ratios were similar for subjects S1 and S2.   Subject S1 showed anterior-to-posterior gradients, similar to those for the healthy subjects, in total dissolved-phase to gas, tissue-to-gas, and RBC-to-gas ratios, while the anterior-to-posterior variations for COPD subject S2 were much less.   However, subject S1 also showed an anterior-to-posterior gradient in the RBC-to-tissue ratio, as well as values higher than median values for healthy subjects. In contrast, subject S2 did not show a substantial anterior-to-posterior gradient in the RBC-to-tissue ratio, and the values were well below the median values for healthy subjects.
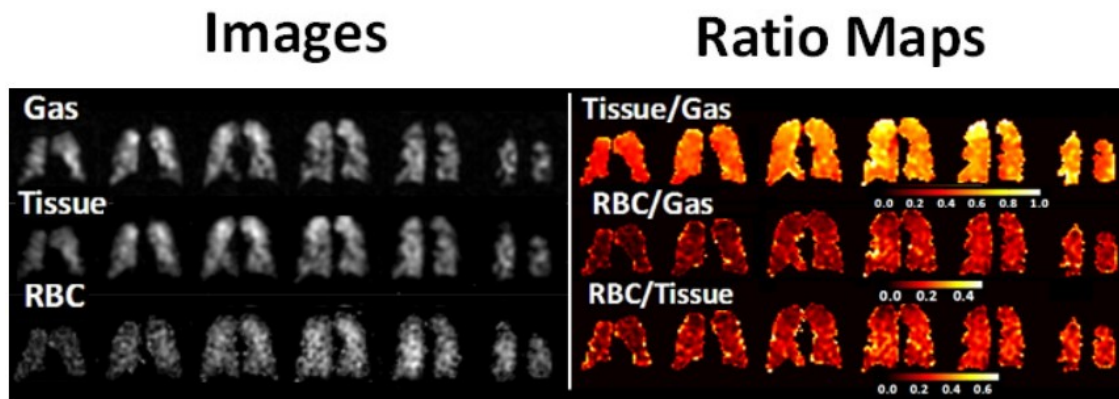
Figure 5.13. (a) Coronal gas, tissue and RBC images covering the whole lung, and (b) corresponding tissue-to-gas, RBC-to-gas and RBC-to-tissue ratio maps from subject A1 with asthma. This subject showed many ventilation defects, inhomogeneous tissue and RBC images, and inhomogeneous ratio maps.

Asthmatics

Except for RBC-to-gas ratios (Figure 5.15c), the results from the two asthmatics were markedly different; subject A1 showed higher values for total dissolved-phase to gas and tissue-to-gas ratios (Figure 5.15a, b), but much lower values for RBC-to-tissue ratios (Figure 5.15d). The ratio values for both asthmatics were lower than those for healthy subjects (Figure 5.15), with the exception of the RBC-to-tissue ratios for subject A2, which were higher than those for all other subjects in our study (Figure 5.15d).

Statistical Analysis

The means and standard deviations of the ratios for the whole lung are plotted in Figure 5.16 (all subjects). The whole-lung mean values for the ratios of total dissolved-phase signal to gas, tissue-to-gas and RBC-to-gas for the healthy subjects were significantly larger than those for the disease group (smokers and asthmatics, $p < 0.01$ for

all ratios).   The RBC-to-tissue ratio for the healthy subjects was not significantly larger than that for the disease group. When comparing the whole-lung values between healthy subjects and smokers or asthmatics, it is important to note that a substantial fraction of the standard deviation for healthy subjects is attributable to the physiological anterior-to-posterior gradient, whereas for many of the diseased subjects a substantial fraction of the standard deviation is attributable to the effects of the disease process.

Comparison with ADC

Smokers

The whole-lung ADC values for subjects S1, S2, and S3 were 0.043 ± 0.012, 0.056 ± 0.009, and 0.075 ± 0.014 cm^2/s, respectively.   The elevated ADC values for COPD subjects S2 and S3 are consistent with emphysema [118].   Subject S3, who had difficulty inhaling the total volume of gas, had a higher mean ADC in the lung parenchyma than any of those found in emphysema by Kaushik et al [118].   This high value suggests substantial tissue destruction, which is consistent with the very low dissolved-phase signal intensities for this subject (Figure 5.16a).

Asthmatics

The whole-lung ADC value for subject A1 was 0.049 ± 0.014 cm^2/s, which is toward the high end of normal values for the subject's age [118]. ADC data was not acquired in subject A2.

Characterization of Dissolved-phase ^{129}Xe by FID Analysis

Both the real and imaginary parts of all complex FIDs were fitted well. The average R^2 value for the fits was 0.994.   Therefore, as would be expected, the corresponding spectra

based on the fitted parameters were also very close to the original spectra. The quality of the fitting results is illustrated Figure 5.17, showing examples from healthy subject H3, COPD subject S2, and asthmatic subject A2.

Table 5.2 lists the fitted parameters obtained from the FIDs collected at the end of the 3D radial acquisitions. The resonance frequencies for both components were relatively consistent. RBC fractions found in most healthy subjects were higher than those for most diseased subjects (p=0.045), except subject S1, a long time smoker but clinically healthy, had an RBC fraction in the range of healthy values. Subject A2, a young asthmatic, had an RBC fraction higher than those for all of the healthy subjects. However, none of the healthy subjects in this study were as young as subject A2. Among the healthy subjects, T_2^* values of the RBC and tissue components were found to be consistent at 1.8-1.9 ms and 2.2-2.3 ms, respectively. Relative to healthy subjects, diseased subjects had slightly higher T_2^* values for the RBC component (p=0.024), and slightly lower T2* values for the tissue component (p=0.013).

Table 5.2. RBC fractions, and resonance frequencies (relative to +3660 Hz from the gas-phase resonance) and T_2^* values for the RBC and tissue components, obtained from fitting the dissolved-phase FIDs. RBC fractions calculated from image data are presented in the last row (value not calculated for subject S3 due to low SNR).

Sub	H1	H2	H3	H3*	H4	H5	S1	S2	S2*	S3	A1	A1*	A2
RBC Frac (%)	27	29	29	28	27	21	28	13	13	11	14	18	33
RBC Freq (Hz)	159	158	158	160	152	159	158	156	156	162	158	154	160
RBC T2* (ms)	1.8	1.8	1.8	1.8	1.9	1.9	1.9	2.2	2.2	2.2	2.2	2.0	1.7
Tiss Freq (Hz)	-181	-177	-174	-183	-177	-182	-182	-178	-178	-179	-176	-169	-174
Tiss T2* (ms)	2.2	2.2	2.2	2.2	2.3	2.2	2.1	2.0	2.0	2.1	2.2	2.2	1.9
RBC Frac (%) From Images	24	28	23	23	23	20	27	14	15	*	16	19	32

As mentioned in Section 5.2.7, to investigate the effects of lung inflation level on RBC fraction, and RBC and tissue T_2* values, FIDs collected as part of CSSR acquisitions at three lung inflation levels were also analyzed. Results are shown in Table 5.3. As the lung volume increased from RV to TLC, the RBC fraction decreased by approximately 30%. The T_2* of the RBC component was relatively insensitive to lung inflation level, but the T_2* of the tissue component decreased with increasing lung inflation.

RBC fractions from FID data were consistent with those from imaging data. The mean absolute difference between the two groups of data is 2.3%.

Table 5.3. RBC fraction and T_2* values corresponding to the three lung-inflation levels (RV, RV + 1/2 FVC and TLC) from CSSR acquisitions.

Subject	H6			H7			H8		
Inflation Level	RV	1/2FVC	TLC	RV	1/2FVC	TLC	RV	1/2FVC	TLC
RBC Frac (%)	36	31	23	35	31	24	29	20	20
RBC T2* (ms)	1.7	1.7	1.7	1.8	1.7	1.7	1.8	1.7	1.7
Tiss T2* (ms)	2.3	2.0	2.0	2.3	2.1	2.0	2.4	2.1	2.1

5.4 Discussion and Conclusion

We have demonstrated a 3D radial trajectory pulse sequence that acquires multi-echo ^{129}Xe dissolved-phase and gas-phase images covering the whole human lung during a short breath-hold of 11 sec. By using the Hierarchical IDEAL method, originally developed to separate water and fat in proton MRI, we decomposed the multi-echo dissolved-phase signals into two components: ^{129}Xe dissolved in RBCs and ^{129}Xe dissolved in tissue (lung parenchyma and blood plasma). Conventional chemical shift imaging provides an alternative approach for obtaining this information from the lung

[85], and Reis et al [119] recently presented results for 3D chemical shift imaging of ^{129}Xe in humans. Nonetheless, full phase-encoding of the ^{129}Xe signals is inefficient compared to the approach demonstrated here; the implementation shown by Reis et al [119] required a breath-hold duration of more than 20 s while providing voxel volumes roughly 8 times larger than those presented in our work.

The pulse-sequence parameters were chosen to yield high SNR despite the low dissolved-phase signal strength and its short T_2^* values. Besides the effect of T_1 and T_2^* relaxation, the precise signal composition for any flip angle, TR combination depends on a variety of factors including the alveolar surface-to-volume ratio, alveolar wall thickness, xenon solubility, hematocrit, pulmonary perfusion, and tissue composition (which may be altered in diseased subjects, e.g., by inflammation or fibrotic deposits), as well as any other factors that affect the diffusional processes by which the ^{129}Xe atoms exchange between the various compartments. In general, the contribution from any given dissolved-phase ^{129}Xe component decreases in proportion to the number of excitation RF pulses it has experienced and the associated flip angles for the pulses. Thus, because a low flip angle was used for our experiments, the resulting dissolved-phase signals reflect contributions originating from ^{129}Xe atoms at various distances from the exchange sites. If the flip angle is sufficiently small and the TR sufficiently long for a given perfusion rate, it is feasible in humans to image ^{129}Xe in the RBC compartment as far downstream as the left ventricle of the heart (Figure 5.8). Due to the higher heart rate and the shorter distances that need to be traversed, the ascending aorta can be depicted in small animals such as rabbits [91].
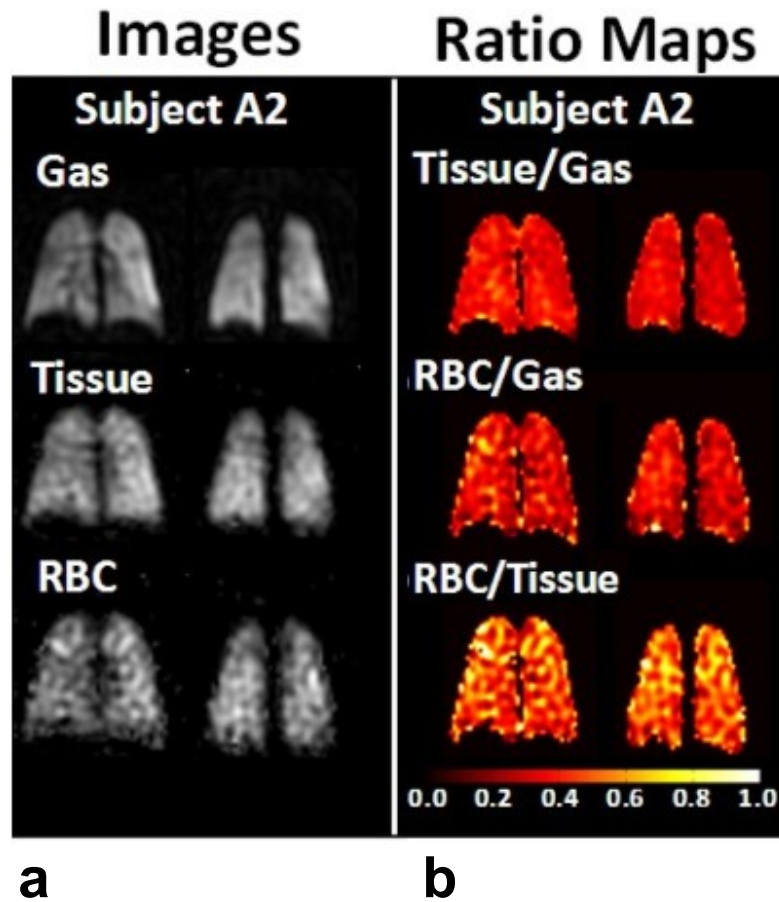
Figure 5.14. (a) Coronal gas, tissue and RBC images at two slice positions, and (b) corresponding tissue-to-gas, RBC-to-gas and RBC-to-tissue ratio maps from subject A2 with asthma. The RBC/Tissue ratios in this subject were higher than those for all other subjects, and so are presented on a scale of 0 to 1.0 (versus 0 to 0.7 for others).

The total dissolved-phase to gas ratio reflects ^{129}Xe gas-uptake efficiency by the lung parenchyma within a timeframe dictated by the selected pulse-sequence parameters. The tissue-to-gas ratio is primarily indicative of the entire alveolar wall volume, but does not
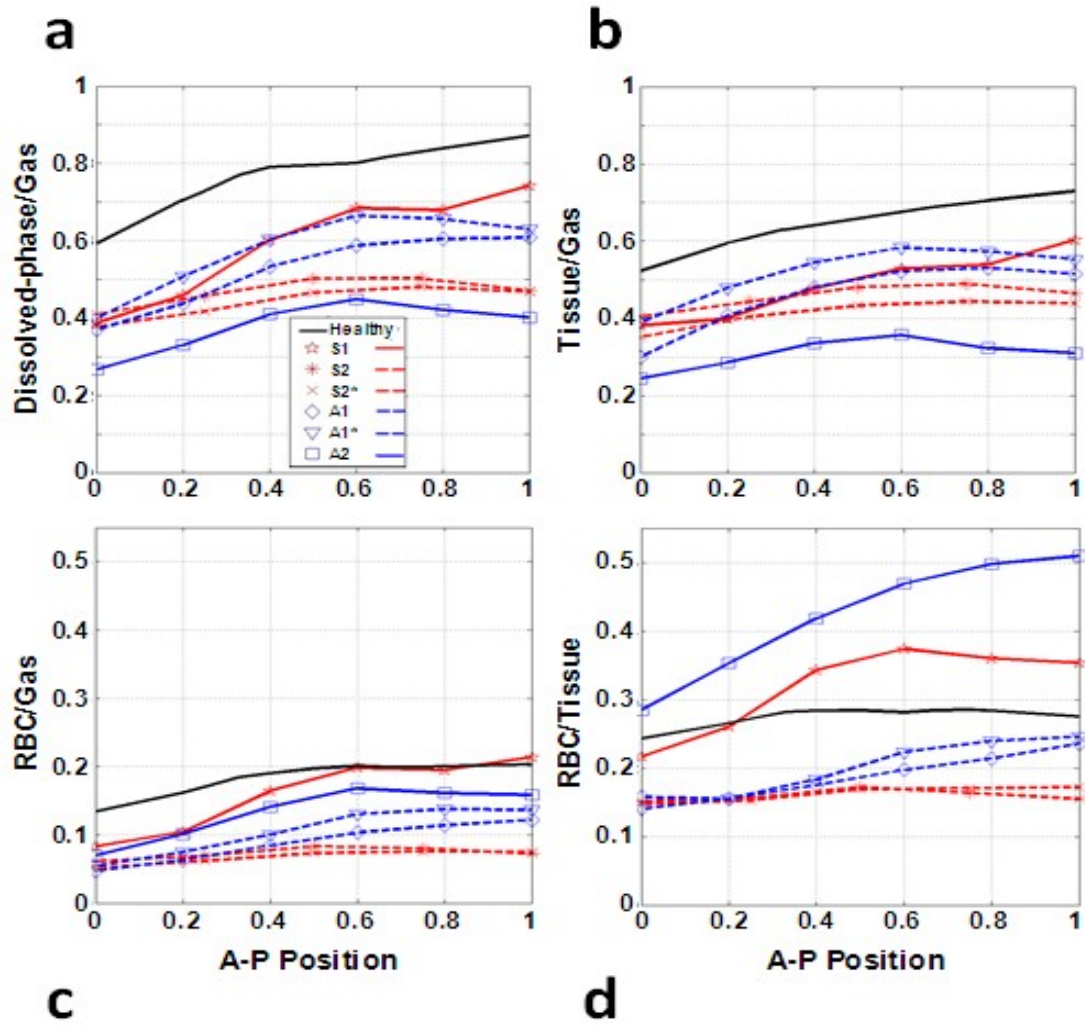
Figure 5.15. Calculated slice-by-slice ratios for smokers and asthmatics. Plots show the mean values for (a) total dissolved-phase to gas, (b) tissue-to-gas, (c) RBC-to-gas, and (d) RBC-to-tissue ratios for each coronal slice as a function of position along the anterior-posterior (A-P) direction. Smokers are plotted in red and asthmatics are plotted in blue. For comparison, the solid black line shows the median of ratio values for healthy subjects, shown in Figure 5.9. S2* and A1* denote the repeat imaging for these two subjects (S2* obtained on the same day as S2, A1* obtained on a different day than A1).
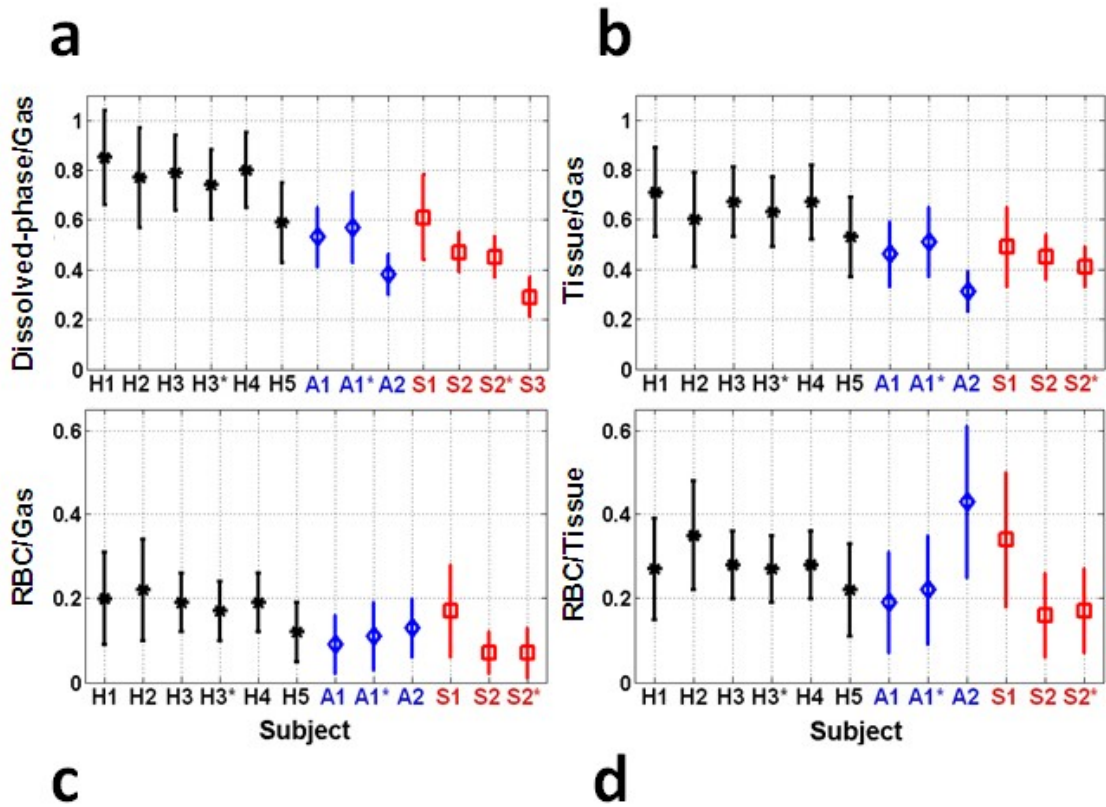
Figure 5.16. Whole-lung ratio values for all subjects. Means (plotting symbols) and standard deviations (vertical bars) are shown for (a) total dissolved-phase to gas, (b) tissue-to-gas, (c) RBC-to-gas, and (d) RBC-to-tissue ratios. Healthy subjects, asthmatics and smokers are shown in black, blue and red respectively. Because the dissolved-phase signal intensities for subject S3 were very low, preventing accurate separation of the tissue and RBC components, only the total dissolved-phase to gas ratio is shown.

reveal whether a deviation from its normal value is due to a change in alveolar size (number of walls per unit volume), a change in alveolar wall thickness, or a combination of both. The RBC-to-gas ratio quantifies ^{129}Xe transport from the alveolar airspaces to the bloodstream, similar to the diffusion capacity of the lung for carbon monoxide (DLCO) global lung-function test. Finally, the RBC-to-tissue ratio might reveal disease-related

shifts in the relative compartment sizes.   For example, a decrease in this ratio in a subject with normal hematocrit could suggest thickening of the alveolar walls.
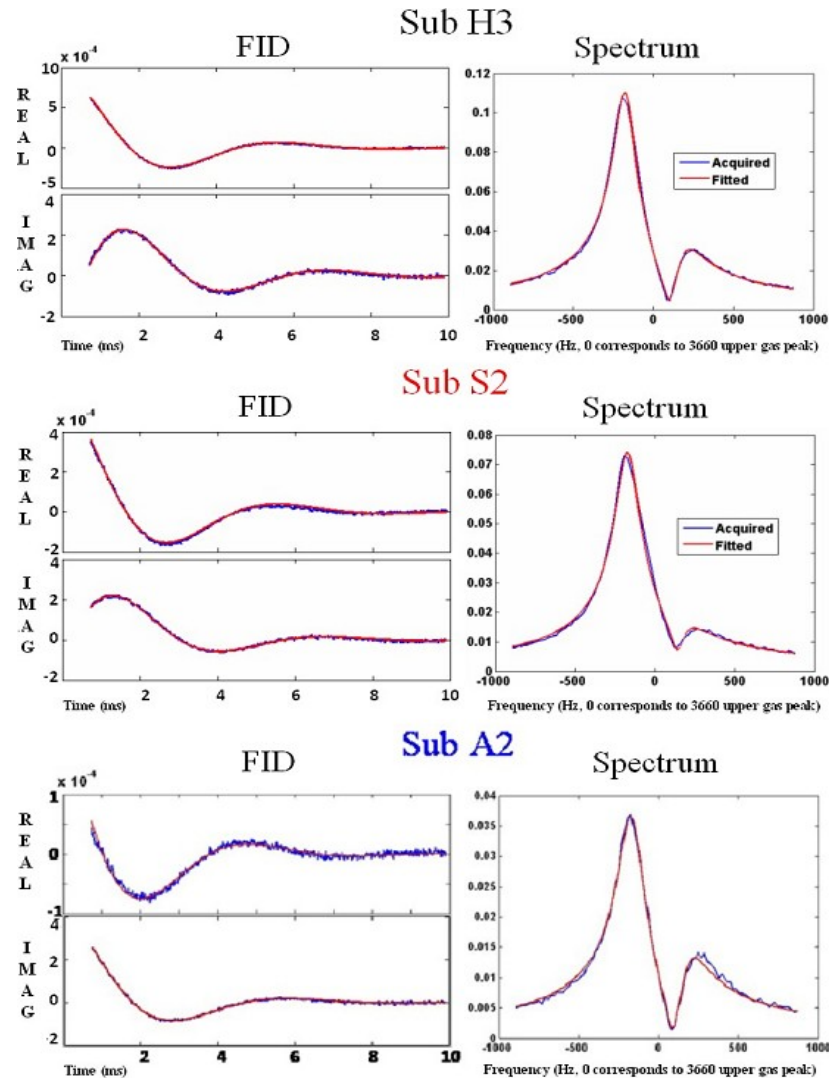
Figure 5.17. Fitted FIDs and corresponding spectra from healthy subject H3, COPD subject S2 and asthmatic subject A2. Blue shows acquired data, red shows FID and spectra calculated based on fitting results.

As expected, in healthy subjects, we found that the ventilation, tissue and RBC images, as well as their associated ratios discussed above, were uniform within coronal slices of the lung.   We also observed an anterior-posterior gradient in the ratio maps and ratio plots that

reflects the well-documented tissue compression in dependent areas of the lung. On the other hand, the 3D image sets acquired from subjects with obstructive lung disease (COPD and asthma) revealed inhomogeneous distributions in the images as well as in the ratio maps, and slice-by-slice and whole-lung ratio values which differed from those for healthy subjects. However, one potential issue of this exploratory study was that the majority of the healthy subjects were much younger than the COPD subjects.

The two COPD GOLD Stage III subjects had low total dissolved-phase to gas ratios, which is consistent with the high ADC values found with diffusion-weighted imaging, indicating an increase of the average distance between alveolar walls due to tissue destruction. The RBC-to-tissue ratio was also low in one of these subjects, which might indicate thickening of the alveolar walls secondary to inflammation, which would reduce the amount of ^{129}Xe diffusing to the RBCs while increasing the volume of the tissue compartment. This indication of wall thickening in COPD is consistent with that found by Dregely et al [83, 120] using the multiple-exchange-time xenon polarization transfer contrast technique. Alternatively, decreased pulmonary capillary perfusion could also cause a low RBC-to-tissue ratio, and patients with COPD are known to have pulmonary vascular pruning apparent on pulmonary angiography. Interestingly, the clinically-healthy smoker exhibited a lower than normal tissue-to-gas ratio, while the RBC-to-gas ratio was similar to those for healthy subjects and the RBC-to-tissue ratio was somewhat elevated. This could indicate generally normal alveolar wall thickness, but some of the alveolar walls are destroyed due to the onset of emphysematous tissue destruction.

The two asthmatics showed markedly different patterns. The changes in subject A1, a 53-year-old male who exhibited numerous ventilation defects, were qualitatively similar to

those in COPD subject S2, suggesting increased alveolar wall thickness in conjunction with hyperexpansion or mild emphysema-like tissue destruction in this asthmatic. In the 16-year old asthmatic A2, we found a very high RBC-to tissue ratio, which, overall, was even higher than those in healthy subjects. However, the total dissolved-phase to gas and tissue-to-gas ratios were very low, possibly due to hyperexpansion. A frequent finding in asthmatics is an elevated residual volume, which, if present in our asthmatic subjects, could result in decreased tissue-to-gas ratios. Perhaps the young asthmatic (A2) had an increased cardiac output to compensate for his lung disease, resulting in the high RBC-to-tissue ratio.

In three subjects we tested the repeatability of the acquisition method introduced in this study. The results for repeated acquisitions were reasonably consistent: percent differences between repeated acquisitions for the four ratios, averaged over 3 subjects (H3, A1 and S2) were approximately 10% or less. The biggest difference was seen on subject A1, who was imaged on different days and was found to have distinct differences in ventilation images. Clearly the lung inflation level may affect certain characteristics of the exchange sites. As shown in Table 5.3, the RBC fraction and tissue T_2* were found to depend on the level of lung inflation. The RBC fraction decreased with increasing lung volume suggesting that gas exchange is reduced at high lung volumes. The RBC fraction was significantly lower in the diseased subjects than in healthy subjects, as presented in Table 5.2. Both asthma and smoking-related lung disease are known to increase RV of the lung, that is, the lung volume at maximum expiration. An increase in RV would mean that lung volume at imaging of the diseased subjects was effectively larger than for healthy subjects, and could partially explain the decreased RBC fraction found in diseased subjects.

But the RBC fraction in diseased subjects was much lower than in healthy subjects at maximum inspiration (TLC), suggesting that factors other than just lung inflation level may cause impaired gas exchange.

We are currently investigating approaches for measuring the level of lung inflation using proton image sets acquired during the same breath hold period, and assessing whether the various ratio values can be corrected or normalized based on the level of lung inflation.

In conclusion, we have demonstrated an imaging method that permits regional mapping of the tissue and RBC fractions of ^{129}Xe dissolved in the human lung, as well as quantitative comparison of tissue- and RBC-based ratios among subjects. The 11-sec breath-hold acquisition was well tolerated by both healthy volunteers and subjects with obstructive lung disease. Our preliminary results, although obtained from a small number of subjects in this exploratory study, suggest marked differences in the spatial distributions and overall amounts of ^{129}Xe dissolved in tissue and RBCs among healthy subjects, smokers (including those with COPD), and asthmatics. Additional studies, including more subjects and appropriate age matching, are clearly warranted to fully assess the potential of this technique.

Chapter 6

Conclusions and Future Work

6.1 Conclusion

In the work presented in this dissertation, we first demonstrated development of a phase-based method for transmitter calibration utilizing Shinnar-Le Roux (SLR) RF pulses, optimized for the off-resonance and peak B_1 constraints of hyperpolarized-gas lung imaging [94]. Accuracy of this method was evaluated through: (1) theoretical simulation using the Bloch-Siegert equation; (2) phantom tests using 3-dimensional B_1 and B_0 mapping, and comparison with the amplitude-based calibration method routinely used for HPG imaging [54] and the phase-based calibration method based on a spin-echo pulse sequence [**53**]; and (3) comparison with the amplitude-based calibration method in a large number of human studies. Results showed that this phase-based method has a dependency on the homogeneity of the B_0 field, but it remains reasonably accurate even for very inhomogeneous B_0 distributions, as found in the lungs of severely diseased subjects or near the diaphragm. Because of its very small magnetization consumption (less than 5%) and short acquisition time (less 100ms), it can be integrated with any imaging pulse sequence for hyperpolarized-gas studies, and offers an automatic and relatively accurate adjustment of the transmitter voltage. It is thus functionally equivalent to the calibration procedures for proton studies integrated into the software of commercial MR scanners.

To address the need for accelerating combined 3D ^{3}He/^{1}H imaging acquisitions in human studies, we incorporated the concept of compressed sensing [73]. We designed an undersampling pattern based on simulation using previously acquired human-lung images, and reconstructed undersampled images by seeking converged solutions in the wavelet domain. The reconstruction fidelity of the reconstructed images was verified through: (1) simulation based on fully-sampled datasets; (2) direct quantitative comparison of fully-sampled and undersampled image sets acquired in the same breath-hold; and (3) direct quantitative comparison of ventilation defects found in fully-sampled and undersampled image sets, acquired in different breath-holds, through image registration and segmentation [102]. High similarities were found between the fully-sampled and CS reconstructed undersampled images. Observed differences were caused primarily by factors unrelated to the CS technique, including diaphragm movement between breath-holds, the non-equilibrium nature of hyperpolarized-gas magnetization, and variation in ventilation defects between breath-holds. The total image-acquisition time was reduced to less than 10 seconds, which is suitable for even severely diseased subjects.

This dissertation also proposed a 3D radial pulse sequence for a multi-echo ^{129}Xe dissolved-phase and gas-phase image acquisition. Using optimized imaging protocols, we were able to acquire three echoes of xenon dissolved-phase images, and gas-phase images with matching resolution, in a breath-hold duration of about 10 seconds, and thereby realized regional mapping of the tissue and RBC fractions of ^{129}Xe dissolved in the human lung through separation of RBC and tissue components using the Hierarchical IDEAL method [112]. Four ratio maps were calculated for quantitative assessment of

lung function: total dissolved-phase to gas, tissue-to-gas, RBC-to-gas, and RBC-to-tissue. In preliminary human studies, healthy subjects showed generally uniform distribution of signals in all images and ratio maps within coronal slices, and were found to have the well-known anterior-to-posterior gradient due to gravity in all images and ratio maps except the RBC-to-tissue maps. In contrast, diseased subjects show moderate to severe inhomogeneity in images and ratio maps, depending on disease type and severity. The ratios for diseased subjects (COPD and asthmatics) were very different than those for healthy subjects. The mean ratios over slices and whole-lung mean ratios of total dissolved-phase to gas, tissue-to-gas and RBC-to-gas from all diseased subjects were below the median values for healthy subjects.

6.2 Future Work

6.2.1 Phase-based Calibration

The results from the phase-based calibration method were found to be consistent with those from the amplitude-based method in more than one hundred human studies we did in the past 2-3 years. We need to continue the verification of the phase-based calibration method through more studies. For instance, we can use the phase-based B_1 mapping method proposed by Santoro et al [59], but replace the hard pulse [59] with the SLR pulse we designed. By choosing the appropriate protocol, we will be able to determine the theoretical prediction for calibration using the B_1 mapping results from a human, as we already did in the phantom test (Section 3.3.1). Also, 3D B_0 mapping in diseased subjects will be helpful to analyze the accuracy or potential pitfalls of the phase-based calibration method. When the accuracy of the phase-based method is further verified,

we can probably modify the current pulse sequence to make it change the transmitter voltage automatically based on calibration results calculated by the online ICE (reconstruction) program. Then, the following imaging pulse sequence could be executed with the adjusted transmitter voltage, eliminating the need for a separate bag of hyperpolarized gas for calibration.

6.2.2 Accelerated Combined ^{3}He/^{1}H Acquisitions using the Compressed Sensing Technique

In the near future, we plan to collect more data from diseased subjects and continue to use the segmentation method [102] to quantitatively compare the ventilation defects between the fully-sampled and undersampled image sets. Also, online image reconstruction (ICE) programs are needed for the undersampled acquisitions before the undersampled protocol can replace the fully-sampled protocols currently used.

6.2.3 Regional Mapping of Gas Uptake by Red Blood Cells and Tissue using ^{129}Xe

This project was just started recently. In the near future, we plan to image more diseased subjects and age-matched healthy subjects, and quantitatively analyze the results. For evaluation purposes, some of these subjects will undergo CT scans to investigate the tissue structure in their lungs. Also, imaging of lung perfusion and measurement of ADC maps would be helpful to understand the different phenotypes and progression of disease.

In the long term, there is much potential to improve the current imaging strategies and to explore new imaging strategies, such as using parallel imaging to improve the SNR (e.g., by allowing access to a wider range of repetition times) or enhance the image

resolution. Also, the sampling trajectory or undersampling pattern can be optimized to yield better image quality. On the basis of improved SNR, different protocols [91] could be tested to explore more valuable information on lung function.

6.3   Collaborations and Contributions

This dissertation includes many efforts from inside and outside Dr. John Mugler's lab, and it would not have been possible to finish it without their work, help and suggestions. I want to express my thanks to all of them and apologize for those missed.

The initial idea of phase-based calibration/B_1 mapping method is inherited from Dr. John Mugler. The reconstruction of undersampled ^{3}He and ^{1}H datasets are reconstructed using the SparseMRI toolbox provided by Dr. Micheal Lustig. Dr. John Mugler proposed the original idea of separating the excitation of dissolved-phase and gas-phase xenon signals, and provided a series of possible solutions for optimizing the SNR of signals. Dr. Kai Ruppert provided plenty of reference data to help investigate the signal behavior of dissolved-phase xenon. The original radial sequence was composed by Dr. Wilson Miller. The original Hierarchical IDEAL separation codes are developed by Dr. Jeffrey Tsao and Yun Jiang. The 3D radial data is reconstructed using IRT toolbox published by Dr. Jeffrey A. Fessler.

The three projects were mainly done by the author, while certainly all the work in this dissertation is attributed to the guidance of Dr. John Mugler.

Appendix - Publications and Conference Abstracts

A.1 Journal Publications

[1] **Qing K**, Ruppert K, Jiang Y, Mata JF, Miller GW, Shim MY, Wang C, Ruset IC, Hersman WF, Altes TA, Mugler JP III. Regional mapping of gas uptake by blood and tissue in human lung using hyperpolarized Xenon-129 MRI. J Magn Reson Imaging 2013. (Accepted pending revision.)

[2] **Qing K**, Miller GW, Altes TA, Mata JF, de Lange EE, Tobias WA, Cates GD Jr., Ruset IC, Hersman FW, Brookeman JR, Mugler JP III. Optimization and validation of phased-based transmitter calibration for hyperpolarized-gas MRI of the human lung. (Draft completed.)

[3] **Qing K**, Altes TA, Tustison NJ, Mata JF, Miller GW, de Lange EE, Tobias WA, Cates GD Jr., Brookeman JR, Mugler JP III. Combined spatially-registered proton and hyperpolarized 3He 3D image sets of the human lung acquired in less than 10 seconds using compressed sensing. (Draft completed.)

[4] Wang C, Altes TA, Mugler JP III, de Lange EE, Mata JF, **Qing K**, Hersman FW, Ruset IC, Verbanck S. Experimental measurements and computer simulation of long-time-scale hyperpolarized ^{3}He and ^{129}Xe diffusion in human lungs. Magn Reson Med 2012. (Submitted.)

[5] **Qing K**, Bai J. Portable ECG Monitor based on ARM. Beijing Biomedical Engineering. 2008 Feb; 27(1): 72-74.

A.2 Conference Publications

[1] **Qing K**, Altes TA, Tustison NJ, Mata JF, Miller GW, de Lange EE, Tobias WA, Cates GD Jr., Brookeman JR, Mugler JP III. Quantitative Assessment of Compressed-Sensing Reconstruction Fidelity for 3D He-3 and H-1 Acquisitions in One Breath-hold. Proceedings of the International Society for Magnetic Resonance in Medicine 4003; 2012. Twentieth Meeting, Melbourne, Australia.

[2] **Qing K**, Miller GW, Altes TA, Mata JF, de Lange EE, Tobias WA, Cates GD Jr., Ruset IC, Hersman FW, Brookeman JR, Mugler JP III. Improved Phase-Based Transmitter Calibration for Hyperpolarized-Gas MRI using Shinnar-Le Roux RF Pulses. Proceedings of the International Society for Magnetic Resonance in Medicine 912; 2011. Nineteenth Meeting, Montreal, Canada.

[3] **Qing K**, Altes TA, Tustison NJ, Mata JF, Miller GW, de Lange EE, Tobias WA, Cates GD Jr., Brookeman JR, Mugler JP III. Acquisition of Spatially-registered Helium-3 and Proton 3D Image Sets of the Lung in less than 10 seconds using Compressed Sensing. Proceedings of the International Society for Magnetic Resonance in Medicine 1349; 2011. Nineteenth Meeting, Montreal, Canada. (**Oral**)

[4] **Qing K**, Miller GW, Mugler JP III. Performance of Three Transmitter Calibration Methods for Hyperpolarized Gas MRI in the Presence of B0 and B1 Inhomogeneity. Proceedings of the International Society for Magnetic Resonance in Medicine 2574; 2010. Eighteenth Meeting, Stockholm, Sweden.

[5] **Qing K**, Pan L, Fetics B, Wacker FK, Valdeig S, Philip, M, Roth A, Nevo Erez, Kraitchman DL, van der Kouwe AJ, Lorenz CH. A Multi-slice Interactive Real-time Sequence Integrated with the EndoScout Tracking System for Interventional MR

Guidance. Proceedings of the International Society for Magnetic Resonance in Medicine 4429; 2010. Eighteenth Meeting, Stockholm, Sweden.

[6] Mugler JP III, Mooney KE, Altes TA, Mata JF, **Qing K**, de Lange EE, Tobias WA, Brookeman JR, Cates GD Jr., Miller GW. High-quality ventilation imaging of the human lung using 100 ml of helium-3. Proceedings of the International Society for Magnetic Resonance in Medicine 1357; 2012. Twentieth Meeting, Melbourne, Australia.

[7] Ruppert K, Altes TA, Ruset IC, Miller GW, Mata JF, **Qing K**, Tsentalovich I, Hersman FW, Mugler JP III. Detection of a long-T2 dissolved-phase Xe129 component in the human chest. Proceedings of the International Society for Magnetic Resonance in Medicine 1349; 2012. Twentieth Meeting, Melbourne, Australia.

[8] Mugler JP III, Altes TA, Ruset IC, Miller GW, Mata JF, **Qing K**, Tsentalovich I, Hersman FW, Ruppert K. Image-based measurement of T2* for dissolved-phase Xe129 in the human lung. Proceedings of the International Society for Magnetic Resonance in Medicine 1347; 2012. Twentieth Meeting, Melbourne, Australia.

References

[1] Centers for disease control and prevention. National surveillance for asthma-United States, 1980-2004: Surveillance summaries, October 19, 2007. MMWR. 2007; 5 (SS-8).

[2] Centers for disease control and prevention. Chronic obstructive pulmonary disease surveillance–United States, 1970–2000: Surveillance summaries, August 2, 2002. MMWR. 2002;51(SS-06).

[3] National Institutes of Health, National Heart, Lung and Blood Institute (NHLBI). Guidelines for the diagnosis and management of asthma (EPR-3) [Internet]. Bethesda, MD: NHLBI. Available from: http://www.nhlbi.nih.gov/guidelines/asthma

[4] Global Initiative for Chronic Obstructive Lung Disease (GOLD). Strategy for the diagnosis, management, and prevention of chronic obstructive pulmonary lung disease: Executive summary [Internet]. [cited 2010 Mar 12.] Available from: http://www.goldcopd.com

[5] Salerno M, Altes TA, Mugler JP, 3rd, Nakatsu M, Hatabu H, de Lange EE. Hyperpolarized noble gas MR imaging of the lung: Potential clinical applications. Eur J Radiol 2001; 40(1): 33-44.

[6] Moller HE, Chen XJ, Saam B, Hagspiel KD, Johnson GA, Altes TA, de Lange EE, Kauczor HU. MRI of the lungs using hyperpolarized noble gases. Magn Reson Med 2002; 47(6); 1029-1051.

[7] van Beek EJ, Wild JM, Kauczor HU, Schreiber W, Mugler JP, 3rd, de Lange EE. Functional MRI of the lung using hyperpolarized 3-helium gas. J Magn Reson Imaging 2004; 20: 540-554.

[8] Fain S, Scheibler ML, McCormack DG, Parraga G. Imaging of lung function using hyperpolarized helium-3 magnetic resonance imaging: Review of current and emerging translational methods and applications. J Magn Reson Imaging 2010; 32: 1398-1408.

[9] West JB. Pulmonary pathophysiology—the essentials. Baltimore, USA: Williams & Wilkins; 1998.

[10] Weibel ER. Morphometry of the Human Lung. Heidelberg: Spring Verlag; 1963.

[11] Lumb AB. Applied Respiratory Physiology. Edinburgh, Scotland: Butterworth Heinemann; 2000.

[12] Widdlicombe J, Davies A. Respiratory Physiology. Baltimore, USA: Edward Arnold Ltd; 1983.

[13] Rabe KF, Hurd S, Anzueto A, et al. Global initiative for chronic obstructive lung disease. Am J Respir Crit Care Med 2007; 176(6): 532-55.

[14] Standards for the diagnosis and management of patient with COPD. New York, NY: American Thoracic Society. European Respiratory Society; 2004. http://www. Thoracic.org/copd/pdf/copddoc.pdf

[15] Centers for Disease Control and Prevention (CDC), National Center for Health Statistics. Compressed mortality file 1999–2006. CDC WONDER on-line database, compiled from Compressed Mortality File 1999–2006 Series 20 No. 2L. Atlanta: CDC; 2009 [cited 2010 Mar 5]. Available from: http://wonder.cdc.gov/cmf-icd10.html

[16] Data Fact Sheet: Chronic Obstructive Pulmonary Disease. Bethesda, USA: NIH and NHLBI; 2010.

[17] Croxton TL, Weinmann GG, Senior RM, Wise RA, Crapo JD, Buist AS. Clinical research in chronic obstructive pulmonary disease: needs and opportunities. Am J Respir Crit Care Med 2003; 167(8): 1142-1149.

[18] Practical guide for the diagnosis and management of asthma. Bethesda, USA: NIH and NHLBI; 1997.

[19] Data Fact Sheet: Asthma Statistics. Bethesda, USA: NIH and NHLBI; 1999.

[20] National Institutes of Health, National Heart, Lung, and Blood Institute (NHLBI). National asthma education and prevention program expert panel report 3 (EPR3): Guidelines for the diagnosis and management of asthma. Bethesda, MD: NHLBI; 2007 Available from: http://www.nhlbi.nih.gov/guidelines/asthma/asthgdln.htm

[21] Arakawa A, Webb WR. Air trapping on expiratory high-resolution CT scans in the absence of inspiratory scan abnormalities: correlation with pulmonary function tests and differential diagnosis. AJR Am J Roentgenol 1998; 170(5): 1349-1353.

[22] Hogg JC. Airways pathology. In Barnes PJ, Drazen JM, Rennard S, Thomson NC, editors. Asthma and COPD, Basic mechanisms and clinical management. London, UK: Academic Press: 2002. p 57-66.

[23] Verbanck S, Schuermans D, Noppen M, VanMuylem A, Paiva M, Vincken W. Evidence of acinar airways involvement in asthma. Am J Respir Crit Care Med 1999; 159(5): 1545-1550.

[24] Kaczka DW. Ingenito EP, Israel E, Lutchen KR. Airway and lung tissue mechanics in asthma. Effects of albuterol. Am J Respir Crit Care Med 1999; 159(1): 169-178.

[25] Park CS, Mueller NL, Worthy SA, Kim JS, Awardh N, Fitzgarald M. Airway obstruction in asthmatic and healthy individuals: Inspiratory and expiratory thin section CT findings. Radiology 1997; 203(2): 361-367.

[26] James AL, Pare PD, Hogg JC. The mechanics of airway narrowing in asthma. Am Rev Respir Dis 1989; 139: 242-246.

[27] Benayoun L, Druilhe A, Dombret M-C, Aubier M, Pretolani M. Airway structural alterations selectively associated with severe asthma. Am J Respir Crit Care Med 2003; 167: 1360-8.

[28] Boulet L, Belanger M, Carrier G. Airway responsiveness and bronchial-wall thickness in asthma with or without fixed airflow obstruction. Am J Respir Crit Care Med 1995; 152:865-71.

[29] Paganin F, Seneterre E, Chanez P, Daures J, Bruel J, Michel F, et al. Computed tomography of the lungs in asthma : influence of disease severity and etilogy. Am J Respir Crit Care Med 1996; 153: 110-4.

[30] Castro M, Fain SB, Hoffman EA, Gierada DS, Erzurum SC, Wenzel S, et al. Lung imaging in asthmatic patients: the picture is clearer. J Allergy Clin Immunol. 2011; 128(3): 467-78.

[31] Pontana F, Faivre J, Remy-Jardin M, Flohr T, Schmidt B, Tacelli N, et al. Lung perfusion with dual-energy multidetector-row CT (MDCT): feasibility for the evaluation of acute pulmonary embolism in 117 consecutive patients. J Thorac Imaging 2008; 25: 100-11.

[32] Hoffman E, Chon D. Computed tomography studies of lung ventilation and perfusion. Proc Am Thorac Soc 2005; 2: 492-8, 506.

[33] Ohno Y, Koyama H, Yoshikawa T, et al. T_2* measurements of 3-T MRI with ultrashort TEs: Capabilities of pulmonary function assessment and clinical stage classification in smokers. AJR Am J Roentgenol 2011; 197: W279-W285.

[34] Kauczor H, Ebert M, Reitner K, Nilgens H, Surkau R, Heil W. Imaging of the lungs using [3]He MRI: Preliminary clinical experience in 18 patients with and without lung disease. J Magn Reson Imaging 1997; 7: 538-543.

[35] Altes TA, Powers PL, Knight-Scott J, Rakes G, Platts-Mills TAE, de Lange EE, Alford BA, Mugler III JP, Brookeman JR. Hyperpolarized [3]He MR lung ventilation imaging in asthmatics: Preliminary findings. J Magn Reson Imaging 2001; 13: 378-384.

[36] de Lange EE, Mugler JP, 3rd, Brookeman JR, Knight-Scott J, Truwit JD, Teates CD, Daniel TM, Bogorad PL, Cates GD. Lung air spaces: MR imaging evaluation with hyperpolarized [3]He gas. Radiology 1999; 210: 851-857.

[37] Marshall H, Deppe MH, Parra-Robles J, et al. Direct visualisation of collateral ventilation in COPD with hyperpolarised gas MRI. Thorax. 2012; 67(7): 613-7. Epub 2012 Jan 27.

[38] Brookeman JR, Mugler JP III, Knight-Scott J, Munger TM, de Lange EE, Bogorad PL. Studies of [3]He diffusion coefficient in the human lung: Age-related distribution patterns. Eur J Radiol 1999; 9: B21.

[39] Saam B, Yablonskiy D, Kodibagkar V, et al. MR imaging of diffusion of [3]He gas in healthy and diseased lungs. Magn Reson Med 2000; 44: 174-179.

[40] Salerno M, de Lange EE, Altes T, Truwit J, Brookeman J, Mugler JP 3rd. Emphysema: Hyperpolarized helium-3 diffusion MR imaging of the lungs compared with spirometric indexes- initial experience. Radiology 2002; 222: 252-260.

[41] Fain SB, Panth SR, Evans MD, et al. Early emphysematous changes in asymptomatic smokers: Detection with 3He MR imaging. Radiology 2006; 239(3): 875-883.

[42] Fischer M, Spector Z, Ishii M, Yu J, Emami K, Itkin M, Rizi R. Single-acquisition sequence for the measurement of oxygen partial pressure by hyperpolarized gas MRI. Magn Reson Med 2004; 52: 766-773.

[43] Miller GW, Mugler JP, 3rd, Altes TA, et al. A short breath-hold technique for lung pO2 mapping with [3]He MRI. Magn Reson Med 2010; 63: 127-136.

[44] Hamedani H, Emami K, Kadlecek S, et al. A multislice single breath-hold scheme for imaging alveolar oxygen tension in humans. Magn Reson Med 2011; 67: 1332-1345.

[45] Ruppert K, Brookeman JR, Hagspiel KD, Mugler JP, 3rd. Probing lung physiology with xenon polarization transfer contrast (XTC). Magn Reson Med 2000; 44: 349-357.

[46] Wang C, Miller GW, Altes TA, et al. Time dependence of 3He diffusion in the human lung: Measurement in the long-time regime using stimulated echoes. Magn Reson Med 2006; 56: 296-309.

[47] Samee S, Altes T, Powers P, et al. Imaging the lungs in asthmatic patients by using hyperpolarized helium-3 magnetic resonance: Assessment of response to methacholine and exercise challenge. J Allergy Clin Immunol 2003; 111: 1205-1211.

[48] Yablonskiy DA, Sukstanskii AL, Leawoods JC, et al. Quantitative in vivo assessment of lung microstructure at the alveolar level with hyperpolarized [3]He diffusion MRI. Proc Natl Acad Sci USA 2002; 99: 3111-3116.

[49] Swift AJ, Wild JM, Fichele S, et al. Emphysematous changes and normal variation in smokers and COPD patients using diffusion [3]He MRI. Eur J Radiol 2005; 54: 352-358.

[50] Salerno M, Altes T, Brookeman J, de Lange EE, Mugler J. Dynamic spiral MRI of pulmonary gas flow using hyperpolarized [3]He: Preliminary studies in healthy and diseased lungs. Magn Reson Med 2001; 46: 667-677.

[51] Mugler JP, 3rd, Altes TA. Hyperpolarized [129]Xe MRI of the human lung. J Magn Reson Imaging 2013; 37: 313-331.

[52] Foxall DL, Hoppel BE, Hariharan H. Calibration of the radio frequency field for magnetic resonance imaging.   Magn Reson Med 1996; 35: 229-236.

[53] Sacolick LI, Sun L, Vogel MW, Dixon WT, Hancu I. Fast radiofrequency flip angle calibration by Bloch–Siegert Shift. Magn Reson Med 2011; 66(5): 1333-8.

[54] Miller GW, Carl M, de Lange EE, Altes TA, Tobias WA, Mugler JP 3rd. A robust transmitter calibration procedure for NMR of hyperpolarized nuclei. Proc Intl Soc Mag Reson Med 2007; 15: 1268.

[55] Wild JM, Woodhouse N, Paley MN, Fichele S, Said Z, Kasuboski L, van Beek EJ. Comparison between 2D and 3D gradient-echo sequences for MRI of human lung ventilation with hyperpolarized 3He. Magn Reson Med 2004; 52(3): 673–678.

[56] Rivoire J, Terekhov M, Meise FM, Gast K, Salhi Z, Schreiber LM. Flip-angle measurement by magnetization inversion: Calibration of magnetization nutation angle in hyperpolarized 3He magnetic resonance imaging lung experiments. Magn Reson Med 2011; 65: 399-408.

[57] Mugler JP 3rd, Miller GW, Altes TA, de Lange EE, Brookeman JR. A low flip angle, phase-based method for accurately calibrating the transmitter in hyperpolarized-gas MRI. Proc Intl Soc Mag Reson Med 2005; 13: 789.

[58] Mugler JP 3rd, Miller GW. Rapid 3D mapping of the B_1 field using a low-flip-angle, phase-based method with improved sensitivity. Proc Intl Soc Mag Reson Med. 2007; 15: 351.

[59] Santoro D, Rivoire J, Meise F, et al. Three-dimensional mapping of the B1 field using an optimized phase-based method: Application to hyperpolarized 3He in lungs. Magn Reson Med 2011;65(4):1166-1172.

[60] Qing K, Miller GW, Mugler JP, 3rd. Performance of three transmitter calibration methods for hyperpolarized gas MRI in the presence of B_0 and B_1 inhomogeneity. Proc Intl Soc Mag Reson Med 2010; 18: 2574.

[61] Sacolick LI, Wiesinger F, Hancu I, Vogel MW. B1 mapping by Bloch-Siegert shift. Magn Reson Med 2010; 63(5): 1315-1322.

[62] Bloch F, Siegert A. Magnetic resonance for nonrotating fields. Phys Rev 1940; 57(6): 522-527.

[63] Ramsey NF. Resonance transitions induced by perturbations at two or more different frequencies. Phys Rev 1955; 100(4): 1191-1194.

[64] Steffen M, Vandersypen LMK, Chuang IL. Simultaneous soft pulses applied at nearby frequencies. J Magn Reson. 2000; 146: 369-374.

[65] Bergin CJ, Pauly JM, Macovski A. Lung parenchyma: Projection reconstruction MR imaging. Radiology, 1991; 179: 777-781.

[66] Heidemann RM, Griswold MA, Kiefer B, Nittka M, Wang J, Jellus V, Jakob PM. Resolution enhancement in lung ^{1}H imaging using parallel imaging methods. Magn Reson Med 2003; 49: 391-394.

[67] Woodhouse N, Wild JM, Paley MN, Fichele S, Said Z, Swift AJ, van Beek EJ.

Combined helium-3/proton magnetic resonance imaging measurement of ventilated lung volumes in smokers compared to never-smokers. J Magn Reson Imaging, 2005; 21: 365-369.

[68] Donnelly LF, MacFall JR, McAdams HP, Majure JM, Smith J, Frush DP, Bogonad P, Charles HC, Ravin CE. Cystic fibrosis: Combined hyperpolarized ^{3}He-enhanced and conventional proton MR imaging in the lung – preliminary observations. Radiology, 1999; 212: 885-889.

[69] Ireland RH, Woodhouse N, Hoggard N, Swinscoe JA, Foran BH, Hatton MQ, Wild JM. An image acquisition and registration strategy for the fusion of hyperpolarized helium-3 MRI and x-ray CT images of the lung. Phys Med Biol 2008; 53: 6055-6063.

[70] Wild JM, Woodhouse N, Teh K. Single-scan acquisition of registered hyperpolarized 3He ventilation and ADC images using a hybrid 2D gradient-echo sequence. Magn Reson Med 2007; 57: 1185-1189.

[71] Mugler JP, 3rd, Miller GW, Altes TA, et al. Rapid three-dimensional hyperpolarized 3He imaging of the lung using an optimized steady-state free-precession pulse sequence: Increased SNR without off-resonance banding artifacts. Proc Intl Soc Mag Reson Med 2008; 16: 2664.

[72] Wild JM, Ajraoui S, Deppe MH, et al. Synchronous acquisitions of hyperpolarized 3He and 1H MR images of the lungs – maximizing mutual anatomical and functional information. NMR Biomed 2011; 24(2): 130-134.

[73] Lustig M, Donoho D, Pauly JM. Sparse MRI: The application of compressed sensing for rapid MR imaging. Magn Reson Med 2007:58(6): 1182-1195.

[74] Ajraoui S, Lee KJ, Deppe MH, Parnell SR, Parra-Robles J, Wild JM. Compressed

sensing in hyperpolarized 3He lung MRI. Magn Reson Med 2010; 63(4): 1059-1069.

[75] Ajraoui S, Parra-Robles J, Wild JM. Incorporation of prior knowledge in compressed sensing for faster acquisition of hyperpolarized gas images. Magn Reson Med 2012, in press. doi: 10.1002/mrm.24252.

[76] Miller KW, Reo NV, Schoot Uiterkamp AJ, Stengle DP, Stengle TR, Williamson KL. Xenon NMR: Chemical shifts of a general anesthetic in common solvents, proteins, and membranes. Proc Natl Acad Sci USA 1981; 78(8): 4946-4949.

[77] Sakai K, Bilek AM, Oteiza E, et al. Temporal dynamics of hyperpolarized ^{129}Xe resonances in living rats. J Magn Reson B 1996; 111(3): 300-304.

[78] Wagshul ME, Button TM, Li HF, et al. In vivo MR imaging and spectroscopy using hyperpolarized ^{129}Xe. Magn Reson Med 1996; 36(2): 183-191.

[79] Mugler JP, 3rd, Diehuys B, Brookeman JR, et al. MR imaging and spectroscopy using hyperpolarized ^{129}Xe gas: Preliminary human results. Magn Reson Med 1997; 37(6): 809-815.

[80] Ruppert K, Brookeman JR, Hagspiel KD, Driehuys B, Mugler JP, 3rd. NMR of hyperpolarized ^{129}Xe in the canine chest: Spectral dynamics during a breath-hold. NMR Biomed 2000; 13(4): 220-228.

[81] Mugler JP, 3rd, Altes TA, Ruset IC, et al. Simultaneous magnetic resonance imaging of ventilation distribution and gas uptake in the human lung using hyperpolarized xenon-129. Proc Natl Acad Sci USA 2010; 1070; 107(50): 21707-21712.

[82] Driehuys B, Cofer GP, Pollaro J, Mackel JB, Hedlund LW, Johnson GA. Imaging alveolar-capillary gas transfer using hyperpolarized ^{129}Xe MRI. Proc Natl Acad Sci USA 2006; 103(48): 18278-18283.

[83] Dregly I, Mugler JP, 3rd, Ruset IC, et al. Hyperpolarized xenon-129 gas-exchange imaging of lung microstructure: First case studies in subjects with obstructive lung disease. J Magn Reson Imaging 2011:33(5): 1052-1062.

[84] Butler JP, Mair RW, Patz S, et al. Measuring surface-area-to-volume ratios in soft porous materials using laser-polarized xenon interphase exchange nuclear magnetic resonance. J Phys Condens Matter 2002: 14(13): L297-304.

[85] Swanson SD, Rosen MS, Coulter KP, Welsh RC, Chupp TE. Distribution and dynamics of laser-polarized [129]Xe magnetization in vivo. Magn Reson Med 1999; 42(6): 1137-1145.

[86] Wakayama T, Narazaki M, Kimura A, Fujiwara H. Hyperpolarized [129]Xe phase-selective imaging of mouse lung at 9.4T using a continuous-flow hyperpolarizing system. Magn Reson Med Sci 2008; 7(2): 65-72.

[87] Muradian I, Patz S, Butler JP, et al. Hyperpolarized 129Xe human pulmonary gas exchange with 3 point Dixon technique. Proc Intl Soc Mag Reson Med 2006; 14: 1297.

[88] Hersman FW, Ruset IC, Ketel S, et al. Large production system for hyperpolarized [129]Xe for human lung imaging studies. Acad Radiol 2008; 15(6): 683-692.

[89] Cleveland ZI, Cofer GP, Metz G, et al. Hyperpolarized [129]Xe MR imaging of alveolar gas uptake in humans. Plos ONE 2010; 5(8): e12192.

[90] Mugler JP, 3rd, Altes TA, Ruset IC, et al. Image-based measurement of T_2* for dissolved-phase Xe129 in the human lung. Proc Intl Soc Mag Reson Med 2012; 20: 1347.

[91] Ruppert K, Mata JF, Dregly IM, et al. Hyperpolarized xenon-129 dissolved-phase signal dependence on the echo time (abstract). Proc Intl Soc Mag Reson Med 2010; 18: 2552.

[92] Pauly J, Le Roux P, Nishimura D, Macovski A. Parameter relations for the Shinnar-Le Roux selective excitation pulse design algorithm. IEEE Trans Med Imaging 1991; 10(1): 53-65.

[93] Matson GB. An integrated program for amplitude-modulated RF pulse generation and re-mapping with shaped gradients. Magn Reson Imaging 1994; 12(8): 1205-1225.

[94] Qing K, Miller GW, Altes T, et al. Improved phase-based transmitter calibration for hyperpolarized-gas MRI using Shinnar-Le Roux RF Pulses (abstract). Proc Intl Soc Mag Reson Med. 2011; 19: 912.

[95] Cohen A, Daubechies I, Feauveau J-C. Biorthogonal bases of compactly supported wavelets. Comm Pure Appl Math 1992; 45(5): 485-560.

[96] Jafarpour S, Xu WY, Hassibi B, Calderbank R. Efficient and robust compressed sensing using optimized expander graphs. IEEE Trans Inform Theory 2009; 55(9): 4299-4308.

[97] Wang Z, Arce GR, Variable density compressed image sampling. IEEE Trans Image Proc 2010; 19(1): 264-270.

[98] Qing K, Altes TA, Tustison NJ, et al. Acquisition of spatially-registered helium-3 and proton 3D image sets of the lung in less than 10 seconds using compressed sensing (abstract). Proc Intl Soc Mag Reson Med. 2011; 19: 546.

[99] Wang Z, Bovic AC, Sheikh HR and Simon EP. Image quality assessment: from error visibility to structural similarity IEEE transactions on image processing 2004: 13(4): 600-612.

[100] Qing K, Altes TA, Tustison NJ, et al. Quantitative assessment of compressed-sensing reconstruction fidelity for 3D He-3 and H-1 acquisitions in one

breath-hold (abstract). Proc Intl Soc Mag Reson Med. 2012; 20: 4003.

[101] Tustison NJ, Avants BB, Flors Lucia, Altes TA, de Lange EE, Mugler JP, 3rd, Gee JC. Ventilation-based segmentation of the lungs using hyperpolarized ^{3}He MRI. J Magn Reson Imaging 2011: 34: 831-841

[102] Tustison NJ, Contrella B, Altes TA, Avants B, de Lange EE, Mugler JP, 3rd. Longitudinal assessment of treatment effects on pulmonary ventilation using 1H/3He MRI multivariate templates (abstract). Proc SPIE 2013; vol 8672-33.

[103] http://www.picsl.upenn.edu/ANTs

[104] Dixon WT. Simple proton spectroscopic imaging. Radiology 1984; 153(1): 189-194.

[105] Glover GH, Schneider E. Three-point Dixon technique for true water/fat decomposition with B_0 inhomogeneity correction. Magn Reson Med 1991; 18(2):371-383.

[106] Reeder SB, McKenzie CA, Pineda AR, et al. Water-fat separation with IDEAL gradient-echo imaging. J Magn Reson Imaging 2007; 25(3): 644-652.

[107] Yu H, McKenzie CA, Shimakawa A, et al. Multiecho reconstruction for simultaneous water-fat decomposition and T2* estimation. J Magn Reson Imaging 2007; 26(4): 1153-1161.

[108] Chan RW, Ramsay EA, Cheung EY, Plewes DB. The influence of radial undersampling schemes on compressed sensing reconstruction in breast MRI. Magn Reson Med 2012; 67(2):363-377.

[109] Sutton BP, Noll DC, Fessler JA. Fast, iterative image reconstruction for MRI in the presence of field inhomogeneities. IEEE Trans Med Imaging 2003; 22(2): 178-188.

[110]. Tsao J, Jiang Y. Hierarchical IDEAL – robust water-fat separation at high field by multi-resolution field map estimation. Proc Int Soc Magn Reson Med 2008; 16: 653.

[111] Jiang Y, Griswold M, Tsao J. Fast and robust separation of multiple chemical species from arbitrary echo times with complete immunity to phase wrapping. Proc Int Soc Magn Reson Med 2012; 20: 2484.

[112] Tsao J, Jiang Y. Hierarchical IDEAL: Fast, robust, and multiresolution separation of multiple chemical species from multiple echo times. Magn Reson Med 2012. doi: 10. 1002/mrm. 24441.

[113] Pineda AR, Reeder SB, Wen Z, Pelc NJ. Cramer-Rao bounds for three-point decomposition of water and fat. Magn Reson Med 2005; 54: 625-635.

[114] Hernando D, Kellman P, Haldar JP, Liang ZP. Robust water/fat separation in the presence of large field inhomogeneities using a graph cut algorithm. Magn Reson Med 2010; 63: 79-90.

[115] Yu H, Reeder SB, et al. Field map estimation with a region growing scheme for iterative 3-point water-fat decomposition. Magn Reson Med 2005 Oct; 54(4): 1132-9.

[116] Patz S, Muradian I, Hrovat M, et al. Human pulmonary imaging and spectroscopy with hyperpolarized [129]Xe at 0.2T. Acad Radiol. 2008; 15(6): 713-727.

[117] Ruppert K, Mata JF, Brookeman JR, Hagspiel KD, Mugler JP, 3rd. Exploring lung function with hyperpolarized [129]Xe nuclear magnetic resonance. Magn Reson Med 2004; 51: 676-687.

[118] Kaushik SS, Cleveland ZI, Cofer GP, et al. Diffusion-weighted hyperpolarized [129]Xe MRI in healthy volunteers and subjects with chronic obstructive pulmonary disease. Magn Reson Med 2011; 65(4): 1154-1165.

[119] Reis S, Ruppert K, Altes T, et al. Hyperpolarized Xe-129 CSI of the human lung: Preliminary results from healthy, second-hand smokers and cystic-fibrosis subjects (abstract). Proc Int Soc Magn Reson Med 2012; 20: 629.

[120] Dregley I, Mugler JP, 3rd, Ruset IC, et al. Multiple-exchange-time xenon polarization transfer contrast (MXTC) MRI: Initial results in animals and healthy volunteers. Magn Reson Med 2012; 67(4): 943-953.